THE ^{40}CA(α,γ)^{44}TI NUCLEAR REACTION USING DRAGON

by

CHRISTIAN OUELLET, M.SC

A Thesis

Submitted in Partial Fulfillment

of the Requirements

for the Degree of

Doctor of Philosophy

Oct 2007

McMaster University

MASTER OF SCIENCE (2003) Queen's University
(physics) Kingston, Ontario

TITLE: The ^{40}Ca(α,γ)^{44}Ti Nuclear Reaction Using DRAGON

AUTHOR: Christian Ouellet

SUPERVISOR: Professor A. Chen

NUMBER OF PAGES: xiii, 94

Abstract

In our every day life we are surrounded by materials composed of the elements of the periodic table. Rarely does one ask where these elements came from. It has been a long process of discovery to understand the precise origin of many of the elements we consider commonplace. It is now believed that the Big-Bang produced only the lightest elements, primarily hydrogen and helium, and that heavier elements were synthesized as the product of nuclear reactions within stars. Occasionally the nuclear reactions that occur within stars produce an isotope of an element which is unstable, radioactive. When a radioactive species decays it emits radiation which is characteristic of the species that decayed. Satellites have been able to detect the characteristic radiation from the decay of several isotopes in the Milky Way. One in particular which has been detected is the isotope of titanium, ^{44}Ti. The decay of ^{44}Ti has been seen in the ashes of exploding stars, vast gas clouds termed supernova remnants. This isotope of titanium eventually decays to a stable isotope of calcium found everywhere on Earth from bones to chalk. It is believed that the bulk of the production in stars of ^{44}Ti occurs as the star explodes, during the supernova. Calculations indicate that among the many possible reactions during a supernova, a particular nuclear reaction, where calcium captures a helium nucleus and fuses into titanium, is the main source of ^{44}Ti. In this work it is detailed how using laboratory equipment on Earth one is able to shed light on the nuclear physics of this particular reaction governing the production of an isotope in our universe.

Acknowledgments

Thanks to all those who helped me during my doctoral study and research at McMaster, TRIUMF and at home.

In particular I would like to first thank my supervisor, Dr. Alan Chen, who gave me this great opportunity to pursue the highest level of education by choosing me as a student. His guidance was instrumental in the quality of my research, the successful completion of my degree and the quality of the document you now hold. I couldn't have asked for a better supervisor.

Next I would thank Vera Tang, who has stuck with me through the difficult moments of my life. This work would never have been completed, let alone completed on time, without her. Love you girl.

I would like to thank Christof Vockenhuber, who helped me through every step of the experiment and analysis. Definitely a high caliber scientist, I always felt like I was playing catch-up to get to his level of understanding.

I would also thank the entire DRAGON collaboration for their toil and effort to make this experiment a success. I would particularly like to thank John D'Auria, who wisely steered me towards taking on this project, Dave Hutcheon, who patiently explained the ins-and-outs of DRAGON to me, Jonty Pearson and Chris Ruiz for general help and advice along the way.

I would finally like to thank my parents, who never ceased to imprint upon me the value of education and helped me out when times were tough, and my rabbits Wup, Spud and Meba for keeping me sane (relatively).

Table of Contents

List of Figures

List of Tables

Chapter 1

Introduction

We take the word "atom" from the Greek *atomos* which means indivisible. It was in the fifth century BC that Democritus first proposed the idea that our world is composed of basic building blocks which could not be further cut or divided [7]. However in the 5th century there was fierce theoretical competition from Empedocles, another Greek philosopher who brought forth in his *Tetrasomia* the idea that everything in the natural world was composed of four basic elements: Earth, Fire, Water and Air [8].

It was not until the dawn of the 19th century that the atomic explanation of matter acquired significant scientific interest. In 1803, while investigating why chemicals react in specific proportions, John Dalton proposed that certain chemicals are formed of a single atom and that these atoms can join to each other to form compound chemicals [9]. To what would perhaps be the frustration of Democritus, the types of these single atoms were dubbed elements.

In 1897, while working on cathode rays, J.J. Thompson discovered that the atoms of Dalton could in fact be further sub-divided [10]. He discovered the electron, and shortly thereafter in 1909 Ernest Rutherford discovered the nucleus [11]. Despite these discoveries and the many that would follow, the term "atom" continued to describe the agglomerate system of a dense positive nucleus and diffuse circling electrons. It was Henry Moseley who discovered in 1913 that nuclear charge is the key physical property that distinguishes one element from the next [12]. Serious scientific efforts to classify elements were undertaken in as early as 1661 with Robert Boyle showing that there could not be merely the four of Greek philosophy [13]. Antoine Lavoisier in 1789 had a table of elements which also included such things as "light" and "caloric" [14]. The first classification into a periodic table of elements is credited to Dmitri

Mendeleev and in his day (1869) there were 66 [15].

Today 117 elements fill the periodic table [16]. The nucleus is understood as a combination of protons and neutrons. The protons carry a unit of charge and the neutrons do not. As Moseley's work entailed, an element is characterized by the number of protons its nucleus has. The number of neutrons can vary, forming the many isotopes of that element. On Earth 94 of these 117 elements can be found, with a total of 327 isotopes. The question then is: How did all these elements and isotopes come to be? To answer that question is one of the principal goals of nuclear astrophysics.

1.1 Nuclear Astrophysics

Aristotle reasoned that earth, air, fire and water were Earthly elements and corruptible. The heavens appeared unchanging, incorruptible, and so stars would need a fifth element, the *aether* or equivalently *quintessence* to explain their substance [17]. He would certainly be much surprised that today's science turns to the stars themselves as the origin of all elements save a handful. To properly explain this last statement, the history of the universe must be traced back to its genesis [18].

1.1.1 Big Bang Nucleosynthesis

Certainly the most interesting result from astrophysics of the 20th century is that our universe had a beginning. It is now understood that at one point in our Universe's distant past, all of its matter was concentrated into a small volume, no larger than a grapefruit, and was very hot [19]. The universe in exploding outwards cooled rapidly and over time all the structures seen today in the night sky, such as stars and galaxies, were formed [20, 21]. At the very high densities and temperatures of the very early universe, nuclei were simply unable to form. The universe was a small, dense mix of high energy particles. Nucleosynthesis is thought to begin and end within the first 5 minutes of the expansion of the Universe. As the universe expanded and cooled unstable high energy particles decay to form the stable protons and unstable neutrons. The protons and neutrons interacted during this short phase, and occasionally fused to form light stable elements, namely, Deuterium, Helium, ^{3}He and Lithium. Neutrons that were not bound with protons decayed into electrons and protons.

In principle, if the universe expanded slowly enough, then all the elements could be formed out of this hot soup of protons and neutrons. This was the idea of George Gamow, the originator of Big-Bang nucleosynthesis

[22, 23]. However, experimental measurements of the atmospheres of very old stars indicate that the universe expanded and cooled too rapidly for the heavier elements to form. The prediction is that the first generation of stars, the ones formed out of primordial material from the Big-Bang must have been composed of Hydrogen and Helium with only trace amounts of Lithium, Deuterium and ^{3}He [24, 25].

To explain the origin of heavier elements requires the mechanisms of stellar and explosive nucleosynthesis.

1.1.2 Hydrogen Burning

As the universe cooled, gas clouds of Hydrogen and Helium coalesced under the influence of gravity to form stars and eventually galaxies and clusters of galaxies. For a time in the 20th century there was a significant amount of debate as to how a star could avoid simply collapsing in on itself as there was no known mechanism strong enough to oppose relentless gravity [26]. From the virial theorem a cloud of collapsing gas certainly heats up, and outward pressure does correspondingly build up opposing the inward free fall of material. Over time however the gas cools, releasing radiant energy into the universe at large and gravitational collapse is unavoidable [26] . As more and more data appeared to indicate our Sun was billions of years old, the problem grew more mysterious. What was required was a source of energy to generate pressure and keep the star from gravitational collapse. The solution would come in the form of nuclear fusion.

Einstein's ubiquitous equation of $E = mc^2$ is the basis of how this process creates energy [27]. Because the velocity of light c is a very large number, even a small amount of mass can be converted into a large amount of energy. At the cores of stars such as our Sun the Hydrogen gas is under great pressure (2.5 x 10^8 atm) from the surrounding gas and its temperature is very high (1.56 x 10^7 K). Under such conditions material enters a new state of matter; no longer a gas, it becomes a plasma, where the electrons no longer orbit the nuclei. In the case of Hydrogen plasma this means a soup of protons and electrons. When two protons fuse, the mass of the corresponding deuterium is less than the sum mass of two protons, and energy is thus released.

$$\mathrm{p} + \mathrm{p} \rightarrow \mathrm{d} + \mathrm{e}^+ + \nu_e \qquad (\mathrm{Q} = 1.44\,\mathrm{MeV}) \tag{1.1}$$

The release of energy Q indicated includes the annihilation energy of the positron e^+. In 1938 Bethe and Critchfield performed the first quantum mechanics calculations to estimate the rate of this reaction within our Sun [28]. To within an order of magnitude the calculations indicated that the reaction could produce enough energy to sustain the Sun against gravitational collapse,

in hydrostatic equilibrium. This reaction is the first, critical step in energy generation, termed hydrogen burning. As will be seen, the ashes of hydrogen burning will account for further nucleosynthesis beyond the big-bang.

The pp chain reactions

There are three proton-proton nuclear reaction chains active during hydrogen burning. The pp chains, like many stellar nuclear reactions, have rates which are highly sensitive to temperature, this temperature dependence will be explained in the theory section. The first pp chain (PPI) is the following set of reactions:

$$\mathrm{p} + \mathrm{p} \rightarrow \mathrm{d} + \mathrm{e}^{+} + \nu_e \tag{1.2}$$

$$\mathrm{p} + \mathrm{d} \rightarrow {}^{3}\mathrm{He} + \gamma \tag{1.3}$$

$${}^{3}\mathrm{He} + {}^{3}\mathrm{He} \rightarrow {}^{4}\mathrm{He} + 2\mathrm{p} \tag{1.4}$$

PPI is responsible for 86% of the power generation in our Sun [18]. The second pp chain (PPII) is responsible for nearly all the remainder, 13.88% of the power generation:

$${}^{3}\mathrm{He} + {}^{4}\mathrm{He} \rightarrow {}^{7}\mathrm{Be} + \gamma \tag{1.5}$$

$${}^{7}\mathrm{Be} + \mathrm{e} \rightarrow {}^{7}\mathrm{Li} + \nu_e \tag{1.6}$$

$${}^{7}\mathrm{Li} + \mathrm{p} \rightarrow 2\,{}^{4}\mathrm{He} \tag{1.7}$$

The final pp chain (PPIII) is responsible for only 0.02% of the power generation in our Sun, it comprises of reactions 1.2, 1.3, 1.5 as well as the following:

$${}^{7}\mathrm{Be} + \mathrm{p} \rightarrow {}^{8}\mathrm{B} + \gamma \tag{1.8}$$

$${}^{8}\mathrm{B} \rightarrow {}^{7}\mathrm{Be} + \mathrm{e}^{+} + \nu_e \rightarrow 2\,{}^{4}\mathrm{He} + \mathrm{e}^{+} + \nu_e \tag{1.9}$$

In stars heavier than our Sun, and thus with higher core temperatures, the bulk of the power generation will shift towards the PPII and PPIII chains. In young stars, that is to say stars enriched with heavier elements other than those originating uniquely from the Big-Bang, yet another cycle may appear. The CNO cycle is believed to be the dominant energy production cycle in heavy stars [18]. Its reaction network uses Carbon, Nitrogen and Oxygen nuclei and, through proton capture, beta decay and alpha decay. The particulars may vary, but the net nucleosynthesis of all these reaction chains remains a constant:

$$4\mathrm{p} \rightarrow {}^{4}\mathrm{He} + 2\mathrm{e}^{+} + 2\nu_e \tag{1.10}$$

The star transmutes Hydrogen into Helium.

1.1.3 Helium Burning

As Hydrogen burning progresses Helium builds up in the core of the star. At the temperatures of hydrogen burning Helium is unable to fuse into heavier elements in any appreciable quantity. There is a gap of stable elements between the atomic numbers 8 and 5, where presumably two ^{4}He or a ^{4}He and Hydrogen might fuse. As the Helium core grows the number density of Hydrogen atoms able to react in the PP chains decreases. With fewer reactions, there is less heating and so the pressure drops. The Helium core is forced to contract gravitationally and so its temperature increases. In an evolved star, Hydrogen burning forms but a thin layer about the Helium core. This thin layer of hydrogen burning continues to feed Helium to the core, the core continues to contract and the temperature of the core rises.

The contraction of the Helium core marks an important stage in stellar evolution. Increasing core temperature means a net increase in outward thermal pressure. The large Hydrogen layer enveloping the core responds to the increased outward pressure by expanding, sometimes by as much as a factor of 50 in radius relative to its original size. The envelope expands to such a degree that its surface temperature drops. With a lower surface temperature the radiation emitted by the star shifts towards longer wavelengths, into the red. This is the red giant phase of stellar evolution.

For large stars with masses in excess of 10 times our Sun, Helium burning ignites when temperatures of 1-2x10^{8}K and densities of 10^2-10^5 g cm^{-3} are reached in the core. At these high densities and temperatures, the capture of an ^{4}He nucleus, also called an alpha particle, is probable enough that even a short lived species such as ^{8}Be (half life 1x10^{-16}s) can capture one readily. The overall process can be viewed as an equilibrium of the reactions that follow:

$$\alpha + \alpha \rightleftarrows {}^8\mathrm{Be} \tag{1.11}$$

$$\alpha + {}^8\mathrm{Be} \rightleftarrows {}^{12}\mathrm{C}^* \tag{1.12}$$

where the * is to indicate that ^{12}C is produced in an excited state of the nucleus. The excited state means that equation 1.12 is not a true equilibrium. Irreversible leakage occurs when the ^{12}C nucleus de-excites, either through gamma emission or electron positron pair production to the ground state of ^{12}C. The sum process is:

$$3\,{}^4\mathrm{He} \rightleftarrows {}^{12}\mathrm{C}^* \rightarrow {}^{12}C + (\gamma\gamma \text{ or } \mathrm{e}^+\mathrm{e}^-) \tag{1.13}$$

and is termed the triple alpha process and arguably the most important reaction for all of nuclear astrophysics (and carbon based life-forms) [29]. This reaction is an example of a resonant capture reaction which will be discussed

in detail in the theory section.

1.1.4 Advanced and Explosive Burning

Only the most prominent features of stellar burning nucleosynthesis can be here described. The complete picture involves a very large number of interdependent reactions termed reaction networks.

The product of Helium burning is Carbon. The ^{12}C reacts slowly with the Helium to form ^{16}O. A Carbon-Oxygen core gradually forms. The star begins to acquire what is best described as an onion-like structure: A large outer envelope of Hydrogen, a much smaller Helium envelope with a Hydrogen burning layer, and a Carbon-Oxygen core. The core will again reach such a point that it contracts and new nuclear reactions become possible at higher temperatures and pressures, synthesizing ever heavier elements. An important consequence of this process is that each phase of nuclear burning is significantly shorter than its predecessor, because thermonuclear reaction rates increase exponentially with increased temperature. These results are summarized in Table 1.1 (table from [30]).

Table 1.1. Evolutionary Stages of a 25 Solar Mass Star

Stage	Time Scale	Temperature in 10^9K	Density (g cm^{-3})
Hydrogen burning	7x10^{6}y	0.06	5
Helium burning	5x10^{5}y	0.23	7x10^2
Carbon burning	600 y	0.93	2x10^5
Neon burning	1 y	1.7	4x10^6
Oxygen burning	6 y	2.3	1x10^7
Silicon burning	1 day	4.1	3x10^7
Core collapse	seconds	8.1	3x10^9
Core bounce	milliseconds	34.8	$\tilde{3}$x10^{14}
Explosive burning	0.1-10 s	1.2-7.0	Variable

Carbon burning produces an Oxygen-Neon core. Neon burning produces energy through photodisintegration of ^{20}Ne into ^{16}O, the resulting alpha combining with undissociated Neon into ^{24}Mg [31, 32]. The primary reaction is endothermic but subsequent secondary reactions lead to a net positive energy balance. A predominantly Oxygen core is produced out of Neon burning. When finally the Oxygen core contracts, ^{16}O reacts with itself and produces a ^{28}Si core [33]. The Silicon core is unable to fuse Silicon with Silicon because

of the very high temperature (T >3.5x10^9 K) that reaction requires. Instead, before these temperatures are reached, photodisintegration takes place as in the case of Neon burning. Silicon is photodisintegrated into lighter nuclei, protons, neutrons and alphas. The products of the photodisintegration react with each other in a dizzying array of reactions producing an Iron-Nickel core [34, 35]. When the Iron-Nickel core is so massive as to contract, something very dramatic happens resulting in a complete explosion of the star, a supernova.

1.1.5 Nucleosynthesis Beyond Iron

One of the properties of nuclear physics that is most important to nuclear astrophysics is the binding energy of the nucleus. Iron is the most tightly bound nucleus in nature. In simple terms this means that the fusion of nuclei with a product that is lighter or equal in mass to iron releases energy. In addition, the fusion of nuclei that are equal or greater in mass than iron requires energy.

1.1.5.1 Core Collapse Supernovae

The Iron-Nickel core is unable to generate energy through fusion. It is held in equilibrium against gravity by a quantum mechanical effect, namely degeneracy pressure. Degeneracy pressure is the result of the Pauli exclusion principle which states that two fermions can not occupy the same quantum state. In the case of the Iron-Nickel core it is the electrons in the plasma which provide the degeneracy pressure. However, as Silicon burning progresses, more mass is added to the core and electron degeneracy pressure is overcome [18].

The specifics of what happens next as the core enters into free-fall is an active field of research. Some general features are however well understood. It is clear that the core will collapse quickly ($\sim$ seconds), completely independent of the burning shells that surround it. As the core collapses gravitationally, the nuclei are forced together until they begin to touch, and the entire core reaches nuclear density. The nucleons then themselves exert a degeneracy pressure. This degeneracy pressure halts the collapsing core very quickly and a hydrostatic bounce of the infalling core occurs. The bounce is very stiff, and an outward compression wave is reflected from the center of the star which when the lower density burning material is impacted turns into a shock-wave. After bounce, most of the core will rapidly evolve into either a neutron star, or a black-hole if the mass of the core is sufficient. The gravitational energy that is gained as the core collapses is almost entirely lost to the creation of neutrinos. Although the precise mechanism of explosion remains unclear what is known is that the shockwave takes only a fraction of the total explosive

energy, ∼1%, and imparts to the outer layers an outward velocity which is in excess of the escape velocity [36]. This leads to the ejection of most of the mass of the star into the interstellar medium, and with that mass the products of nucleosynthesis within the star.

1.1.5.2 S-process, R-process

Abundance is the term used to describe the proportion of an element relative to the total of all elements. The interstellar medium (ISM) is seeded with the products of the burning cycles of stars that have undergone supernova explosions, and new stars that form from the gas of the ISM exhibit initially the particular abundance pattern of their progenitors. A great deal of experimental effort has gone into determining the abundances of our local solar system. The graph of their distribution can be seen in Fig 1.1.

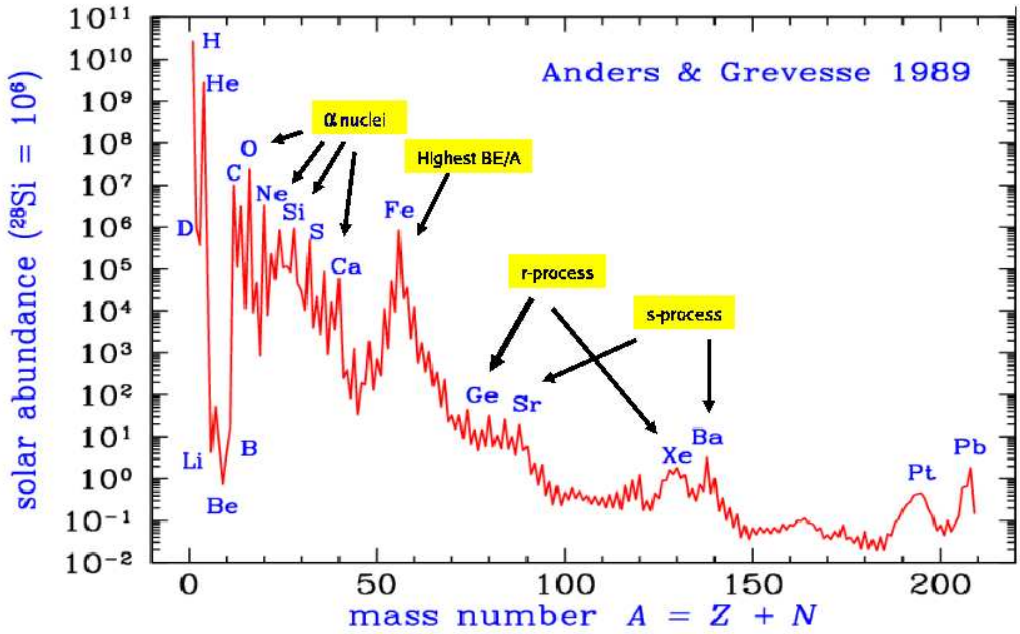

Figure 1.1. The abundance pattern of our solar system. The characteristics of this pattern can be understood through nuclear astrophysics.

The particular features of this graph can be understood through the lens of nuclear astrophysics.

The sloping curve from Hydrogen towards the iron peak is the direct result of the burning phases of stellar evolution: each of these phases involves positively charged nuclei fusing to form heavier nuclei. The like charges repel via the electromagnetic force and present a Coulomb barrier that must be

penetrated before fusion is to occur. This Coulomb barrier grows stronger with greater charges and thus it is significantly more difficult for stars to produce heavier elements from fusion, requiring ever higher temperatures (see theory section for further detail).

The strong peak of Iron elements at A ∼60 is a testament to the end of stellar burning and the peak in nuclear binding energy at Iron. For the elements beyond Iron, one would expect then almost no production, but this is not what is seen. The abundances of the elements beyond iron progress along an almost linear path all the way up through the transuranic elements, and quantities are small but non-negligible (∼3% of the iron peak elements). From the Coulomb barrier argument, the origin of these elements must result from the capture of non-charged particles, namely neutrons. Two processes have been proposed to explain this distribution, a rapid-capture of neutrons and a slow capture of neutrons with accompanying beta-decays, see Fig 1.2 [37]. The slow s-process occurs continuously over the lifetime of the star,

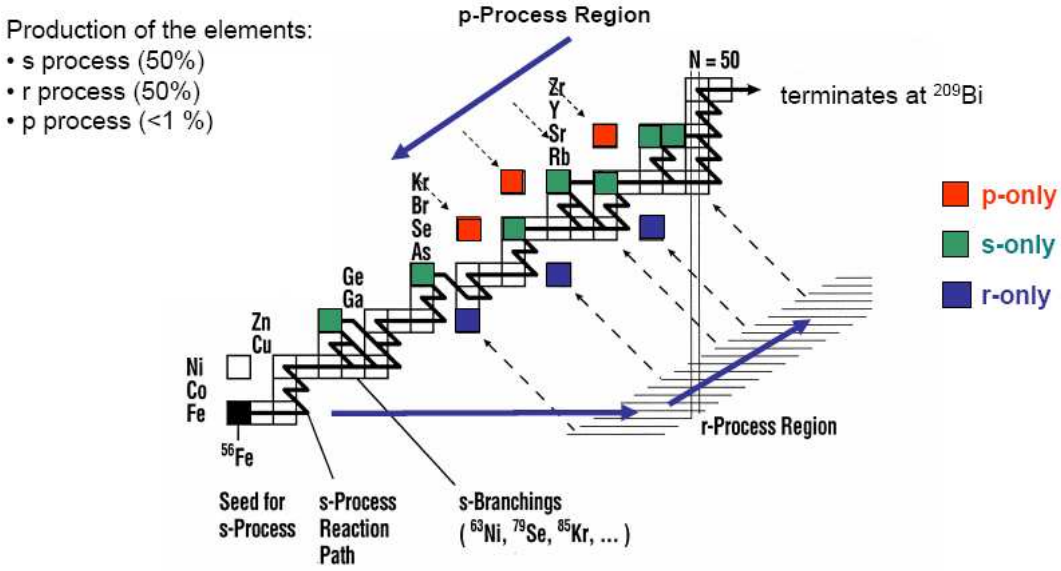

Figure 1.2. A schematic of the r-process and the s-process. Both processes involve capture of neutrons and then subsequent β-decay to stable elements. The p-process occurs only rarely, in exotic astrophysical environments such as novae, and it involves a rapid capture of protons.

with neutrons generated in the various burning stages readily capturing on the heavy seed nuclei out of silicon burning. For instance the nucleus ^{127}I captures a neutron producing unstable ^{128}I which decays with a half-life of 25 minutes to the stable isotope of ^{128}Xe. The s-process occurs when the neutron density is low and the resulting unstable nuclei are given sufficient time to decay. The specific sites of generation of the neutrons are the capture of alpha

particles on ^{13}C and ^{22}Ne in a type of star called an AGB star (Asymptotic Giant Branch). The rapid r-process is believed to occur during the violent end of stellar evolution when neutron densities are very high and it accounts in particular for the radioactive isotopes beyond ^{209}Bi such as ^{235}U. When the neutron density is very high ($\sim 10^{19}$ neutrons cm^{-3}) nuclei can often capture neutrons faster than they can beta-decay. Very unstable nuclei can thus be formed and very high atomic numbers can be reached following a different pathway along the chart of nuclides than the s-process. The r-process has also been proven to be at the origin of nuclei in the 90-200 region, abundance peaks at A $\sim$130 and 195 can thus be explained. The particular astrophysical site(s) of the r-process remains unclear though supernova are a likely candidate [38].

1.2 ^{44}Ti and ^{44}Ca Production

Titanium and Calcium are elements most of us are familiar with in our everyday environment. Calcium is the fifth most abundant element in the Earth's crust closely followed by Titanium in ninth [39]. The origin of these elements is clearly understood as a result of the solar system forming from gas clouds enriched by the ashes of the nuclear burning of stars that came before the Sun. The abundances of elements in our solar system can be, by and large, attributed to the processes that have been previously described. However, certain particular elements and isotopes such as ^{44}Ca can have a different astrophysical mechanism for their production. ^{44}Ca is the second most abundant of the stable Ca isotopes, 2% of all Calcium (^{40}Ca is the most abundant 97%). It is the end result of the decay of ^{44}Ti which proceeds by electron capture first into ^{44}Sc then into ^{44}Ca. While Helium and Silicon burning produces some quantity of ^{44}Ti another mechanism is required to explain the observed abundances namely the alpha-rich freezeout.

1.2.1 Alpha Rich Freezeout

In a core-collapse supernova the shockwave that the core sends forth dramatically heats the matter of the silicon burning shell, reaching an estimated $\sim$7-10 billion degrees [36]. At these temperatures nuclei break apart into nucleons and alphas. This layer, along with the other outer layers surrounding the core, is ejected by the shockwave into space and rapidly cools. The cooling allows free neutrons and protons to recombine into more alphas, much akin to the Big-Bang. However unlike the Big-Bang the cooling is not as rapid - the alphas are able to reassemble into heavier nuclei. The synthesis is also heavily influenced by the black-hole or neutron star which gravitationally

re-absorbs some of the mass of this innermost layer, termed the "mass cut". ^{12}C nuclei are assembled in the hot dense expanding alpha cloud by the same triple-alpha process of Helium burning. The Carbon nuclei absorb more and more alphas and free nucleons and thus become heavier. Because of the high density the various elements synthesized by this process also eject nucleons through photo-ejection processes and so a state of nuclear quasi-equilibrium occurs between them. It is not a true thermal equilibrium because the rates at which emission and absorption processes occur are not equal, and heavier stable elements are formed out of lighter less stable elements. The expanding gas rapidly evolves to be composed primarily of Nickel isotopes and alphas. Many other species co-exist in this state of quasi-equilibrium in quantities of lesser abundance, and one among these is ^{44}Ti. *Freezeout* occurs when the temperature and density drops below the levels required for the alphas to fuse into heavier nuclei. The final state is then a gas with many heavy elements and "frozen" un-recombined alphas.

This process of alpha-rich freezeout was first predicted in 1969 [40]. As the gas from the supernova expands it thins and the radiation from the products of the alpha-rich freezeout can thus escape unimpeded into the universe at large. In particular the radioactive decay of the unstable elements produced emit gamma-rays which can be detected using satellite-based detectors and was used to confirm the existence of this process.

1.2.2 Experimental Evidence

1.2.2.1 Supernova Remnants

The decay of ^{44}Ti into ^{44}Sc produces principally two γ-ray lines of 68 keV and 78 keV. The subsequent decay of ^{44}Sc proceeds almost entirely to ^{44}Ca with a characteristic 1.16 MeV γ-ray. ^{44}Ti is a very important species for the direct observation of ongoing nucleosynthesis for a number of reasons:
1- it is produced in sufficient quantities to be detected in space
2- its half-life is 58.9$\pm$0.3 years [41], which means it decays quickly enough to produce a measurable flux of γ-rays and
3- its half-life is not so short as to disappear entirely within the first few moments of the supernova, allowing astronomers time to detect it
The CGRO (Compton Gamma Ray Observatory) satellite telescope first reported in 1994 the detection of the 1.16 MeV line characteristic of the decay of ^{44}Ti in the young supernova remnant Cassiopeia A, Fig 1.3 [42]. Another satellite BeppoSAX subsequently confirmed this by detection of the 68 and 74 keV lines from the same galactic source in 2001 [43]. The strength of these

Figure 1.3. Cassiopeia A is the closest supernova remnant in our Galaxy and one of the most studied [1]. It is at the origin of a lot of the interest in ^{44}Ti.

lines combined with the known distance from the source and half-life allows astronomers to accurately estimate the total production, or total yield, of ^{44}Ti in these supernova. The most recent satellite investigation by INTEGRAL revealed the 68 keV and 74 keV lines and from that data an estimated ejected mass of $1.6^{+0.6}_{-0.3}\times10^{-4}$ Solar mass of ^{44}Ti [44]. On the 24th of February, 1987, a star underwent a core-collapse supernova in the Large Magellanic Cloud, a nearby small daughter galaxy to our own. This famous event is dubbed supernova 1987a. SN1987a provided a wealth of data on supernova, and in particular SN1987a ejected a mass estimated to 7% of the mass of the Sun ($M_\odot$) in radioactive isotopes of Nickel and 10^{-4} $M_\odot$ of ^{44}Ti [45].

1.2.2.2 Presolar Grains

Titanium is strongly chemically reactive and readily combines with Oxygen to form TiO, Ti_2O_3 and TiO_2. On Earth it is most commonly found in the form of *rutile* which is as common as sand (1%) in the Earth's crust [39]. After the alpha-rich freezeout, as the expanding gas cools to the point where molecules may form, the ^{44}Ti produced reacts chemically with the other

elements in the cloud to form into macroscopic grains. These grains thus carry with them the isotopic signature of the individual supernova.

As our solar system was forming the ejected gas clouds from many previous supernovae contributed to the elemental abundances but the isotopic signatures of the individual supernovae were lost in the subsequent heating and mixing of the planets and Sun. However certain carbonaceous meteorites did not entirely destroy the grains ejected from the individual supernovae and these dubbed "presolar grains" have been recovered. The presolar grains exhibit isotopic abundances radically different from any terrestrial object and can be studied in detail using the technique of Secondary Ion Mass Spectrometry (SIMS). The isotopic ratio of ^{44}Ca to ^{40}Ca is greatly enhanced in these grains (4-100 times the solar value). This anomoly was the first unambiguous indication that these grains had a supernova origin [46]. These types of grains were furthermore postulated to exist in 1975 by D. Clayton. The complete implications of presolar grains for supernova theory have yet to be uncovered but they will doubtless prove significant.

1.2.3 Controversy and Motivation of the Experiment

Theoretical investigations into the nuclear reactions governing the synthesis of ^{44}Ti have been performed and they point towards a few key reactions . One of the most prominent of these is the capture of an alpha particle on ^{40}Ca with the emission of a γ-ray photon, abbreviated ^{40}Ca(α,γ)^{44}Ti [47]. This reaction was studied during the 1970's by bombarding a ^{40}Ca target with alpha particles and detecting the γ-rays that resulted [2, 3, 4, 5, 6]. These studies covered a range of energies generally higher than that of astrophysical interest, however Cooperman studied the range of energies which correspond to temperatures of T_9= 1.2-2.9 (T_9= 10^9 K).

A more recent experiment used a different method: activation of a ^{4}He gas by a ^{40}Ca beam with subsequent implantation of the ^{44}Ti recoils into a foil target [48]. The foil target was then chemically treated to extract the Titanium and the isotopic ratio of ^{44}Ti to ^{48}Ti was measured using AMS. This experiment agreed well with the γ-ray studies over a limited range but when the range was extended to energies corresponding to T_9= 0.98 significantly greater yield, a factor of 2.4 to 4.8, was observed in the most recent publication.

Theoretical models predicting the total amount of ^{44}Ti ejected from CasA relying on uniquely γ-ray data estimate 2 to 10 times less production than what is observed. In the case of 1987a it is a factor of $\sim$3. The estimate for 1987a does not come however from direct detection of the γ-rays. Instead it comes from the indirect analysis of the light curve, that is to say the afterglow of the supernova, which is powered by scattering of the γ-rays from the

radioactive decay of ^{44}Ti [49]. Attempts at direct detection are still ongoing.

Purely theoretical models based on a Hauser-Feshback statistical approach also have provided a reaction rate for ^{40}Ca(α,γ)^{44}Ti. One code among these is termed NON-SMOKER, and this code is then adjusted by experimental data to produce a reaction rate from a code termed REACLIB [50]. It is one of the goals of this work to improve these predictions to arrive at a more accurate rate for supernova models.

There is also significant interest in locating other supernova remnants through the detection of ^{44}Ti γ-rays in the Milky Way. Perplexingly there appear to be very few sources aside from CasA in our galaxy. Searches are ongoing; a possible source in the Vela region was recently identified [51].

The motivation of this experiment was to pin down in detail the nuclear physics portion of these many controversies, to provide the most accurate determination of the ^{40}Ca(α,γ)^{44}Ti reaction over the range of astrophysically relevant temperatures using a powerful direct-detection technique, capturing both the γ-ray and the Titanium produced.

1.3 Thesis Outline

Chapter 2 presents the theoretical framework of stellar thermonuclear reactions. Particular attention is paid to the importance of resonant capture and how the reaction rate is calculated using laboratory data. The DRAGON (Detector of Recoils And Gammas Of Nuclear reactions) is the apparatus used to perform the experiment and its functioning is expounded in Chapter 3 as well as the technical difficulties particular to this experiment and how these were surmounted. Chapter 4 details the analysis of the data collected as well as the interpretation of the results into an astrophysical context, namely the stellar reaction rate. Finally Chapter 5 is a discussion of the implications of this work in relation to other experiments and nucleosynthesis in supernovae.

Chapter 2

Theory of Stellar Nuclear Reactions

Heaven lasts long, and Earth abides.
What is the secret of their durability?
Is it not because they do not live for themselves
That they can live so long?
-Li Po, from the Yang Collection

Our Sun is the closest star to us and we are able to observe in detail even daily changes in magnetic fields, effects due to rotation, tidal distortions, pulsations. Communication systems on Earth can be influenced by sunspot activity and the accompanying solar flares. These are minor variations which cannot be felt or observed from afar, as we view the other stars of our galaxy and Universe. Be it luminosity, mass, radius, or even chemical composition of the outer layers inferred from spectroscopy, over human lifespans the vast majority of stars exhibit an extreme constancy in their physical properties. This implies that the stellar interior must be in a state of hydrostatic and thermal equilibrium and thus the physics of their hot gaseous interiors becomes relatively simple.

2.1 Kinematics

Despite densities in excess of solid lead and extreme pressures the stellar plasma in the cores of stars behaves as an ideal gas. This is because free electrons and the nuclei completely stripped of their electrons occupy a very small amount of space: a typical atomic radius is $\sim 10^{-10}$m whereas a nucleus is $\sim 10^{-15}$m. Temperature at the macroscopic level is a result of the average

velocity of the gas particles at the microscopic level. The hotter the gas the higher the average velocity of particles, and thus the higher their kinetic energy which is critically important for fusion reactions of charged particles as will be seen.

The velocity distribution of an ideal gas follows the Maxwell-Boltzmann distribution. Even at the temperatures involved in alpha-rich freezeout and stellar cores only very few of the fusing nuclei reach speeds comparable to the speed of light. It is therefore not necessary to involve the theory of Relativity, since the simpler Newtonian dynamics is sufficient.

In the following discussion vector quantities will be denoted by a bold face. Consider two particles on a collision course of respective masses m_1 and

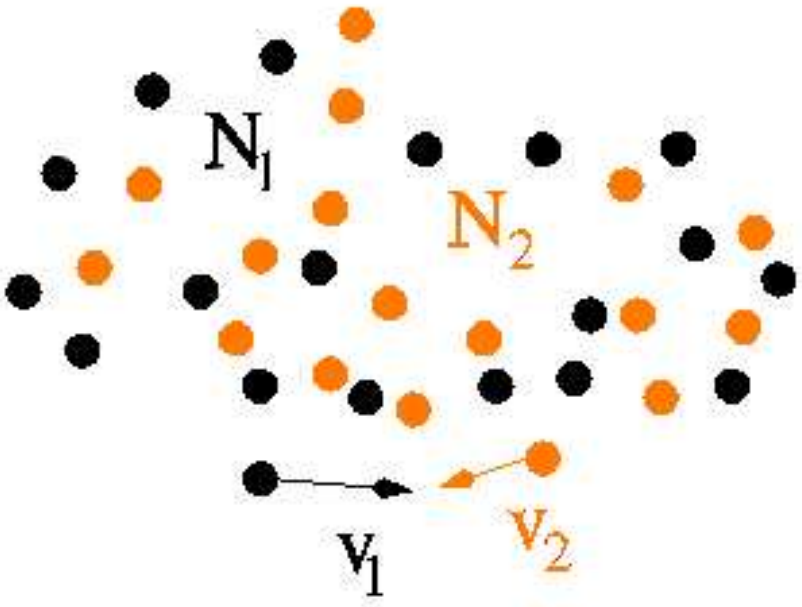

Figure 2.1. Schematic of the hot gaseous interior of stars where nuclei fuse.

m_2, and velocities $\mathbf{v}_1$ and $\mathbf{v}_2$ as pictured in Fig 2.1. Much of the complexity of calculations can be reduced by shifting the reference frame to the center of mass. The center of mass (cm) velocity of the system is defined as:

$$\mathbf{V}_{cm} = \frac{m_1\mathbf{v}_1 + m_2\mathbf{v}_2}{m_1 + m_2} \tag{2.1}$$

Viewed in the center of mass reference frame the particles appear to be colliding with velocities:

$$\mathbf{v}_1 - \mathbf{V}_{cm} = \frac{m_2}{m_1 + m_2}(\mathbf{v}_1 - \mathbf{v}_2) \tag{2.2}$$

$$\mathbf{v}_2 - \mathbf{V}_{cm} = -\frac{\mathrm{m}_1}{\mathrm{m}_1 + \mathrm{m}_2}(\mathbf{v}_1 - \mathbf{v}_2) \tag{2.3}$$

The initial total kinetic energy before collision, K_i, is:

$$\mathrm{K}_i = \frac{1}{2}\mathrm{m}_1\mathbf{v}_1^2 + \frac{1}{2}\mathrm{m}_2\mathbf{v}_2^2 \tag{2.4}$$

Using the cm velocity:

$$\mathrm{K}_i = \frac{1}{2}(\mathrm{m}_1 + \mathrm{m}_2)\mathbf{V}_{cm}^2 + \frac{1}{2}\frac{\mathrm{m}_2\mathrm{m}_1}{\mathrm{m}_2 + \mathrm{m}_1}(\mathbf{v}_1 - \mathbf{v}_2)^2 \tag{2.5}$$

In this experiment a beam of ^{40}Ca particles (label 1) is fired at a stationary ^{4}He gas target (label 2). The kinetic energy of the beam is much greater than the thermal kinetic energy of the gas target atoms, so their velocities can be set to be zero in these equations ($\mathbf{v}_2$= 0). The total energy for collision in the lab frame of reference is then:

$$\mathrm{E}_{lab} = \frac{1}{2}\mathrm{m}_1\mathbf{v}_1^2 \tag{2.6}$$

In the cm frame of reference, the velocity of the cm is zero, $\mathrm{V}_{cm} = 0$. The energy in the cm frame relative to the velocities of the lab frame (where $\mathbf{v}_2$ = 0) is then:

$$\mathrm{E}_{cm} = \frac{1}{2}\frac{\mathrm{m}_2\mathrm{m}_1}{\mathrm{m}_2 + \mathrm{m}_1}\mathbf{v}_1^2 \tag{2.7}$$

By substitution the key equation that relates the energy of the beam as measured in the lab to the energy of the collision in the center of mass frame is found:

$$\mathrm{E}_{cm} = \frac{\mathrm{m}_2}{\mathrm{m}_2 + \mathrm{m}_1}\mathrm{E}_{lab} \tag{2.8}$$

2.2 Thermonuclear Reaction Rates

For fusion reactions to occur there need not be a head-on collision, although this is favorable. In general nuclei will react within some small volume. This reaction volume is quite generally on the same scale as the volume of nuclei and is heavily influenced by the amount of collision energy available and specific nuclear properties of the colliding nuclei. From the frame of reference of the individual particles, the volume of reaction appears as an effective cross-sectional area and it is conventional to describe reactions by their velocity dependent effective cross-section, σ(v) (or equivalently σ(E)).

In the stellar plasma nuclei are found with varying concentrations and velocities, and the stellar reaction rate must take this explicitly into account.

Consider two particle types, one of number density N_1 and the other of number density N_2, moving with a relative velocity v_1-v_2. Each of these particle types will have a Maxwell-Boltzmann velocity distribution $\Phi_i(\mathrm{v}_i)$ such that $\int_0^\infty \Phi_i(\mathrm{v}_i)d^3\mathrm{v}_i = 1$ and

$$\Phi_i(\mathrm{v}_i) = \left(\frac{\mathrm{m}_i}{2\pi kT}\right)^{3/2} \exp\left(-\frac{\mathrm{m}_i \mathrm{v}_i^2}{2kT}\right) \tag{2.9}$$

Then the stellar reaction rate r_{12} is given by,

$$r_{12} = N_1 N_2 \int_{v_1}\int_{v_2} (\mathrm{v}_1 - \mathrm{v}_2)\sigma(\mathrm{v}_1 - \mathrm{v}_2)\Phi_1(\mathrm{v}_1)\Phi_2(\mathrm{v}_2)d^3\mathrm{v}_1 d^3\mathrm{v}_2 \tag{2.10}$$

The expression $\Phi_1\Phi_2$ expanded is:

$$\Phi_1(\mathrm{v}_1)\Phi_2(\mathrm{v}_2) = \frac{(\mathrm{m}_1\mathrm{m}_2)^{3/2}}{(2\pi kT)^3}\exp\left(-\frac{\mathrm{m}_1\mathrm{v}_1^2 + \mathrm{m}_2\mathrm{v}_2^2}{2kT}\right) \tag{2.11}$$

This last expression (2.11) can be re-written by analogy with equation 2.5 using the cm velocity and the relative velocity $\mathbf{v} = \mathbf{v}_1$ - $\mathbf{v}_2$,

$$\Phi_1(\mathrm{v}_1)\Phi_2(\mathrm{v}_2) = \frac{(\mathrm{m}_1\mathrm{m}_2)^{3/2}}{(2\pi kT)^3}\exp\left(-\frac{(\mathrm{m}_1+\mathrm{m}_2)}{2kT}\mathrm{V}^2 - \frac{\mathrm{m}_1\mathrm{m}_2}{2kT(\mathrm{m}_1+\mathrm{m}_2)}\mathrm{v}^2\right) \tag{2.12}$$

A change of basis can then be made for the reaction rate integral 2.10 from (v_1, v_2) to (V,v). To adjust the differentials the Jacobian for the change of basis must be calculated for each component and they are all equal to 1; for instance the x-component:

$$\begin{vmatrix} \frac{\delta \mathrm{V}_{1x}}{\delta \mathrm{V}_x} & \frac{\delta \mathrm{V}_{1x}}{\delta \mathrm{v}_x} \\ \frac{\delta \mathrm{V}_{2x}}{\delta \mathrm{V}_x} & \frac{\delta \mathrm{V}_{2x}}{\delta \mathrm{v}_x} \end{vmatrix} = \begin{vmatrix} 1 & \frac{\mathrm{m}_2}{\mathrm{m}_1+\mathrm{m}_2} \\ 1 & -\frac{\mathrm{m}_1}{\mathrm{m}_1+\mathrm{m}_2} \end{vmatrix} = 1 \tag{2.13}$$

The reaction rate in the new basis can then be written as,

$$\begin{aligned} r_{12} = \quad & N_1 N_2 \left(\tfrac{\mathrm{m}_1+\mathrm{m}_2}{2\pi kT}\right)^{3/2} \int_V \exp\left(-\tfrac{(\mathrm{m}_1+\mathrm{m}_2)}{2kT}\mathrm{V}^2\right) d^3\mathrm{V} \\ & \times \left(\tfrac{\mathrm{m}_1\mathrm{m}_2}{(\mathrm{m}_1+\mathrm{m}_2)*2\pi kT}\right)^{3/2} \int_v \mathrm{v}\sigma(\mathrm{v})\exp\left(-\tfrac{\mathrm{m}_1\mathrm{m}_2}{2kT(\mathrm{m}_1+\mathrm{m}_2)}\mathrm{v}^2\right) d^3\mathrm{v} \end{aligned} \tag{2.14}$$

The first integral is merely the integral of a Maxwell-Boltzmann distribution and is by definition equal to 1. The second integral is a triple integral in velocity, which by analogy to x-y-z volume integrals can be converted into a single integral along the radial velocity direction with the additional factor of $4\pi\mathrm{v}^2$. The formulae can be further simplified in appearance by using what is

termed the reduced mass $\mu = (\mathrm{m_1 m_2})/(\mathrm{m_1} + \mathrm{m_2})$ and we are left with,

$$r_{12} = N_1 N_2 4\pi \left(\frac{\mu}{2\pi kT}\right)^{3/2} \int_0^\infty \mathrm{v}^3 \sigma(\mathrm{v}) \exp\left(-\frac{\mu}{2kT}\mathrm{v}^2\right) d\mathrm{v} \tag{2.15}$$

While the reaction rate is the important physical quantity, it is customary to report instead a reaction rate per particle pair, $\langle \sigma \mathrm{v} \rangle = r_{12}/(N_1 N_2)$ and to express it in terms of the center of mass energy. From the discussion of the kinematics section the center of mass energy E_{cm}=$\mu \mathrm{v}^2/2$ and we arrive at the final formulation of the thermonuclear reaction rate per particle pair:

$$\langle \sigma \mathrm{v} \rangle = \left(\frac{8}{\pi\mu}\right)^{1/2} (kT)^{-3/2} \int_0^\infty \mathrm{E}_{cm} \sigma(\mathrm{E}_{cm}) \exp\left(-\frac{\mathrm{E}_{cm}}{kT}\right) d\mathrm{E} \tag{2.16}$$

To evaluate the reaction rate it is thus required to know the functional form of the nuclear cross section σ(E). However, to achieve this a distinction must be made between resonant and non-resonant fusion reactions as the functional form is very different in each case.

2.2.1 Non-Resonant Fusion Reactions

The stellar fusion reaction rate of nuclei can be best described as a competition between the Maxwell-Boltzmann distribution which vanishes at high energies and the Coulomb barrier which grows ever stronger at lower energy. Only a small portion of all the nuclei, those in the tail end of the Maxwell-Boltzmann distribution with very high velocities, will actually fuse. They fall within an energy range called the Gamow window, as will be seen.

To properly explain the Coulomb barrier an appeal to quantum mechanics is necessary. The two body Schroedinger wave equation is,

$$-\frac{\hbar^2}{2\mu}\nabla^2 \Psi + \mathrm{V}(r)\Psi = \mathrm{E}_{cm}\Psi \tag{2.17}$$

Ψ is the two body wavefunction and $\hbar$ is Planck's constant divided by 2π [52]. V(r) is the electrostatic repulsive Coulomb potential that the nuclei generate and that the center-of-mass kinetic energy E_{cm} must overcome for the nuclei to get close enough for the strong nuclear force to fuse them. In the case of two nuclei with Z_1 and Z_2 respective number of protons, then it has the form,

$$\mathrm{V}(r) = \frac{\mathrm{Z}_1 \mathrm{Z}_2 e^2}{r} \tag{2.18}$$

where e is a unit of elementary charge. At first glance equation 2.17 does

not seem to account for the relative angle of collision. To make this apparent the wave function $\Psi(r,\theta,\phi)$ can be separated into a radial piece, $f(r)$ and an angular piece made up of spherical harmonics $Y_l^m(\theta,\phi)$. When substituted back into equation 2.17, terms that depend uniquely on the radius can be sorted onto the left hand side of the equation and terms that depend uniquely on the angles on the right hand side. The differential equation is then termed "separable" and each side must both be identically zero. The radial equation becomes:

$$-\frac{\hbar^2}{2\mu}\frac{d^2(rf(r))}{dr^2}+[\frac{l(l+1)\hbar^2}{2\mu r^2}+V(r)-E_{cm}]rf(r)=0 \tag{2.19}$$

The relative angular momentum l between the two nuclei then becomes apparent as the centrifugal part of the effective potential V_l,

$$\mathrm{V}_l(r)=\frac{l(l+1)\hbar^2}{2\mu r^2}+\frac{\mathrm{Z}_1\mathrm{Z}_2e^2}{r} \tag{2.20}$$

Equation 2.20 is truly only valid for radii greater than the overlap of the two nuclear surfaces. Every nucleus has a semi-empirical radius of $\sim 1.35\mathrm{A}^{1/3}$ fm. Below $2\mathrm{R}= 1.35(\mathrm{A}_1^3+\mathrm{A}_2^3)$ the potential changes radically - the strong nuclear force dominates and binds the nuclei. However nuclei almost never have sufficient energy to completely overcome the Coulomb barrier. In a classical situation they would be reflected back at a radius R_c where $\mathrm{E}(\mathrm{R}_c)=\mathrm{V}_l(\mathrm{R}_c)$. Instead, as a result of their wave-like nature, they tunnel through the barrier with some small but not insignificant probability.

The quantum tunneling probability $\mathrm{P}_l(\mathrm{E})$ is given by the WKB approximation,

$$\mathrm{P}_l(\mathrm{E})\propto\exp\left(-\frac{(8\mu)^{1/2}}{\hbar}\int_{2R}^{R_c}(\mathrm{V}_l(r)-\mathrm{E})^{1/2}dr\right) \tag{2.21}$$

Typically for nuclear astrophysics $\mathrm{E}\ll\mathrm{V}_l(2\mathrm{R})$ and this integral can be well approximated by,

$$\mathrm{P}_l(\mathrm{E})\propto\exp\left(-2\pi\frac{\mathrm{Z}_1\mathrm{Z}_2e^2}{\hbar}(\frac{\mu}{2\mathrm{E}})^{1/2}\right) \tag{2.22}$$

To compare this tunneling probability with the nuclear cross-section the coefficient of proportionality must be established. Because nuclei have a wave-like spatial distribution, the cross section must be proportional to the geometrical area of the nuclei. That area is the square of the nuclear wavelengths, named after de-Broglie, $\lambda=h/(2\mu E)^{(1/2)}$ in the cm frame. The cross section can then

be written as,

$$\sigma(\mathrm{E}_{cm}) = \frac{\mathrm{S}(\mathrm{E}_{cm})}{\mathrm{E}_{cm}} \exp\left(-2\pi \frac{\mathrm{Z}_1 \mathrm{Z}_2 e^2}{\hbar} (\frac{\mu}{2\mathrm{E}_{cm}})^{1/2}\right) \tag{2.23}$$

The quantity S(E) is termed the "astrophysical S-factor" and it is introduced to account for the approximations made as well as any additional contributions from nuclear structure effects. For many nuclear reactions it is a very slowly varying function over a broad range of energies. It can be considered to be a constant specific to the reaction. Substituting our expression for the cross-section, equation 2.23, into the reaction rate, equation 2.16, gives,

$$\langle \sigma \mathrm{v} \rangle = \left(\frac{8}{\pi\mu}\right)^{1/2} (kT)^{-3/2} \mathrm{S} \int_0^\infty \exp\left(-\frac{\mathrm{E}_{cm}}{kT} - \frac{2\pi Z_1 Z_2 e^2}{\hbar} (\frac{\mu}{2\mathrm{E}_{cm}})^{1/2}\right) d\mathrm{E} \tag{2.24}$$

The reaction rate can now be seen as a competition between the Maxwell-Boltzmann distribution, which is large at low energies and small at high energies ($\propto$ exp(-E)) and the Coulomb barrier penetrability which is small at low energies and large at high energies ($\propto$ exp(-$\mathrm{E}^{-1/2}$)), as shown in Fig 2.2. At the temperatures of interest in stellar reactions the product of these exponentials produces a function which looks not dissimilar to a Gaussian. This function is dubbed the Gamow window. It is peaked at the effective burning energy, E_{eff}, which is determined by setting the first derivative of equation 2.24 to zero [52, 18],

$$\mathrm{E}_{eff} = \left(\pi \frac{Z_1 Z_2 e^2 kT}{\hbar} (\frac{\mu}{2})^{1/2}\right)^{2/3} \tag{2.25}$$

The Gamow window has an approximate width at half-maximum $\Delta\mathrm{E}_{eff}$ given by,

$$\Delta\mathrm{E}_{eff} = (\frac{8\mathrm{E}_{eff} kT}{3})^{1/2} \tag{2.26}$$

The majority of non-resonant reactions occur within energies of $\mathrm{E}_{eff} \pm \Delta\mathrm{E}_{eff}/2$. The total reaction rate can however be dominated by resonant reactions within the Gamow window. An example of a non-resonant reaction is direct capture. In direct capture the products of the reaction emerge without a transitional state, as opposed to resonant capture where a compound nucleus is first formed as will be seen in the following section.

2.2.2 Resonant Fusion Reactions

Nuclei are quantum mechanical systems. That is to say that they do not behave in the classical physics sense with a continuous range of physical

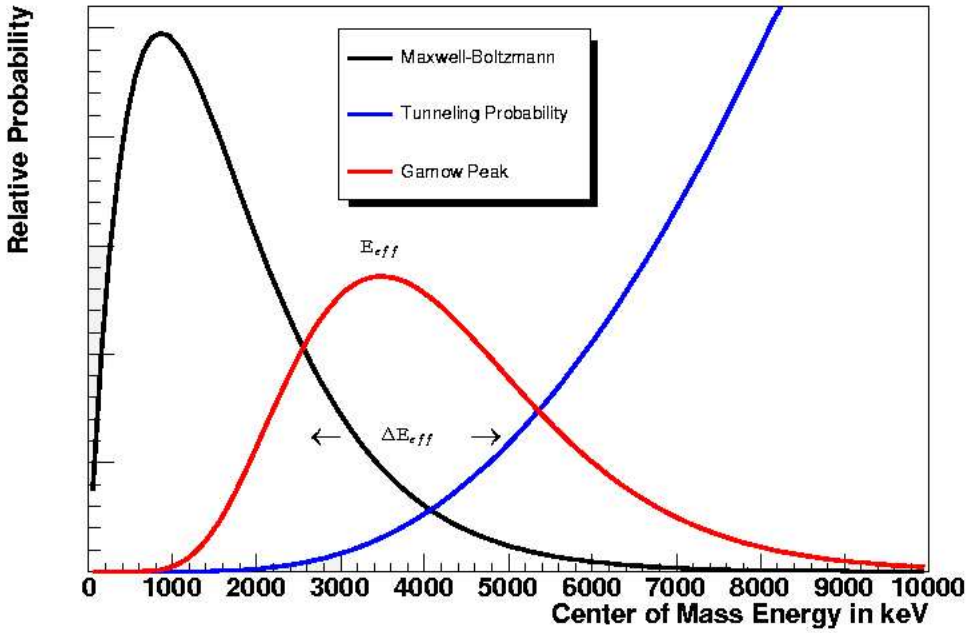

Figure 2.2. The Gamow window for the ^{40}Ca(α,γ)^{44}Ti reaction at T= 10^{10}K. The graphs have been arbitrarily scaled so as to make them all visible on the same plot.

states. Instead they exhibit discrete properties such as angular momentum and in particular excitation energy. Excitation energy is energy stored within the nucleus for a certain amount of time, typically very short, in a quasi-stationary state before being converted into particles, typically particles of light, γ-rays. Every nucleus has discrete excitation energies that are most often tabulated in the form of an energy level diagram.

When two nuclei collide they form a compound system - a new nucleus that is typically in an excited state, depending on the energetics of the reaction. When the center of mass energy of the collision precisely matches an excitation energy level of the compound nucleus the fusion reaction is greatly enhanced. Such a reaction is described as resonant.

The above statement is a good conceptual generalization, but requires some modification to be entirely correct. By the Heisenberg uncertainty principle, quantum mechanics allows the compound nucleus to have a tiny amount of energy fluctuation about its excited energy level. This range is termed a "line width" and while excitation energies are typically on the MeV scale, the line widths are on the keV scale and smaller. Furthermore two nuclei fusing in a resonant reaction can be greatly aided or impeded by their relative angular momentum and must still be influenced by their de-Broglie wavelength area. Combining these ideas is the Breit-Wigner formula [18], the nuclear cross

section for resonant radiative capture reactions:

$$\sigma(\mathrm{E}_{cm}) = \frac{\lambda^2}{4\pi}\frac{2J_r+1}{(2J_p+1)(2J_t+1)}\frac{\Gamma_p\Gamma_\gamma}{(\mathrm{E}_{cm}-\mathrm{E}_r)^2+(\Gamma/2)^2} \tag{2.27}$$

The labels p,t and r refer to the projectile, target and resonance. The curve this function makes as a function of energy can be seen in Fig 2.3.

The Js' are the respective intrinsic angular momenta (spins) of the nuclei involved. Γ_p is the partial width of the entrance channel, Γ_γ is the partial width of the exit channel and $\Gamma = \Gamma_p + \Gamma_\gamma$ is the total reaction width. The partial widths are much akin to linewidths in that they are an energy range tolerance over which the reaction can occur. Because Γ_p is proportional to the tunneling probability, the Gamow window remains critical to determining which excitation energy states can contribute meaningfully to the reaction rate.

Substitution of equation 2.27 into equation 2.16 produces,

$$\langle\sigma\mathrm{v}\rangle = \frac{h^2\sqrt{2}}{(\pi kT\mu)^{3/2}}\frac{2J_r+1}{(2J_p+1)(2J_t+1)}\int_0^\infty \frac{\Gamma_p\Gamma_\gamma \exp\left(-\frac{E_{cm}}{kT}\right)}{(\mathrm{E}_{cm}-\mathrm{E}_r)^2+(\Gamma/2)^2}d\mathrm{E} \tag{2.28}$$

For a narrow resonance, $\Gamma \ll \mathrm{E}_r$, the energy dependence of the partial widths can be ignored and the integral has an analytic form which leads to the narrow resonance reaction rate per particle pair:

$$\langle\sigma\mathrm{v}\rangle = \hbar^2\left(\frac{2\pi}{kT\mu}\right)^{3/2}\frac{2J_r+1}{(2J_p+1)(2J_t+1)}\exp\left(-\frac{\mathrm{E}_r}{kT}\right) \tag{2.29}$$

The resonance strength is the quantity $\omega\gamma$ where,

$$\omega = \frac{2J_r+1}{(2J_p+1)(2J_t+1)} \tag{2.30}$$

and,

$$\gamma = \frac{\Gamma_p\Gamma_\gamma}{\Gamma} \tag{2.31}$$

Even a single resonance can dominate the entire reaction rate. Some nuclei can have such a large number of resonances in the Gamow window that the reaction rate is entirely dominated by resonant capture fusion reactions. The reaction rate then becomes a sum over all resonances and their respective energies and resonance strengths:

$$\langle\sigma\mathrm{v}\rangle = \left(\frac{2\pi}{kT\mu}\right)^{3/2}\hbar^2\sum_i(\omega\gamma)_i\exp\left(-\frac{\mathrm{E}_{ri}}{kT}\right) \tag{2.32}$$

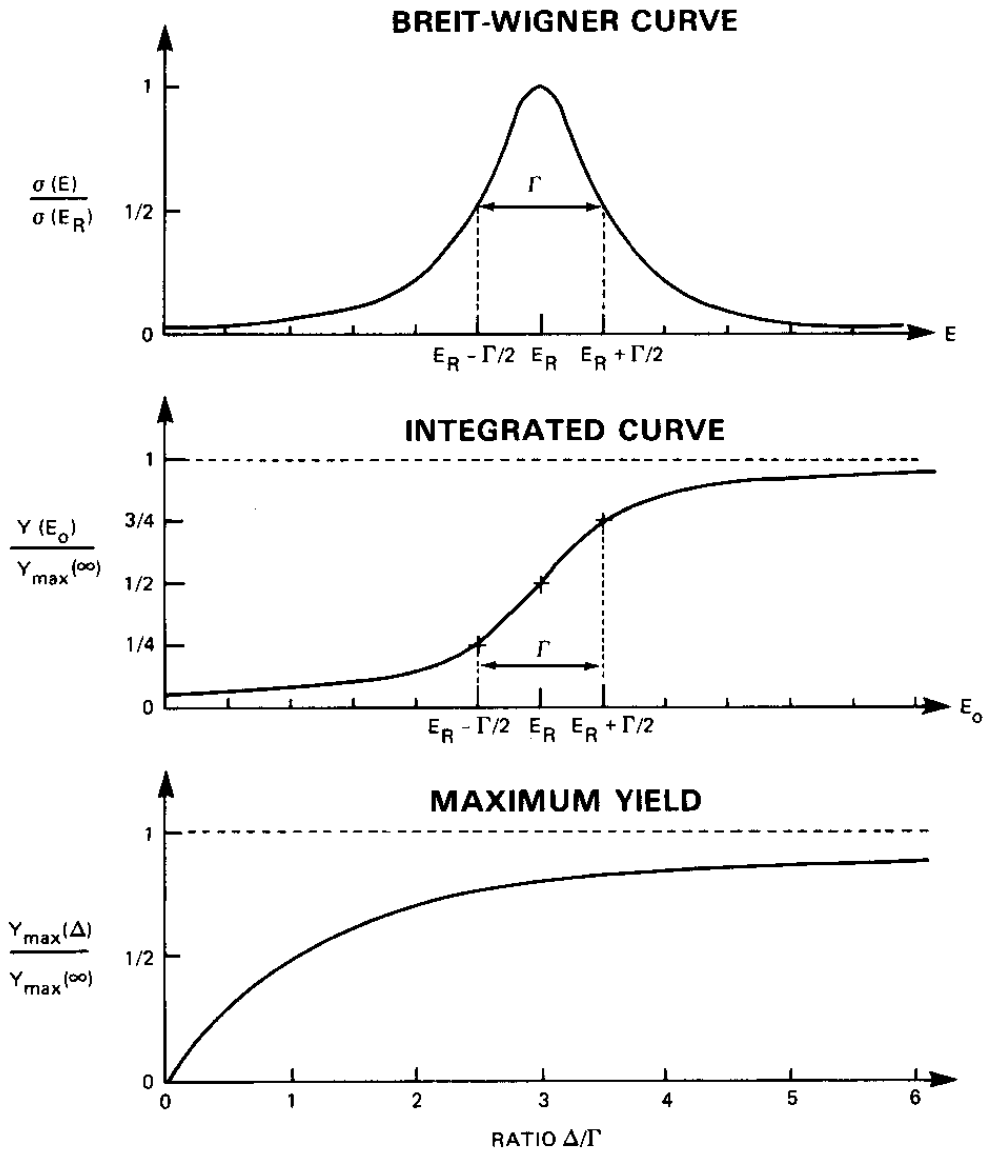

Figure 2.3. The Breit Wigner curve (top) depicts the peaked nuclear cross section for resonant reactions. The ratio of the yields between a finite target to the theoretical infinitely long target can be seen as a function of energy (mid). The bulk of the resonant reactions clearly occur within the target in a small range of energy defined by the total width Γ of the reaction. (Bottom) So long as the energy loss within the target is 6 times the width Γ the experimental yield will be 89% of the theoretical limit.

In general it is difficult if not impossible to derive theoretically the energy levels of any given nucleus beyond hydrogen. This is due to the great complexity of the strong nuclear force and many body physics. Appeal is then made to

experiments such as this one to determine at which energies resonances occur and their spins and partial widths.

2.3 Laboratory Yields

Physics laboratories are unable to simulate the stellar environment with its crushing pressure and intense heat. What can be done is to create a beam of one type of nuclei accelerated to the energies relevant to nuclear astrophysics. This beam is then directed to the target of the other type of nuclei involved in the reaction and a nuclear reaction yield is measured. The yield at a given beam energy as measured in the lab E'$_{lab}$ is defined as the number of reactions divided by the number of incident particles.

$$\text{Yield(E'}_{lab}) = \frac{\text{number of reactions}}{\text{number of incident beam particles}} \tag{2.33}$$

The yield can then be related back to the stellar reaction rate as will be shown next.

2.3.1 Thin Target Yields

Consider a thin target of thickness dx and area a containing n target nuclei. The effective target area is given by $a_{eff} = n\sigma$ because the target is thin and the target atoms' cross sections do not overlap. The reaction yield, Y will then be,

$$Y = \frac{a_{eff}}{a} = \frac{n\sigma}{a} \tag{2.34}$$

The number of target nuclei per unit volume, or number density N_t, is $N_t = n/(adx)$. The yield at a particular energy E' then becomes,

$$Y(\text{E'}_{lab}) = \sigma N_t dx \tag{2.35}$$

In this experiment the target is a gas of monoatomic Helium and the number density is found through the ideal gas law $n = P/(k_B T)$ where P is the pressure, T is temperature of the gas and k_B is the Boltzmann gas constant. The target in this experiment however is not thin, and so the formalism for deriving the thick target yield is required.

2.3.2 Thick Target Yields

The nuclear cross section as we have seen is an energy dependent quantity. As a beam of particles travels through a thick target they electromagnetically scatter off the target atoms and nuclei and lose energy. As a result of this energy loss resonant nuclear reaction can occur at an energy lower than the incident beam energy. The energy loss by the particles in passing through the target material is represented by ϵ and in general is also energy dependent as well as dependent on the raw number density of scattering targets,

$$\epsilon(\mathrm{E}_{lab}) = \frac{1}{N_t}\frac{d\mathrm{E}_{lab}}{dx} \tag{2.36}$$

Equivalently this can be viewed in the center of mass reference frame and then $\epsilon_{cm} = \frac{\mathrm{m}_t}{\mathrm{m}_p+\mathrm{m}_t}\epsilon_{lab}$. The thick target yield can then be obtained by integrating the thin target yield over the thickness of the target accounting for the beam losing energy as it travels deeper into the target,

$$Y(\mathrm{E'}_{lab}) = \int \sigma(\mathrm{E'}_{cm})ndx = \int_{E'_{cm}-\Delta}^{E'_{cm}} \frac{\sigma(\mathrm{E}_{cm})}{\epsilon(\mathrm{E}_{cm})}d\mathrm{E}_{cm} \tag{2.37}$$

where Δ is the total energy lost in the beam's passage through the target in the cm reference frame and $\mathrm{E'}_{cm} = \frac{\mathrm{m}_t}{\mathrm{m}_t+\mathrm{m}_p}\mathrm{E'}_{lab}$ is the energy of the beam in the cm reference frame. In the case of resonant capture the substitution of the Breit-Wigner formula, equation 2.27, into equation 2.37 gives,

$$Y(\mathrm{E'}_{lab}) = \frac{2J_r+1}{(2J_p+1)(2J_t+1)}\int_{E'_{cm}-\Delta}^{E'_{cm}} \frac{\lambda_{cm}^2}{4\pi}\frac{\Gamma_p\Gamma_\gamma}{(\mathrm{E}_{cm}-\mathrm{E}_r)^2+(\Gamma/2)^2}\frac{d\mathrm{E}_{cm}}{\epsilon(\mathrm{E}_{cm})} \tag{2.38}$$

In the case of this experiment the energy lost within the target is much greater than the expected partial widths of the narrow resonances ($\Delta \gg \Gamma$). Under these conditions the energy dependence of the partial widths, de-Broglie wavelength and ϵ is well approximated as constant and the integral has an analytic solution:

$$Y(\mathrm{E'}_{lab}) = \frac{\lambda_{cm}^2}{2\pi}\frac{\mathrm{m}_t+\mathrm{m}_p}{\mathrm{m}_t}\frac{\omega\gamma}{\epsilon_{lab}}\left[\arctan\left(\frac{\mathrm{E'}_{cm}-\mathrm{E}_R}{\Gamma/2}\right)-\arctan\left(\frac{\mathrm{E'}_{cm}-\mathrm{E}_R-\Delta}{\Gamma/2}\right)\right] \tag{2.39}$$

The labels p and t as before represent the target and projectile, with the ratio of the masses arising from the conversion of ϵ from the center of mass value to the lab value. If this yield expression 2.39 is plotted it becomes obvious that the overwhelming majority of resonant nuclear reactions occur within a small window of energy, and hence over a small range of depths within the target. The 50% yield point corresponds to the resonance energy E_R and an energy window between 25% and 75% about E_R is precisely the total width

Γ of the reaction. It is clear that the yield function has tails which extend in both directions. In theory to acquire the entire yield, $Y_{max}(\infty)$ would then require an infinitely long target and infinitely high beam energy,

$$Y_{max}(\infty) = \frac{\lambda_{cm}^2}{2}\frac{\mathrm{m}_t + \mathrm{m}_p}{\mathrm{m}_t}\frac{\omega\gamma}{\epsilon_{lab}} = \frac{\mathrm{h}^2}{4\mathrm{m}_p}\left(\frac{\mathrm{m}_t + \mathrm{m}_p}{\mathrm{m}_t}\right)^3 \frac{\omega\gamma}{\mathrm{E}_{R\,lab}\epsilon_{lab}} \tag{2.40}$$

where $\mathrm{E}_{R\,lab}$ is the resonance energy in the lab frame. However comparison of this ideal yield with practical beam energies and finite targets is still possible, Fig 2.3. Consider $\mathrm{E'}_{cm}$=E_R+$\Delta/2$ and with the resonance occurring in the center of a finite target of total energy loss Δ. The ratio between the ideal yield and the practical yield is then:

$$\frac{Y(\mathrm{E'}_{lab})}{Y_{max}(\infty)} = \frac{2}{\pi}\arctan\left(\frac{\Delta}{\Gamma}\right) \tag{2.41}$$

And thus if the energy loss in the target is at least 6 times greater than the resonance width then the yield is 89% of the entire, ideal yield.

2.3.3 Additional Experimental Factors Influencing Yields

In all practical beam delivery systems the beam is not monoenergetic, but has a small spread in energy. This small spread in energy gets further amplified as the beam passes through the target and its profile changes, an effect known as straggling. In addition the target is a gas, and the gas particles have a Maxwell-Boltzmann kinetic energy distribution which will likewise broaden the energy, termed the Doppler broadening. To properly account for these effects in the thick target yield would require convolution of the initial Breit-Wigner function equation 2.27, with the inherent beam energy spread, together with the spread from straggling and from Doppler broadening [18].

At the ISAC facility where the experiment was performed beam energy spreads δ_b have been measured to be $\sim$0.5% of the beam energy or $\sim$2.7 keV/u at a beam energy E_0= 550 keV/u [53].

The straggling δ_s can be calculated using the Bohr straggling model. The root mean square spread caused by δ_s is given by,

$$\delta_s = \sqrt{4\pi e^2 Z_p^2 Z_t N_t \Delta} \tag{2.42}$$

Evaluating this expression for a ^{40}Ca projectile, a ^{4}He target with 8 Torr pressure of gas gives: δ_s = 97 keV. Even at the lowest beam energy used in this experiment, 22 MeV, straggling contributes 0.4%.

The equation for Doppler broadening, δ_d was worked out by Bethe and

Placzek:

$$\delta_d = \left(2\frac{m_p}{m_t}\mathrm{E}kT\right)^{1/2} \tag{2.43}$$

This works out for this experiment to $\delta_d \sim 22$ keV for the highest energies (44 MeV) used in this experiment, or 0.05%.

Under the conditions of this experiment where, the total energy loss $\Delta \gg \sqrt{\delta_b^2 + \delta_d^2 + \delta_s^2}$, Gove has shown that the thick target yield remains unaffected by these energy smearing effects [54]. The target is sufficiently thick to ensure that all beam particles contribute to the integral of the cross section for a narrow resonance. The yields thus measured in the lab can accurately be used to calculate resonance strengths and thus the reaction rate.

2.4 Specifics of the ^{40}Ca(α,γ)^{44}Ti Reaction

It can happen that a single particularly strong resonance dominates the reaction rate, which is particularly true when dealing with light nuclei. However with heavier nuclei there are more nucleons and thus a larger number of available transitions. What is then more often the case is that multiple resonances contribute to the reaction rate, or equivalently the yield. It is necessary then to measure the yield over the entire Gamow window. If this is done by changing the beam energy in small energy steps, the resulting yield as a function of energy is termed an excitation function. The primary object of the analysis of this experiment was then to measure the excitation function for the ^{40}Ca(α,γ)^{44}Ti reaction.

Typical alpha-rich freezeout temperatures are $T \sim 10^9$K (usually reported as T_9). Due to the uncertain understanding of supernova physics there are no hard limits on the temperature range of interest. The most typical range of interest in alpha-rich freezeout is $1\times T_9$ to $2.8\times T_9$. The Gamow window center of mass effective energy for this experiment is $\mathrm{E}_{eff} = 2.2\times10^{-6}T^{2/3}$MeV. The alpha-rich freezeout temperature range thus corresponds to a range in center of mass energies of 2.19 - 4.35 MeV (excitation energy range of 7.26 - 9.42 MeV). The conversion factor between lab and center of mass energy is $\mathrm{m}^4\mathrm{He}/(\mathrm{m}^4\mathrm{He}+\mathrm{m}^{40}\mathrm{Ca}) = 4/44 \sim 0.0909$. In the lab frame the relevant energy range corresponds to a beam energy range of 24.1 - 47.9 MeV or equivalently in units of keV/u where u=40 atomic mass units, 602 - 1197 keV/u. The present ^{44}Ti energy scheme, derived from γ-ray studies, in the region of interest can be seen in Fig 2.4 with known spins and parities labeled. The energy listed as E_x is the excitation energy, the sum of the kinetic energy and the energy gained during fusion, the Q-value of the reaction, where Q= 5.069 MeV. Strong resonances at E_x = 9.215, 9.227, and 9.239 MeV are highlighted and were used to

guide the experiment in the initial stages.

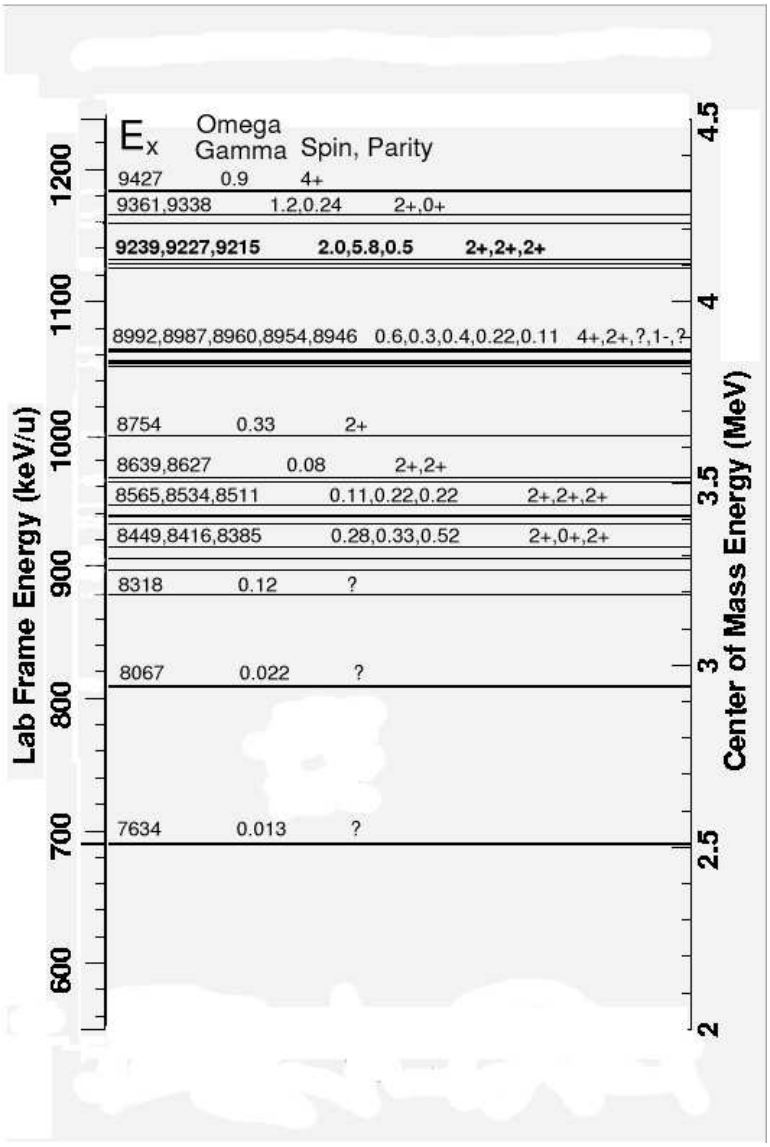

Figure 2.4. The energy level diagram for ^{44}Ti displaying resonances with known resonance strengths from previous γ-ray spectroscopy experiments [2, 3, 4, 5, 6]. Two energy scales are provided, one in the center of mass frame, the other in the lab frame. The energies listed as E_x are the excitation energy levels of the nucleus. Known spins and parities are also listed. The resonance strengths (Omega-Gamma) are in units of eV.

Chapter 3

Enter The DRAGON

As was discussed in the theory section the fusion reactions that occur in the stellar environment can be studied on Earth using particle beams of the appropriate energy. An important result that came from the theory of stellar reactions is that despite numerous collisions the probability of a fusion reaction occurring is still very small. From an experimental perspective this presents a unique challenge in distinguishing the recoil product of the reaction from the much more numerous projectiles. The technique of "recoil separation" has evolved to perform such experiments with great accuracy. The Detector of Recoils And Gammas Of Nuclear reactions, DRAGON, at TRIUMF in Vancouver B.C, is one of the premier recoil separator instruments in the world.

This chapter discusses the specifics of the DRAGON with which the yields of the ^{40}Ca(α,γ)^{44}Ti reaction were measured.

3.1 TRIUMF ISAC Facility

TRIUMF is Canada's national nuclear physics laboratory, located in Vancouver B.C. One of its experimental halls, the ISAC facility Fig 3.1, holds the DRAGON apparatus, among many others [55].

The reactions studied at ISAC are primarily performed in what is called "inverse kinematics". Inverse kinematics merely means that between the target and the projectile it is the projectile that is the heavier of the two. And so to perform the ^{40}Ca(α,γ)^{44}Ti reaction we required a beam of ^{40}Ca.

3.1.1 Offline Ion Source

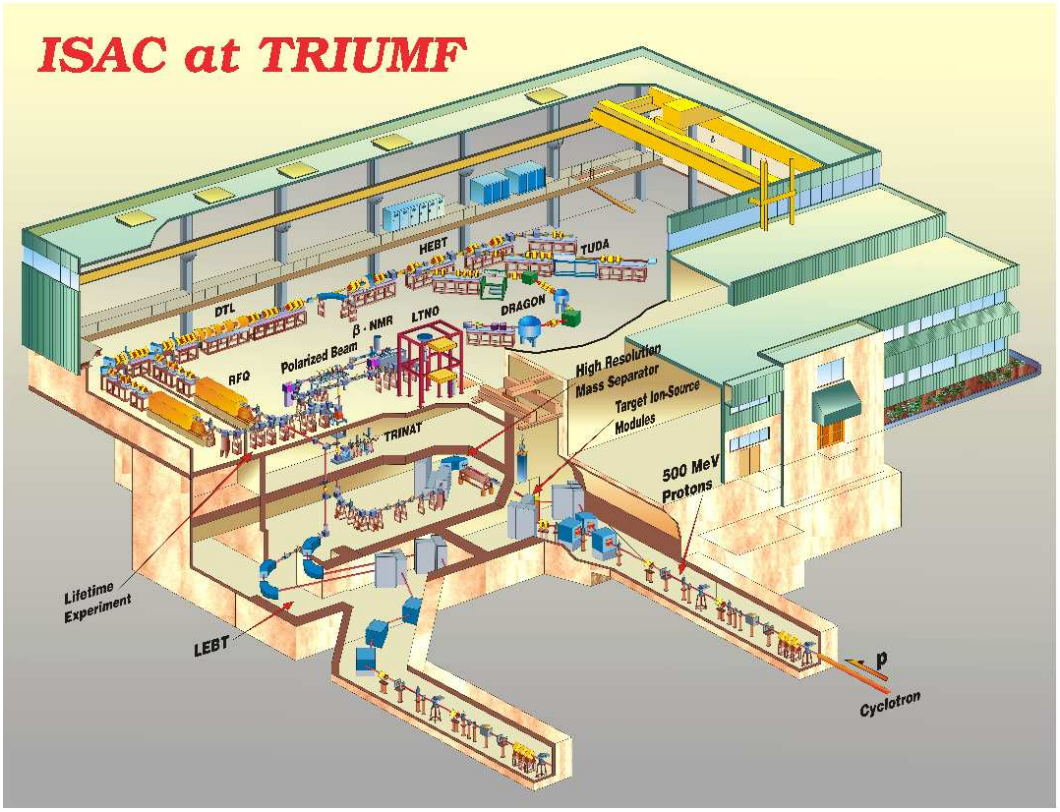

Figure 3.1. ISAC, the Isotope Separator and ACcelerator facility at Triumf. ISAC specializes in radioactive beams and DRAGON is but one of many instruments that use them.

One cannot simply accelerate neutral metallic ^{40}Ca atoms, since they need to be ionized first. Ions are required because ^{40}Ca is electrically neutral and electric fields are used to accelerate, so it needs some charge. More specifically, $^{40}Ca^{2+}$ was required because of the limitations of the Radio-Frequency Quadrupole accelerator (RFQ).

ISAC's primary mission is to produce radioactive beams, since short-lived radioactivities are often of the most scientific interest. The radioactive isotopes that compose these beams are produced with the main TRIUMF cyclotron to bombard 500 MeV protons onto an appropriately chosen target. ^{40}Ca is not radioactive and so it was not necessary to use this beam production mechanism.

Instead the Offline Ion Source (OLIS) was used to provide the initial $^{40}Ca^{2+}$ ions. When a beam is produced with the cyclotron it is termed "online" and when not, it is "offline". OLIS is essentially a micro-wave chamber where material is bombarded with microwaves until it ionizes. It is also capable of surface ionization, with an appropriately chosen material which when heated

removes electrons from powder in contact with the material [56]. The system required modifications to produce a beam of sufficient intensity and purity for this experiment; a paper is pending detailing those modifications.

3.1.2 ISAC Beam Transport and Acceleration

In general the subject of beam transport draws on a direct analogy with the field of optics. Lenses, prisms and filters to focus, deflect and remove photons have analogues in beam transport: quadrupoles, separators and slits. One significant difference from an optical test bed is that along beam transport lines conditions approaching vacuum are maintained so that the beam does not undesirably interact with matter along its trajectory.

The ions produced in OLIS are extracted by electric fields, accelerated to 2 keV/u, and a magnet is used to separate masses. A schematic of the beam transport systems can be seen in Fig 3.2. The mass separator is essentially a very large magnet. The magnetic field causes the charged particles to follow curved paths where their bending is based on their momentum to charge ratio. The species of interest is passed through metallic slits and the remaining undesired species do not continue on towards the RFQ. This is similar to the electromagnetic separation that DRAGON performs and so it will be discussed in detail in the next section. In general when beams of particles are produced in accelerator facilities these beams are not continous streams of particles, for a variety of technical reasons, the beam particles are typically bunched into small packets. Immediately after the mass separator the beam is pre-bunched into packets that arrive at a rate of 11.8 MHz before entering the RFQ. The RFQ operates within a range of mass-to-charge ratio of $1/30 \leq q/A \leq 1/6$, and hence the need for $^{40}Ca^{2+}$. The RFQ further accelerates, bunches and focuses the 2 keV/u input beam into pulsed packets separated in time by 85 ns (35.4 MHz). The beam exits the RFQ and enters the Medium Energy Beam Transport (MEBT) at 150 keV/u. Anything which does not fall within 3 times the pre-bunched frequency is removed by a chopper. Bunchers placed every 8-10 m maintain low energy spread and good total flux per unit area, "emittance".

The beam then passes through a thin carbon foil ($\sim 40 \mu g\ cm^{-2}$) which strips off further electrons to make the beam conform to $1/6 \leq q/A \leq 1/3$. This range of mass-to-charge makes it acceptable for the Drift-Tube Linac (DTL) to accelerate the beam. The DTL accelerates the beam bunches with an oscillating electric field (106 MHz) directed along the beam line. When the field changes direction, the beam bunches travel through a drift tube, and the beam is thus shielded from the portion of the electric field that would decelerate it. By adjusting the electric field strength, the DTL can deliver

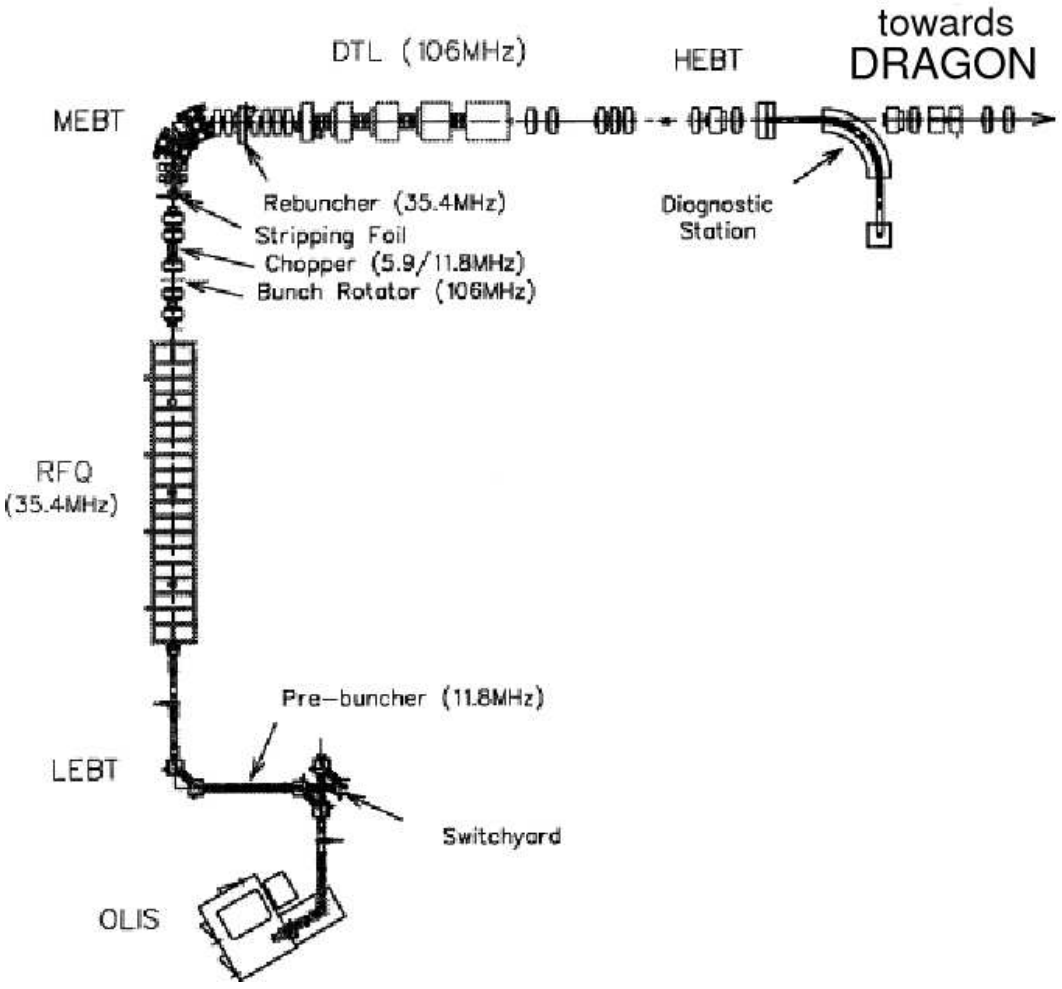

Figure 3.2. Beam transport to DRAGON at ISAC.

a range of beam energies from 153 to 1800 keV/u downstream to DRAGON with small energy spread (0.5%) [57].

3.2 DRAGON

A picture and schematic of DRAGON can be seen in Fig 3.3. A detailed overhead view of the instrument can be seen in Fig 3.4

DRAGON consists of four main components: a windowless gas target, a Bismuth Germanium Oxide (BGO or more commonly Bismuth Germanate) γ-ray detector, an electromagnetic separator (EMS) and a heavy ion detection system at its terminus [58, 53]. In this experiment the gas used is Helium and the end detector is an ionization chamber (or simply "ion chamber"). Dragon

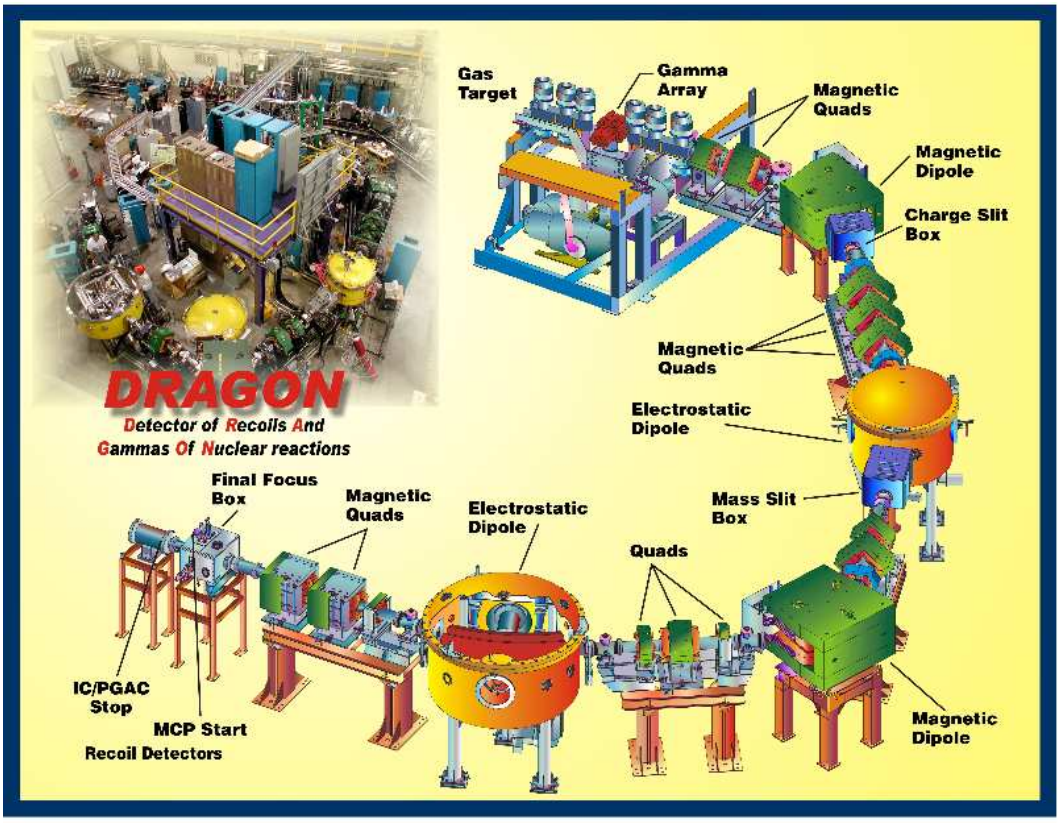

Figure 3.3. DRAGON, the Detector of Recoils And Gammas of Nuclear Reactions.

also has the capability to use Hydrogen as the target gas and the ion chamber can be substituted by a silicon strip detector.

A concise description of the functioning of DRAGON in this experiment is as follows: The ^{40}Ca beam delivered to DRAGON from the DTL enters the windowless ^{4}He gas target. The beam passes through the target and some very small fraction of the beam particles interacts via the ^{40}Ca(α,γ)^{44}Ti reaction. The γ-ray produced by this reaction is captured by the BGO array. The recoil ^{44}Ti and remaining un-reacted ^{40}Ca exit the gas target and enter the EMS. The EMS's purpose is to select out and deliver to the ion chamber only the very few ^{44}Ti recoils and get rid of the un-reacted ^{40}Ca beam. The specifics of how DRAGON accomplishes this will now be discussed.

3.2.1 Windowless Gas Target

DRAGON has a recirculating, differentially pumped, windowless gas target. It consists of a quadrangular aluminum cell, as can be seen in Fig 3.5, enclosed in a rectangular gas box. The beam enters the cell through a

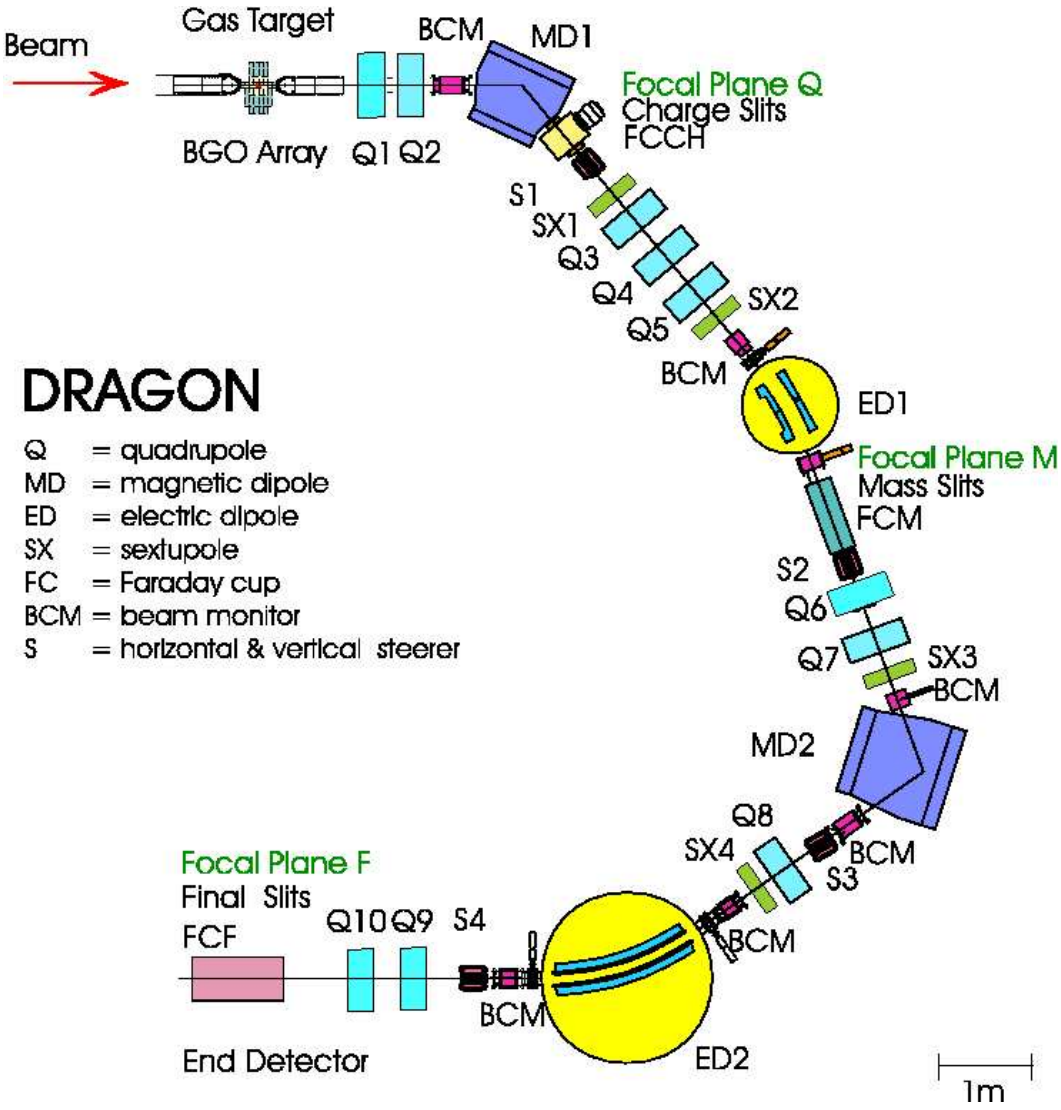

Figure 3.4. Detailed schematic of DRAGON.

6 mm diameter entrance aperture and exits through an 8 mm diameter exit aperture with 11.02 cm separation between the two. The quadrangular design of the cell was chosen so that jets of gas escaping from the entrance and exit apertures are directed away from the entrances to the differential pumping systems. The gas target is termed "windowless" because there is no physical barrier preventing the gas from escaping the cell through the entrance and exit apertures. Instead very powerful turbomolecular pumps maintain a nearly sheer vacuum-gas surface at the apertures while gas pressure (typically 1-10 torr) is kept constant through a zeolite trap. Just outside the main cell, in the gas box, the pressure is reduced by the pumping to $\sim$0.35 Torr. The pressure drops to $\sim 10^{-6}$ Torr beyond the 3rd and 4th pumping stages upstream

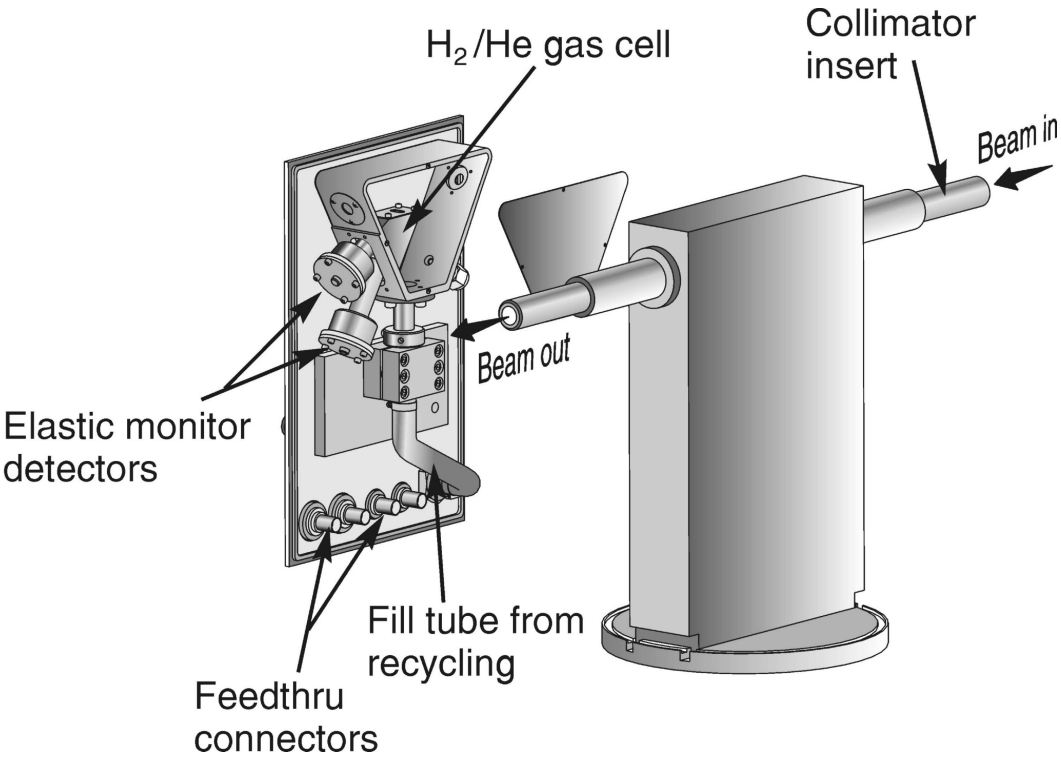

Figure 3.5. The DRAGON windowless gas target. Powerful pumping systems allow for near vacuum outside the gas chamber while gas pressure is maintained within the gas cell.

and downstream, respectively. This small amount of gas leakage still has an impact upon the effective target length a beam of particles encounters. This effective target length was measured to be 12.3 $\pm$ 0.5 cm [59]. Between each pumping stage there is tubing which has been designed to limit gas flow, and has progressively larger radii to allow a maximum recoil exit angle of 20 mrad relative to the central axis. The turbomolecular pumps (Varian V1000HT) deliver any gas that has leaked out of the cell to a Roots blower system (Leybold WSU2001, WSU501, WSU500) which then recirculates it.

The zeolite gas trap attached to the gas box is kept at liquid nitrogen temperature and acts as a molecular sieve, cleaning the gas of impurities. It also serves the purpose of a reservoir of gas, maintaining the cell pressure stable to 1% accuracy throughout data taking runs (several hours). An electronically controlled needle valve allows remote fine tuning of the cell pressure and a capacitance manometer permits pressure monitoring. Due to the high operational temperature of the pumping systems, heat exchange occurs and the gas cell temperature, which has been measured through a thermocouple, reaches 300K.

Two hollow tubes project out from the downstream portion of the gas

cell. Each of these tubes is aligned to have their axes cross at the center of the gas cell along the beam axis, one at 30^0 relative to the beam axis, and the other at 57^0. Each of these tubes contains a collimator which deflects elastically scattered Helium to a silicon detector (Ortec Ultra Cam, 150 mm^2 area). The signal from the silicon detectors, also called surface-barrier detectors (SB), allows realtime beam intensity determination.

Much akin to the carbon stripper foil in the ISAC beam line, when the beam passes through the gas target, the gas strips electrons from the beam particles and they enter a higher ionic charge state. Thus the $^{40}Ca^{+7}$ beam delivered to DRAGON from the ISAC beam line turns into a charge state distribution of higher charge states. There is a reasonably correct model explaining the profile of the charge state distribution which emerges from the passage through a gas target, known as the Sayer model, but in general it is preferable to measure it. In this experiment all charge state distributions were measured with Faraday cups.

3.2.2 Faraday Cups

A Faraday cup is a device which allows the intensity of the beam to be measured. In essence it is a metal plate with an attached ammeter. When the positively charged beam ions impact the plate they are neutralized by the electrons in the metal and a measurable current is created in the metal. For a reasonable estimate of the beam current secondary electrons that are released from the metal as the beam impacts must be caught as well. The design of the Faraday cups used at DRAGON is a cylindrical thick metal catcher with its sides surrounded by a mesh screen and preceded by an annular electrode. The mesh and annular electrode are held at a high negative bias voltage. Electrons produced by the surrounding environment (slits, collimators, etc...) are thus repelled by the mesh and secondary electrons from the beam are forced back onto the metal catcher. Ion beam currents are typically measured to within an accuracy of 1% and on the nano ampere scale. Because the beam of impinging particles may be in a higher charge state a distinction is made between "electrical nano-amps" (enA) and "particle nano-amps" (pnA). enA is the value of the current that the Faraday cup is measuring, pnA is the number of particles per second in the beam in units of the fundamental charge e. For a single charge state beam: enA = pnA $\times$ charge state.

DRAGON has numerous Faraday cups along its length in strategic positions to measure beam current at various stages. An important point for this experiment is that all charge state distributions were measured using Faraday cups. In particular the Faraday cup FC4 measured the beam delivered to DRAGON from the ISAC beam line, FC1 measured the beam immediately

after passing through the gas target and FCCH measured the beam after the first magnetic separator MD1.

An additional point to note is that while taking the experimental data the Faraday cups would stop the beam entirely from reaching the end detector, so the Faraday cups serve as devices to fine tune the separator before and after recoil data collection. During recoil data collection, the beam current is measured and monitored with the scattered target nuclei in the gas target. Typically FC4 readings for the beam intensity ranged from a few enA up to 25 enA.

3.2.3 BGO γ-ray Detectors

Surrounding the gas target is an array of 30 hexagonally shaped crystal bismuth-germanate (BGO) scintillator detectors in a close packed geometry. The BGO scintillator works along the principle that a γ-ray traversing the

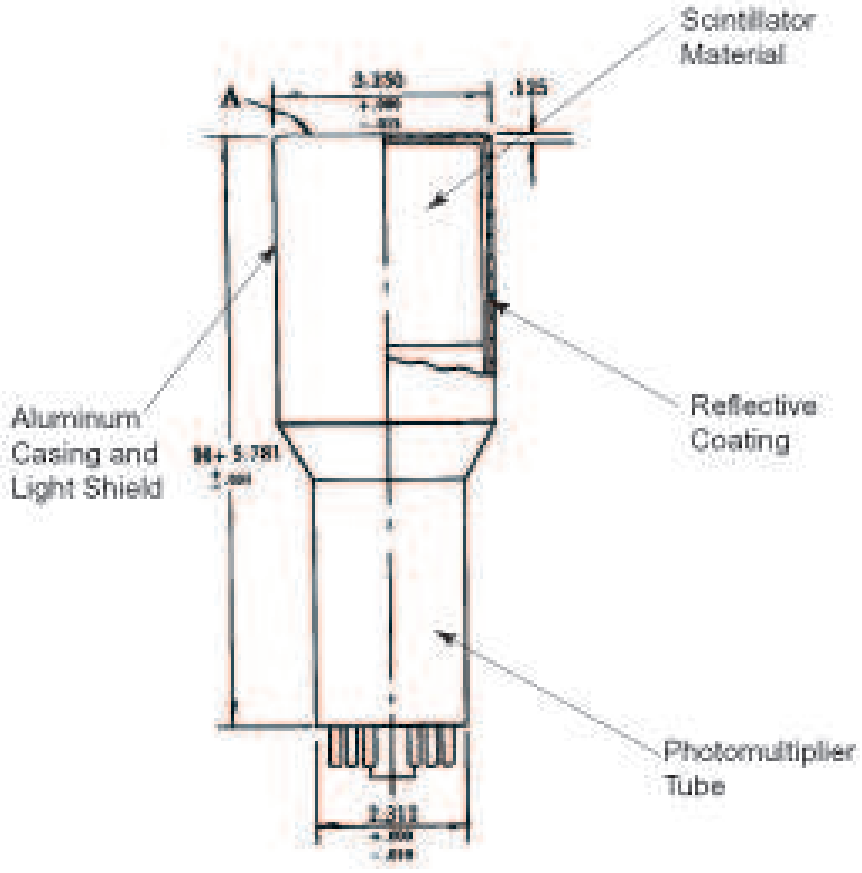

Figure 3.6. Schematic of a BGO detector.

material creates visible light as it scatters off of the electrons in the crystal. The amount of light created is proportional to the amount of energy the γ-ray deposits in the crystal. The scintillation light is then captured using a photomultiplier tube. In this device a photon impacts a metallic plate and photo-electric emission of a few electrons occurs. These electrons are accelerated towards another metallic plate by an electric field. Upon impacting this secondary metallic plate the initial few electrons liberate many more electrons due to their increased energy from the acceleration. These newly liberated electrons then proceed through another stage of acceleration towards yet another metallic plate and the process continues until the final stage of multiplication where a measurable pulse of electrons is recorded. By calibrating these devices the pulse height from the photomultiplier can be related back to the amount of scintillation light recovered and thus the energy of the initial γ-ray.

Each scintillator crystal housed in the hexagonal detector has a radius of 5.58 cm and a length of 7.62 cm. In their highly compact arrangement they are able to cover 92% of the 4π solid angle as viewed from the center of the gas target cell. Full coverage is not possible because of the beam entrance and exit pipes and the pipes to the Roots blowers. Simulations indicate that on average 60% of the time a 1-10 MeV γ-ray deposits its full energy in a single detector [60]. A ^{244}Cm/^{14}C source is used for energy calibration studies and the entire array has been determined to have a 7% full-width at half-maximum energy resolution. In these calibration studies the total efficiency for the array has been measured and simulated for a wide range of incident γ-ray energies. Simulation and measurement agree to within 10 %. In this experiment an additional method for determining the total efficiency of the detector array was used as will be seen in the analysis section.

3.2.4 Electromagnetic Separation

As was discussed in the theory section, fusion reactions typically proceed first through a short phase where the fusion product is a compound nucleus in an excited state. In the ^{40}Ca(α,γ)^{44}Ti reaction, the compound ^{44}Ti* nucleus de-excites by emission of a γ-ray and because the γ-ray is highly energetic its emission significantly impacts the momentum of the ^{44}Ti product. It is because of this significant change in momentum that the ^{44}Ti product is termed the "recoil". Consider the momentum of the compound nucleus to be $\mathbf{p}^*$ and $\mathbf{p}_r$ that of the recoil.

As seen earlier the ^{4}He nucleus in the gas target contributes negligible momentum and thus the momentum of the compound system can be very reasonably approximated as the projectile's momentum, $\mathbf{p}^* = \mathbf{p}_p = (2\mathrm{m}_p\mathrm{E}_p)^{1/2}$. The momentum of the γ-ray is given by its energy divided by the speed of light,

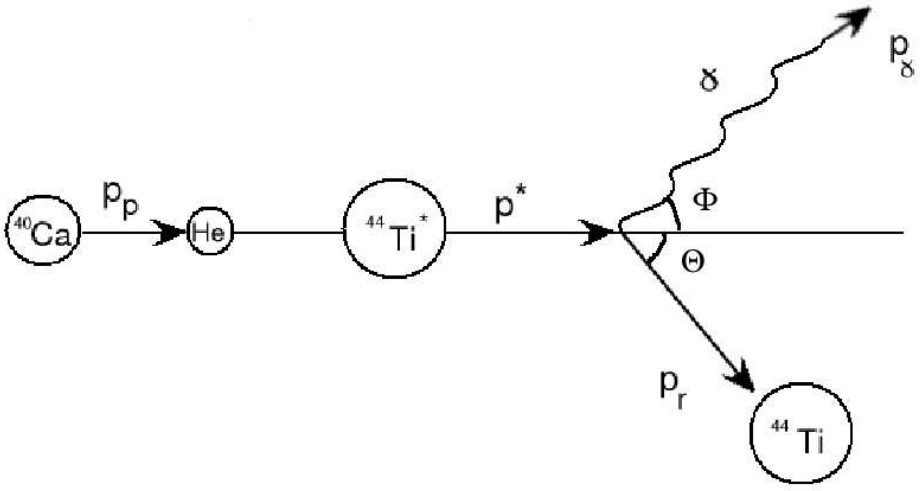

Figure 3.7. Schematic representation of the nuclear reaction as it occurs in this experiment in the laboratory frame of reference.

$p_\gamma = E_\gamma/c$. In the lab system the recoil and γ-ray part with an angle θ and ϕ respectively from the initial direction of the compound nucleus. Applying conservation of momentum before and after the de-excitation,

$$p^* = p_r\cos(\theta) + p_\gamma\cos(\phi) \tag{3.1}$$

$$0 = p_r\sin(\theta) - p_\gamma\sin(\phi) \tag{3.2}$$

From which θ can be isolated,

$$\theta = \arctan\left(\frac{\sin(\phi)}{\frac{p^*}{p_\gamma} - \cos(\phi)}\right) \tag{3.3}$$

When ϕ=$\pi/2$ the recoil angle θ is maximal,

$$\theta_{max} = \arctan\left(\frac{E_\gamma/c}{(2m_pE_p)^{1/2}}\right) \tag{3.4}$$

All recoils thus exit the target confined within a "recoil cone" of angle θ_{max} which reaches a maximum when the ratio of $E_\gamma/\sqrt{E_p}$ reaches a maximum. The energy of the γ-ray is greatest if the excited ^{44}Ti* decays directly to the ground state of ^{44}Ti, in which case E_γ=E_x= E_{cm} + Q. For the lowest beam energy (E_p= 24.09 MeV) and correspondingly highest recoil angle, θ_{max} is calculated to be 5.41 mrad, well within the acceptance angle of DRAGON (17 mrad).

The ^{44}Ti recoils acquire a momentum spread which is bounded by the situation of emission of the γ-ray in the forward direction of propagation, slowed as much as possible ϕ=0, and the reverse direction, speed up as much as possible (ϕ= $\pi/2$). Under these conditions, p_r is,

$$p_r = p^* \pm p_\gamma = \sqrt{2m_pE_p} \pm E_\gamma/c \tag{3.5}$$

At its largest this momentum spread is calculated to be $\pm$0.54%. A result which will be important in the next section is the energy of the recoil, E_r, which can be determined from squaring equation 3.5,

$$E_r = \frac{m_p}{m_r}E_p\left(1 \pm \frac{2E_\gamma/c}{\sqrt{2m_pE_p}} + \frac{E_\gamma^2/c^2}{2m_pE_p}\right) \tag{3.6}$$

3.2.4.1 First Stage of Separation

Because of the recoil cone angle, immediately following the gas target are two quadrupoles, Q1 & Q2, which focus the beam into the first magnetic dipole, MD1. MD1 is a large magnet which produces an intense magnetic field ($\sim$4000 Gauss) oriented towards the ground at a right angle to the beam path. When charged particles enter a magnetic field of strength B, they experience a magnetic Lorentz force which causes their paths to curve in a circle of radius R, which is proportional to the particle's mass m, velocity v and charge q,

$$\frac{mv^2}{R} = qvB \tag{3.7}$$

The paths of the beam and recoil particles entering MD1 thus curve in the plane parallel to the ground with differing radii because their momentum to mass ratios, or magnetic rigidity mv/q = RB are different. However, as discussed in the gas target section, as a result of the beam passing through the gas target, beam and recoils are no longer in a single charge state, since they have acquired a charge state distribution. Positioned just beyond MD1 are movable metallic plates, termed charge slits, which can be positioned to select out only the particular charge state that is desired - all the remainder impacts the plates and proceeds no further down the separator. Typically the most

populous charge state is selected, though on occasion for practical reasons another charge state may be chosen.

Because the beam ions and recoils only have a very slightly different momentum, this single stage of magnetic separation is insufficient to isolate the recoils. Another stage of separation is required, based on energy rather than charge.

3.2.4.2 Second Stage of Separation

After exiting MD1, the now single charge-state beam and recoils are brought into an achromatic focus by a triplet of quadrupoles and two sextupoles to correct for any higher order aberration. The beam then enters the electrostatic dipole ED1, Fig 3.8. ED1 consists of two finely polished metallic

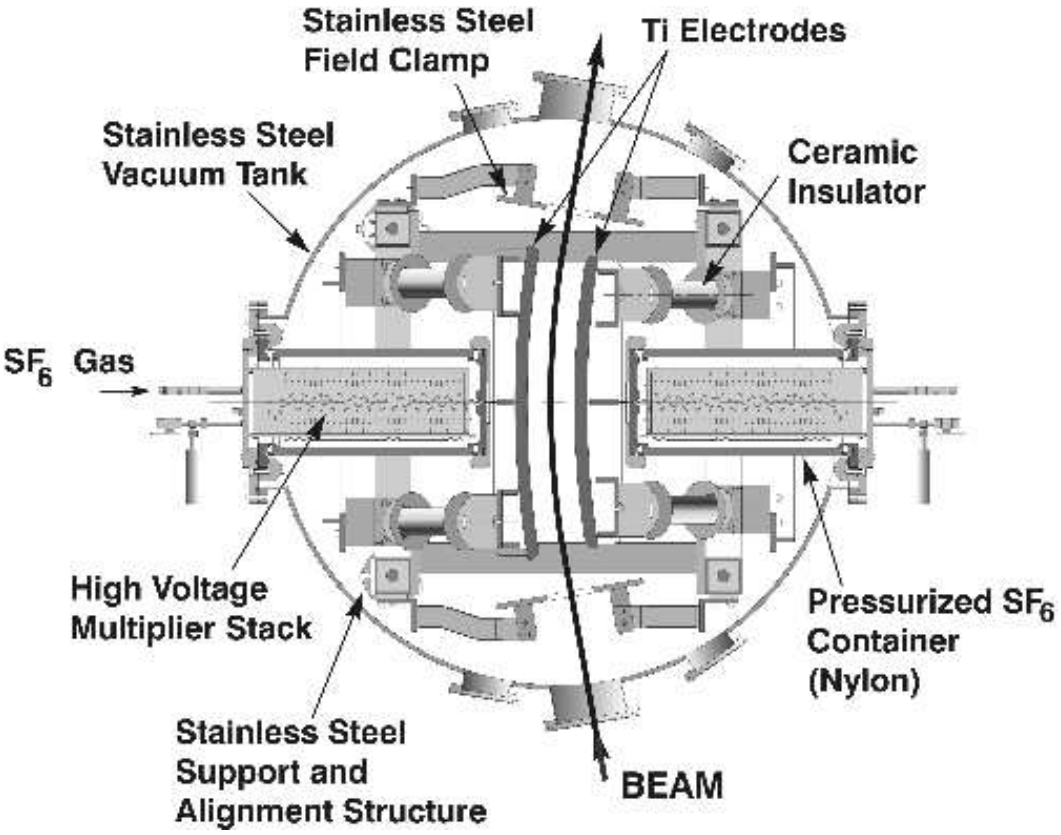

Figure 3.8. Schematic of an electrostatic dipole.

plates perpendicular to the ground that follow the beam line. These plates are charged to a very high voltage (∼100 kV), and produce an intense electric field between them directed perpendicular to the beam line. When particles of charge q, mass m and velocity v enter an electric field of strength D directed

perpendicular to their motion, they experience a radial acceleration, and thus follow a circular path of radius R such that:

$$qD = \frac{mv^2}{R} = \frac{2E}{R} \tag{3.8}$$

The paths of the beam and recoil particles entering ED1 thus curve in a plane parallel to the ground with differing radii because their energy-to-mass ratio, or electric rigidities $mv^2/q = RD$, are different. As with the first stage, positioned just beyond ED1 are movable metallic plates, termed mass slits. These plates can be positioned to select out only the particular mass of interest. The remaining unwanted components of the beam impact the plates and proceeds no further down the separator. Strictly speaking, the separation offered by ED1 is clearly based on kinetic energy, but nonetheless it is conventionally referred to as a mass separation. This is largely because the first stage separated out a charge-to-mass ratio of interest, and this second stage selects out of that population only the particles whose kinetic energy matches the mass of interest.

Substituting numbers into equation 3.6 with the lowest energy of E_p=24.09 MeV the recoil energy is $E_r \sim 21.9 \pm 0.21$ MeV which is significantly different ($\sim$10%) allowing for separation.

The subsequent sections of DRAGON are a repeat of the first and second stages with the difference that the electrostatic dipole ED2 has a larger bending radius than ED1. A final quadrupole doublet brings the recoils to an achromatic focus in the end-detector, an ion-chamber, and there exists a pair of final slits for additional beam rejection before entering the ion chamber.

3.2.5 "Leaky" Beam and Tuning

One might expect that separation after these various stages would result in a perfectly clear signal of only recoils at the end of DRAGON. This is rarely if ever the case. Under experiment conditions, some combination of energy and charge of the beam particles enables them to "leak" through even the most determined efforts to reduce it. The suppression factor is the number of beam ions reaching the end detector per second divided by the number of initial beam ions before separation. In this experiment suppression factors of 10^{-7} could be readily achieved, though even with this impressive ratio coincidence measurement are very often required to isolate the few Ti recoils from the dominant leaky beam.

The term "Tuning" refers to establishing the many magnetic and electric field strengths of the components of the separator. The various field strengths are monitored by NMR probes and electronic readouts. Because the

recoils are so few in number the separator needs to be tuned with the ^{40}Ca beam and then the settings are mathematically scaled to values which reject the beam and accept the ^{44}Ti recoils. The leaky beam can be significantly increased or decreased depending on the quality of the tune and the MD1 charge state selection. 100% transmission of the ^{40}Ca beam from the first Faraday cup to the final Faraday cup FCF was the experimental method used to determine the tune quality. While tuning, several beam centering monitors (BCM) along DRAGON were used. These are essentially a square metal plate segmented into 4 equal quadrants. When the beam impinges on a plate a measurable current is read off it. An ideal tune has an equal amount of beam landing on each quadrant, and thus the beam is at the dead center of the quadrants, passing through the central optical axis.

Beam profile monitors were also used during tuning of the separator. A beam profile monitor is essentially a set of vertical and horizontal metallic wires that are inserted into the beam line. Much like the metallic plates, when the beam impinges on a wire, a current can be read from it. The beam profile monitors have the advantage that the wire separation is constructed to be very small and so it is able to look at the physical "profile" of even a small beam spot (<1 mm diameter).

Finally a CCD camera is placed just beyond MD1, facing the optical axis upstream of MD1. When the beam hits the gas in the target, visible light is created from atomic transitions in the gas and the CCD is able to capture this light to display the beam spot.

Further specifics of tuning for this experiment will be discussed in the Analysis section.

3.2.6 Practical Limitations: Charge State Booster

At a beam energy of 47.9 MeV, the peak of the charge-state distribution (CSD) resulting from the passage of the ^{40}Ca beam through the gas target is at $^{40}Ca^{10+}$. Because of the energies of interest ED1 required a very high electric field strength to bend the recoils through the separator. At the time of performing this experiment, this was not feasible. Instead, a system was designed to position a 50-100 nm Silicon-Nitride (SiN) foil to cover the exit aperture of the gas target, Fig 3.9. Thin foils are used in almost all particle beam experiments to strip (capture) electrons from the passing beam particles. The gas in the target also strips electrons from the beam however in general a beam passing through gas will lose significantly fewer electrons than the same beam passing through a solid foil. By placing this foil after the gas target, this "boosts" or increases the charge state, hence the term "Charge State Booster" (CSB) used to describe this foil. While Carbon foils are more common in beam

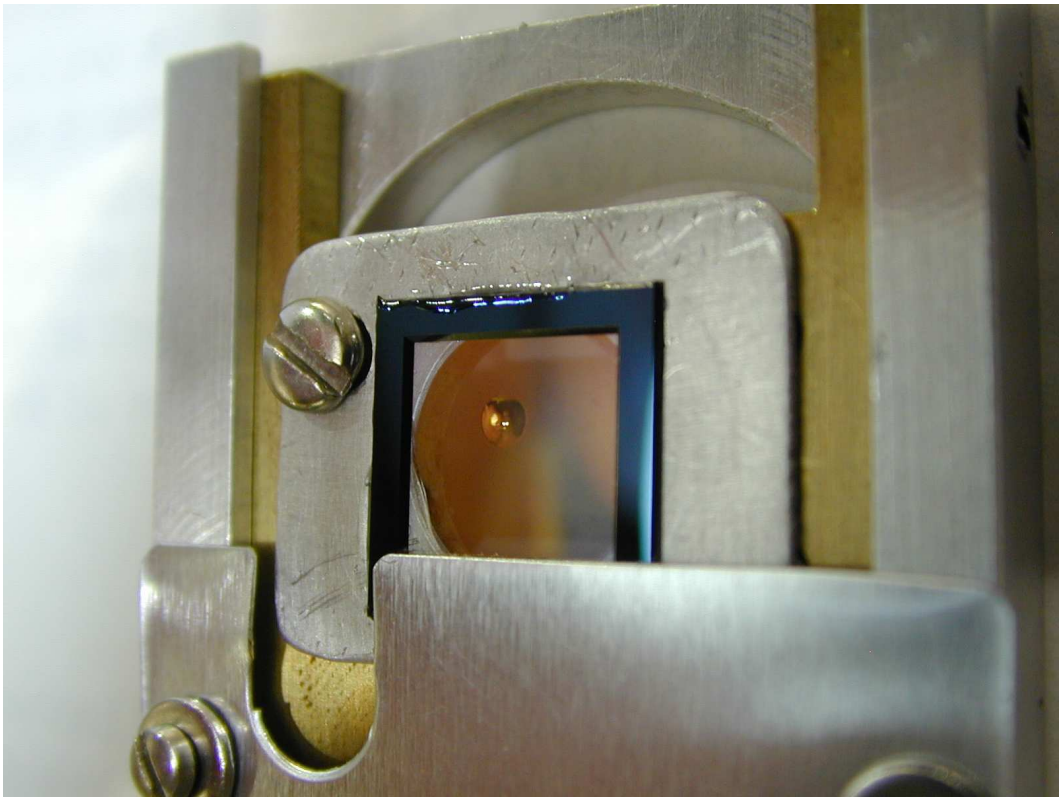

Figure 3.9. The charge state booster (CSB). The silicon nitride foil can be seen with a small patch of melting which was incurred while testing the foil's ability to handle very high beam intensities. The mounting device allowed remote control of the position of the foil in the beam line.

physics, this Silicon-Nitride foil was much more structurally robust, which was required because jets of gas from within the target chamber readily destroyed any Carbon foils. Pressures of up to 8.5 torr within the gas target could easily be achieved without having a 100 nm SiN foil break. Furthermore, compared with the carbon stripper foil used in the ISAC beam line, the Silicon-Nitride foil survived irradiation by the beam for a much longer time, a factor of three at minimum. It was found that under a 40.4 MeV Ca beam, the foils survived up to 600 pnA-hours ($\sim 10^{16}$ beam ions).

With this charge state booster, a shift in the maximum charge state from $^{40}Ca^{11+}$ to $^{40}Ca^{13+}$ for the highest beam energies was achieved, allowing for the beam and recoils to be bent through the separator. An added benefit of the charge-state booster was that the original CSD maximum of 10^+ or 11^+ does not have good separation through MD1: the m/q ratios for $^{40}Ca^{10+}/^{44}Ti^{11+}$ and $^{40}Ca^{9+}/^{44}Ti^{10+}$ are too close.

3.2.7 Ion Chamber

DRAGON can be equipped with 2 types of end detectors, a double-sided silicon strip detector or an ionization chamber (IC). In this experiment the IC was exclusively used because it provided better particle identification (based on atomic number Z) [61]. A schematic of the IC can be seen in Fig 3.10. It is essentially a large steel cylinder filled with isobutane gas. Because

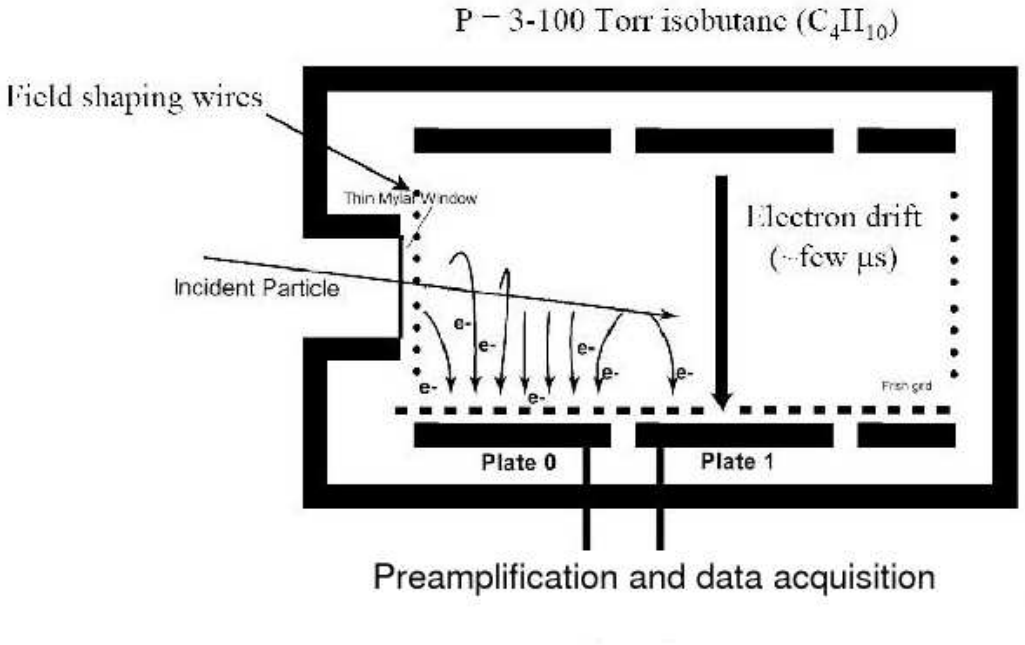

Figure 3.10. Schematic of the ion chamber end detector used in this experiment.

the beam line must operate in conditions of near vacuum the entrance aperture to the IC is sealed by a thin Mylar window (130 μg/cm^2). The Mylar window was kept very thin to minimize energy loss and straggling within its thickness, which would reduce the resolution of the IC, while remaining sturdy enough to maintain 20-30 Torr of pressure within the IC.

When beam ions and recoils pass through the isobutane gas, they ionize the molecules of isobutane, releasing electrons. An electric field (50 V/cm) accelerates these liberated electrons and positive ions towards the electrode plates within the IC. The electrons are typically on the order of a thousand times faster in reaching the plates, and so the ion signal is not used. The result of these electrons impacting the plates is a measurable electric pulse. With the strength of electric field used in this experiment, the electric pulse is proportional to the initial number of electrons liberated. Because the incoming beam and recoil particles can enter the IC at different angles the ionization will

occur at various places within the IC and the differing distances traveled by the electron shower would distort the signal. To make the signals independent of where the initial electrons are liberated a Frisch grid of wires is used. Between the cathode and the Frisch grid only a small voltage exists, just enough to move the electrons towards the grid. Beyond the grid the voltage increase is large and most of the electron shower occurs there, in this way the signals recovered from the active volume of detection are independent of the path of ionization [62].

The DRAGON ion chamber has a segmented anode, with two plates 10 cm wide and a final 5 cm plate. This segmentation allows for particle identification and isobar separation.

3.2.8 Data Acquisition Electronics

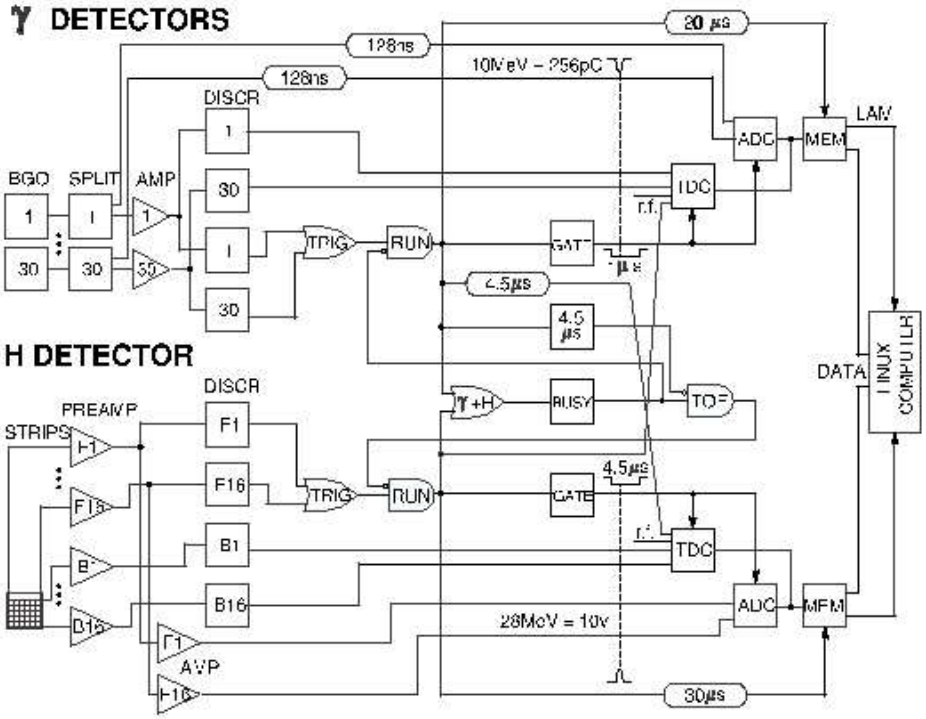

Figure 3.11. The electronics layout for DRAGON data acquisition (DAQ).

Figure 3.11 displays the electronics layout for the DRAGON data acquisition (DAQ), with detectors on the left and the acquisition computer on the right [63]. Save for pre-amplifiers, all of the electronics are mounted in racks and are standard nuclear physics electronics modules (NIM standard)

and the data they process are sent to the computer via standard CAMAC modules.

The signals coming from the 30 PMTs of the γ-ray array are separately carried by 50 Ω co-axial cable to resistive splitters; for clarity the diagram displays only the last and first PMT electronic lines. From the resistive split one branch of each signal is sent through a long co-axial cable bundle which delays it by 128 ns before reaching an analog-to-digital converter (ADC). The other branch first gets amplified by a factor of 10 and then split again. One output of the amplifier is sent to a leading edge discriminator (LED). An LED functions along the principle that only signals which cross a hard threshold produce an output; in practice this removes noise, electronic or otherwise. The other output of the amplifier is sent through an 8 MHz low-pass filter to remove noise and then to a constant fraction discriminator (CFD). A CFD unlike an LED finds the peak value of pulse that crosses a hard threshold rather than the leading edge, it is therefore a better indicator of the timing of the pulse except for at high data rates which is when an LED performs better. The CFD and LED thresholds are typically set to trigger on signals greater than $\sim$2 MeV. The CFD and low pass filter are labeled "trig" on the diagram because their output is used as the trigger for the rest of the electronics. The CFD signals are all combined in a logical OR to form a master gate trigger. When the gate is "open", over the course of a 1 μs, the TDC and ADC data from all PMTs are permitted to be read into memory (MEM), and when closed, nothing is stored. The gate also sets off a "busy" signal that holds off additional gates from being generated within 20 μs, allowing the TDCs and ADCs sufficient time to empty their data into memory.

The electronics for heavy ion detection are nearly identical. Instead of PMT outputs, the signals from the anode plates are sent to pre-amplifiers and then split after a second stage of amplification. There is also a longer gate signal, 4.5 μs, which is longer than the flight time of the recoil through the 20m of the separator. The gates from the γ array electronics and the heavy ion electronics are combined into a coincidence trigger which when open sends the data from the TDCs and ADCs into separate memory banks exclusive to coincidence events. In this way, events which trigger either the γ array or the ion chamber are stored as "singles" and when both are triggered within the 4.5 μs time window, the events are additionally stored as "coincidences".

The elastic monitor is not depicted in schematic format because its circuit is essentially the same as the heavy ion circuit and very simple. The output of the surface barrier detector is sent through a pre-amplifier, then a delay line amplifier. The signal is then split and one branch is sent to a constant fraction timing single channel analyzer (SCA). The SCA signal is used as a trigger for a gate to an ADC and TDC which read in the output of the delay line amplifier. The elastic monitor events are stored in the same

memory list as the heavy ion events but are distinguishable by their differing ADC address.

Chapter 4

Analysis

In the laboratory using DRAGON, reaction yields are the principal physical quantity measured that allow the determination of stellar reaction rates. However because the type of measurements for the ^{40}Ca(α,γ)^{44}Ti reaction are both in coincidence and use a single charge state, the equation 2.33 needs to be restated in terms of these particulars. Both the recoil charge state fraction and the γ-array efficiency must be folded into the expression for the yield. Furthermore the number of ^{40}Ca delivered to the target was measured with the elastically scattered Helium within the gas target and the relationship between the number of elastic He events to the integrated beam current needs to be likewise detailed. Therefore the equation used to calculate the yield for a particular beam energy E'$_{lab}$ is,

$$\mathrm{Y(E'}_{lab}) = \frac{\mathrm{n}_{44Ti}}{\mathrm{n}_{40Ca}} = \frac{\mathrm{n}_{Ti}}{\mathrm{n}_{sb}\mathrm{RE'}^2_{lab}\zeta_{BGO}\mathrm{C/P}} \tag{4.1}$$

Where P is the pressure in the gas target, C is the recoil charge state fraction, ζ_{BGO} is the detection efficiency of the BGO array, n$_{sb}$ is the number of elastically scattered He events recorded by the SB detector and R is a coefficient of proportionality. n$_{Ti}$ is the number of ^{44}Ti recoils detected in coincidence at a particular charge state, and hence n$_{44Ti}$ = n$_{Ti}$/ζ_{BGO}C.

In the following sections the precise determination of all these quantities will be discussed. Additionally the stopping cross section is necessary for the conversion of a yield to a resonance strength (equation 2.40) and this was likewise measured. The chapter concludes with the excitation function and reaction rate in the energy region of astrophysical interest. The data used in this analysis were taken over the course of four beam times in August 2005, September 2005, November 2005 and March 2006.

4.1 DRAGON Tuning

The delivery and quality of the ^{40}Ca beam to DRAGON was the duty of the ISAC operations group. Past the first Faraday cup (FC4) the beam transport was the duty of the DRAGON experimenters. It is the ISAC operations group that sets the beam energy upon request by the DRAGON experimenters. However the DRAGON group independently measures the beam energy using MD1.

An iterative procedure before each recoil data run was performed. All of the field strengths for the various components of DRAGON were set and monitored with the aid of a computer program, EPICS, customized for TRIUMF and DRAGON control systems [64]. With no gas in the target and the CSB removed, the quadrupoles Q1 and Q2 were set to their standard setpoints. 100% transmission between FC1 and FC4 was checked. Perfect 100% transmission of the beam through the gas target was not always possible and was corrected for in the analysis. The vertical charge slits downstream of MD1 were then closed to a 2 mm aperture width. By observing the readout from the slits the value of the MD1 field strength was then adjusted so that the beam passed through both the horizontal and the vertical slits down the center of the optical axis of the separator.

A particularity of this experiment compared to previous experiments with DRAGON was that the beam's physical profile was incredibly thin, due to the low energy spread resulting from of the relatively high mass of the projectile. Under optimal run conditions the beam easily passed through the 2 mm aperture after MD1 at an energy dispersed focus without even a low energy tail of the energy distribution landing upon the slits. With gas in the target however the physical spread of the beam was increased to the point where the readout from the slits was measurable and the beam could be further centered by balancing the slit readouts.

After centering using MD1, the CSB was put in position and gas introduced into the target chamber. The value of MD1 was adjusted for the energy loss in the gas and CSB so that the beam was once again passing through the center of the slits. The beam's profile was then observed using the profile monitor, and using the CCD the beam spot was checked to be centered. Quadrupoles Q1 and Q2 were then turned off and the profile, beam spot and charge slits were checked for any large deviations (>3 mm). Deviations occurred if the beam being delivered from ISAC had an entrance angle greater than 1 mrad relative to the central optical axis, and if that was the case the ISAC operations adjusted their beam and the procedure was iteratively repeated until the entrance angle was satisfactory.

The remaining field strengths downstream of MD1 were scaled using

the scaling program according to the field of MD1. Transport of the beam to the final focus is then a matter of fine tuning using steerers, beam centering monitors and Faraday cups. 100% transmission to the final Faraday cup, FCF, was achieved for every recoil data run. Data collection lasted many weeks and it was necessary to completely retune the separator only infrequently. After large energy changes it was required but in general the scaling program performed admirably.

The value of MD1 was used to measure the beam energy according to the following formula,

$$\mathrm{E'}_{lab} = c_{mag}\frac{\mathrm{B^2q^2}}{\mathrm{m}_p} \tag{4.2}$$

c_{mag} was experimentally determined to have the value $(4.827 \pm 0.003)\times10^{-4}$ keV amu Gauss^{-2}. The energy loss in the CSB was found using this formula comparing the beam energy with and without the CSB in place. The energy loss in the gas was similarly found and measurements at different pressures lead to the stopping power as will be discussed in section 4.7.2.

4.2 Data Reduction

The data that streamed in from the data acquisition electronics (DAQ) and much of the EPICS readout were processed into a MIDAS formated ASCII file. The MIDAS .mid file was then converted into an initial .root file with custom conversion software developed by a DRAGON postdoctoral fellow Jonty Pearson. ROOT is a powerful analysis program for physics experiments based on the C++ programming language, and all of the histograms in this work were produced with ROOT (for more information on ROOT http://root.cern.ch). The initial .root file held the data in a container class called TSubEvents. A customizable program, TDragonSelector.C, then read through the TSubEvents and constructed histograms which graphically displayed the data.

For the purposes of running the experiment this method of displaying the data was good and sufficient. For the purposes of analysis however it was too time consuming. Changing a single data cut meant having to re-process the entire data set. The recoil data set was 722 root files ranging from several megabytes each to several gigabytes. Processing a single change to the data on the best computer available at TRIUMF at the time took over a week of continuous running. To remedy the situation DragonSelector was modified to output the data in tree format.

A tree data architecture is a very efficient way of organizing data for subsequent retrieval. Each data type has a branch, and each data event is a leaf. When processing the data the entire tree need not be loaded into memory,

only the branches of interest.

The coincidence events were sorted into event-based trees - where each coincidence event had a branch with the associated gamma-ray energy and reconstructed γ direction, time-of-flight, pulse width of the first IC plate signal, and the signals from both IC plates (only 2 plates were used, refer to section 4.3). The singles data had branches with the amplitude of the signals from both IC plates and the width of the first IC plate signal. With this data structure processing the entire data set required minutes rather than a week, to reprocess.

Only the highest quality recoil data were considered for this work. Out of 722 data files, 270 were identified with recoils and of those only 184 runs were agreed upon as sufficiently high quality to be used in the excitation function. The selection criterion was based upon a careful perusal of the logbook entries related to each run as well as manual scan verification of the EPICS data within the runs.

4.3 Recoil Determination

The readouts from all three plates in the ion chamber could potentially be used for particle identification. However, two plates were found to be sufficient for the purposes of this experiment. The gas in the ion chamber was set to high enough pressure that the entirety of the beam stopped before reaching the third plate. Experimentally this was $\sim$20 torr at the highest energies and $\sim$ 17 torr at the lowest.

Theoretical description of what happens when an ion stops completely within a target is complicated, and a complete description goes beyond the scope of this work. The situation can be easily described in general terms however. As the positively charged beam particle slows down in matter, more and more energy is deposited per unit path length. The energy loss as a function of depth goes through a peak, termed the Bragg peak, where the beam particle loses most of its energy. Near the end of its trajectory the charge of the beam particle decreases as it picks up electrons, eventually becoming neutral. For the energies of interest to this experiment ($>$ 0.6 MeV/u), the Bethe-Bloch formula describes the energy loss per unit length within the gas of the ion chamber above the first plate,

$$\frac{\mathrm{dE}}{\mathrm{dx}} \sim \frac{4\pi e^4}{\mathrm{m}_e}\frac{\mathrm{Z}_p^2}{\mathrm{v}_p^2}\left(N_A\rho_t\frac{\mathrm{Z}_t}{\mathrm{A}_t}\right)\ln\left(\frac{2\mathrm{m}_e\mathrm{v}_p^2}{I}\right) \tag{4.3}$$

where the subscripts, t, p and e again refer to the target, projectile and electron. I is an empirical parameter to describe the average excitation and ion-

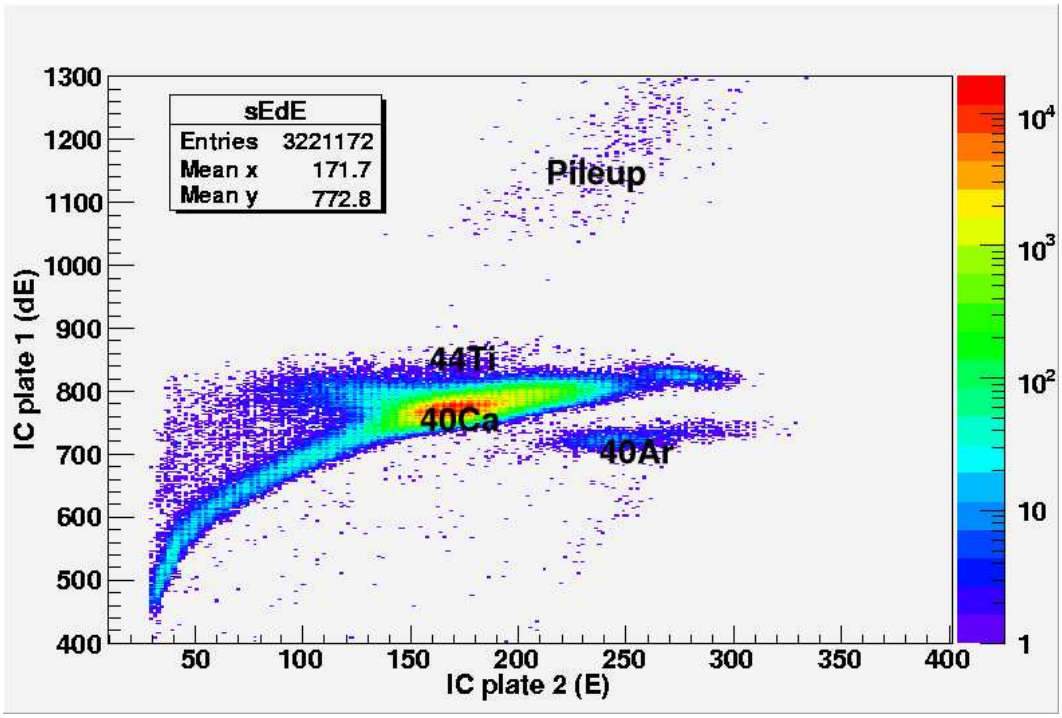

Figure 4.1. The EdE plot of the events recorded uniquely by the ion chamber, singles data, for run 15963 (1005 keV/u beam energy). This is a typical run where the ^{44}Ti peak is completely obscured by the tails of the very large ^{40}Ca leaky beam peak. Also visible is the Argon contamination peak and pileup events due to the high rate. The x and y axes were left uncalibrated, after a number of impractical calibrations of the scale it was found that the repeated adjusting of the pressure in the IC over the course of data taking made these calibrations irrelevant for particle ID.

ization potential of the gas and ρ is the gas density. Because the energy of recoil and beam particles are very similar the nuclear charge squared (Z_p^2) is the discriminating factor in particle identification on the first plate, and this is the reason why there is separation between the populations of leaky beam and recoils.

To visualize this, the signals from the first and second plate are plotted in x-y format. This is termed an EdE plot for particle ID where the first plate is dE, displaying the minimal energy loss of the particles according to equation 4.3, and E is the energy deposited in the gas region spanned by the second plate showing the bulk of energy loss. A sample plot can be seen in Fig 4.1.

As described earlier, the DRAGON separator is very good but not perfect and the leaky beam clearly dominates the singles EdE spectrum. Also seen is a small contribution from Argon contamination and pileup. Noise, either electronic or from some physical source, is easily discriminated away

because it is of far too low energy compared to the beam and recoils.

4.3.1 Pileup Discrimination

As discussed earlier the pileup events are electronic signals which, because of too high an incoming beam rate within the IC, happen to produce overlapping pulses. Pileup occurred only in small quantity and in few runs. It accounted for less than 0.6% of the singles data of all data taken. It can be distinguished from the data proper by looking at the pulse height vs the pulse width, where pileup events are clearly larger in one or the other as seen in Fig 4.2. After the coincidence requirement, time of flight and γ-energy cuts were applied only 50 pileup events in all 184 data runs were found.

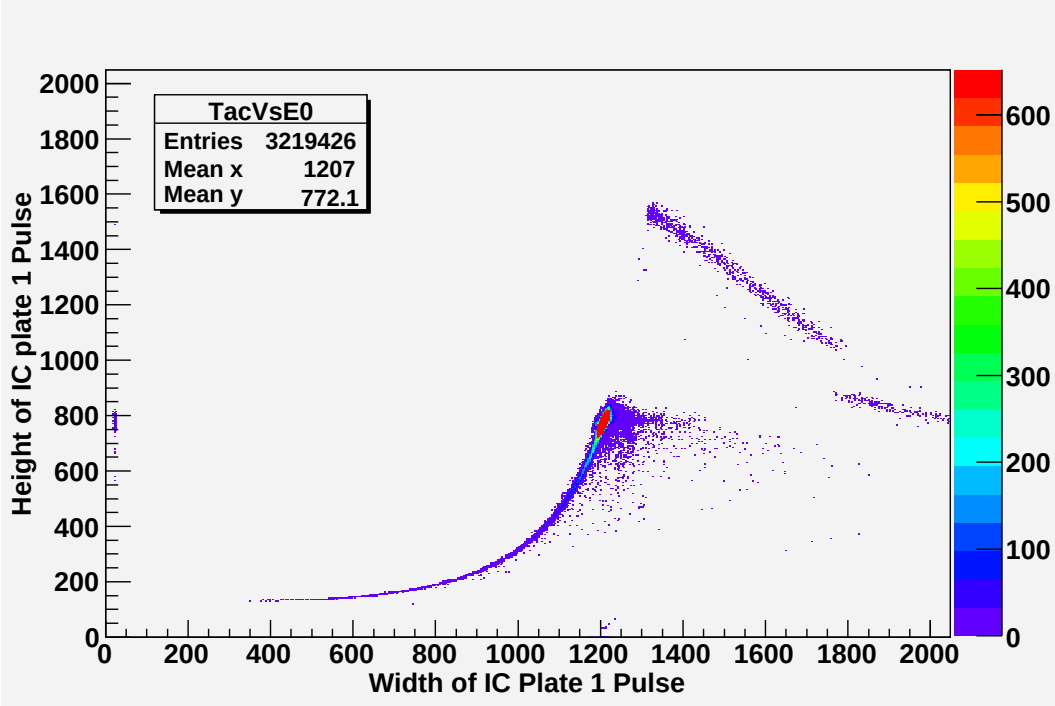

Figure 4.2. Pileup discrimination Fig, pulse height vs. pulse width on the first IC plate. The beam events are centered on the red region in this Fig. The pileup events are clearly distinguished as pulses with either too much pulse width, pulse height or a combination of both.

4.3.2 Beam Contamination

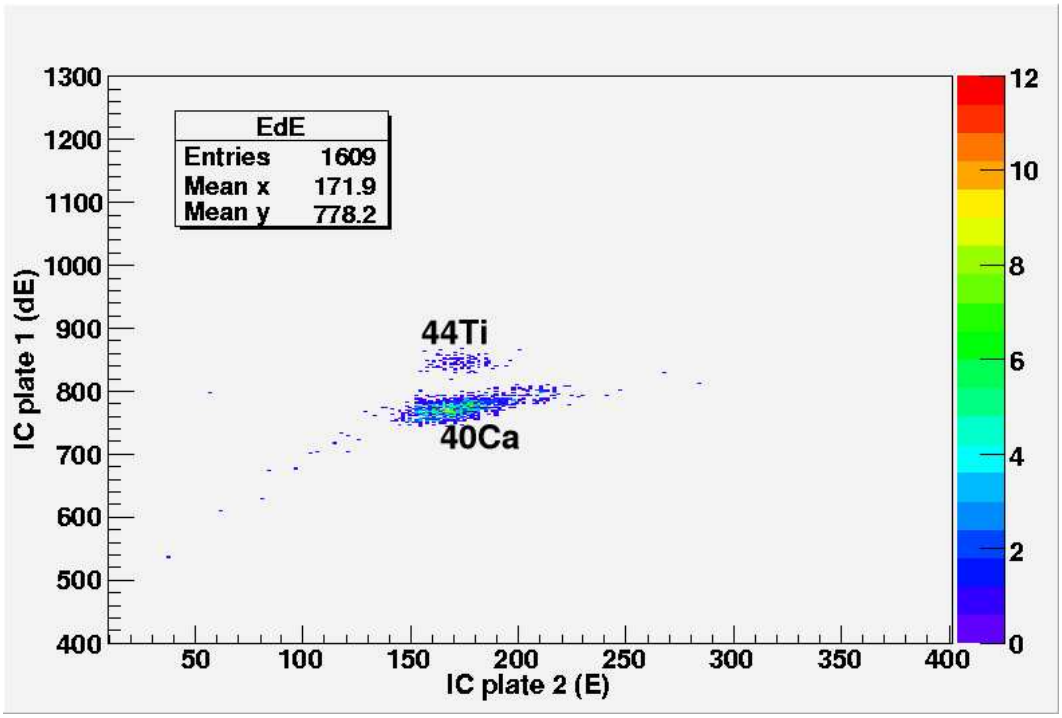

Figure 4.3. The EdE plot with the coincidence condition applied for the same run as Fig 4.1. The ^{44}Ti population becomes visible when looking at the coincidence EdE plot, as the leaky beam is further suppressed. The scale is the same as 4.1, the units are arbitrary.

^{40}Ar is an omnipresent inert noble gas that easily diffuses and has much the same charge-to-mass ratio as ^{40}Ca, and therefore it is reasonable to expect some contamination of the beam. The ^{40}Ar/^{40}Ca contamination ratio was measured to be $(1.0\pm0.4)\times10^{-4}$ during August 2005, $(4.4\pm0.3)\times10^{-3}$ during September 2005, $(6.8\pm0.3)\times10^{-3}$ during November 2005 and $(2.88\pm0.06)\times10^{-2}$ during March 2006. These ratios were measured by tuning the ^{40}Ca beam through to the IC and then taking a ratio of the two populations as measured by their separation in the IC. Because the raw beam intensity is much too high for the IC to handle, the beam intensity was first attenuated by putting filters downstream at the source. These filters are essentially porous metal plates where some fraction of the beam particles make it through their holes. No other trace of possible contaminant species was found.

4.3.3 Coincidence Requirement

When the EdE plot is viewed with only the IC events in coincidence with a γ-ray within the 10 μs time window, the ^{44}Ti recoils become apparent

as seen in Fig 4.3. Leaky beam is suppressed on average over all 184 good recoil runs by a factor of ∼265.

4.3.4 Time of Flight

The time difference between detection of a γ-ray in the BGO array and the

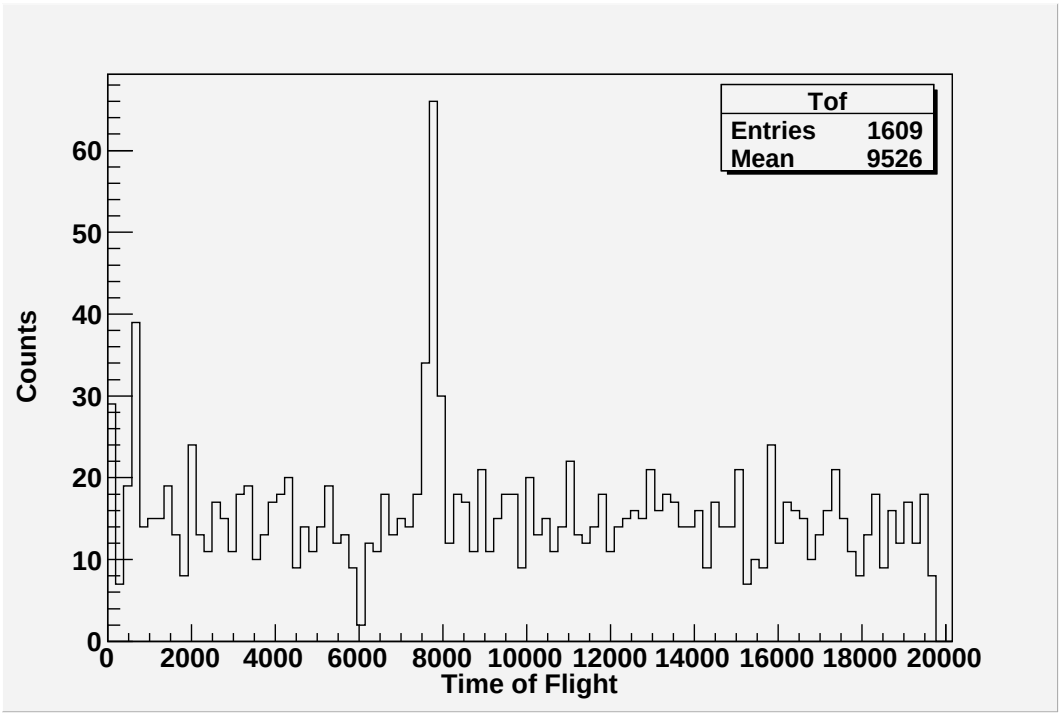

Figure 4.4. The leaky beam events in the IC that occur within a 10ms time window, with a random lab background γ-ray, form the flat background in this spectrum. The ^{44}Ti recoils have a distinct time of flight through the separator and thus create a peak in the time spectrum. 20000 channels correspond to $\sim 20 \mu s$.

detection of an event in the IC was a constant if the event was a ^{44}Ti recoil. This time difference was the time necessary for the ^{44}Ti recoil to travel the length of the 22 m of the separator, the time of flight. For events that are not recoils this time difference is essentially random, and so the time spectra for coincident events display a recoil peak on a random background. Figure 4.4 displays a characteristic time spectrum.

The data cut on the time of flight much like the recoil peak was chosen to be quite large so as to not lose any recoils: 2000 channels compared to the peak width of 200 channels but fully encompassing even the tails of the largest recoil time peak. Figure 4.5 displays the time for only events that qualified as recoils through the other cuts.

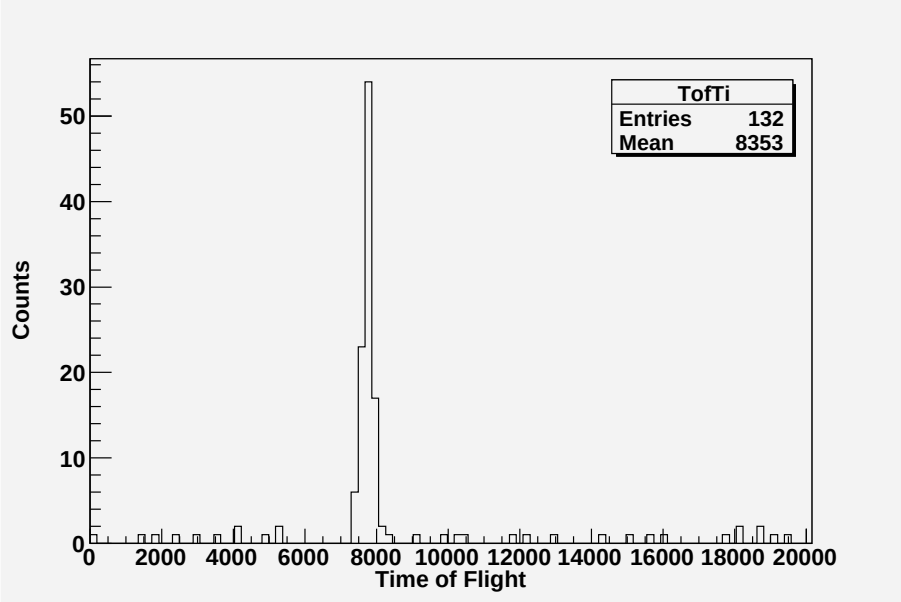

Figure 4.5. This Fig shows the time of flight of all events within a 100x100 channels wide box centered upon the Ti peak in the EdE coincidence window. 20000 channels correspond to $\sim 20\mu$s.

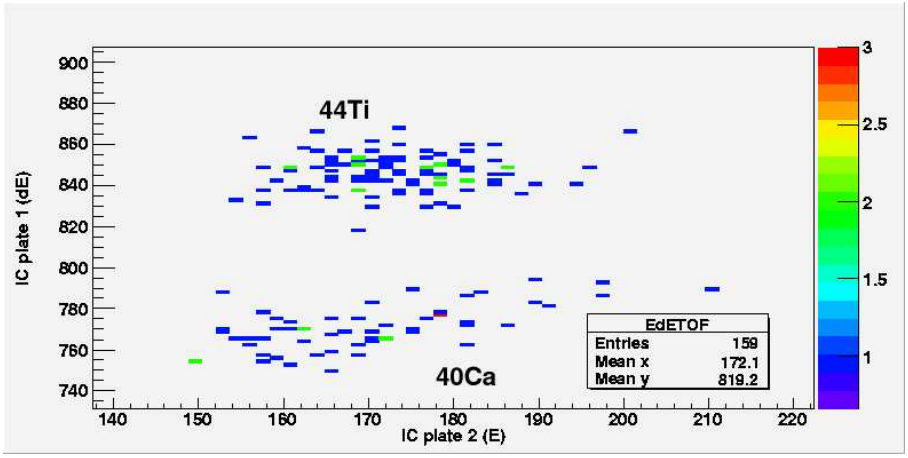

Figure 4.6. The EdE plot with the coincidence and time of flight cuts applied for the same run as Fig 4.1. The coincidence and time of flight cuts together remove almost all but the ^{44}Ti recoils. Some leaky beam can still be seen but it is clearly distinct from the recoils. The units are arbitrary.

The cut on the time of flight further suppressed the leaky beam events by an average factor of $\sim$10.4 above and beyond the coincidence cut. The EdE spectrum with both coincidence and time of flight cuts can be seen in Fig 4.6.

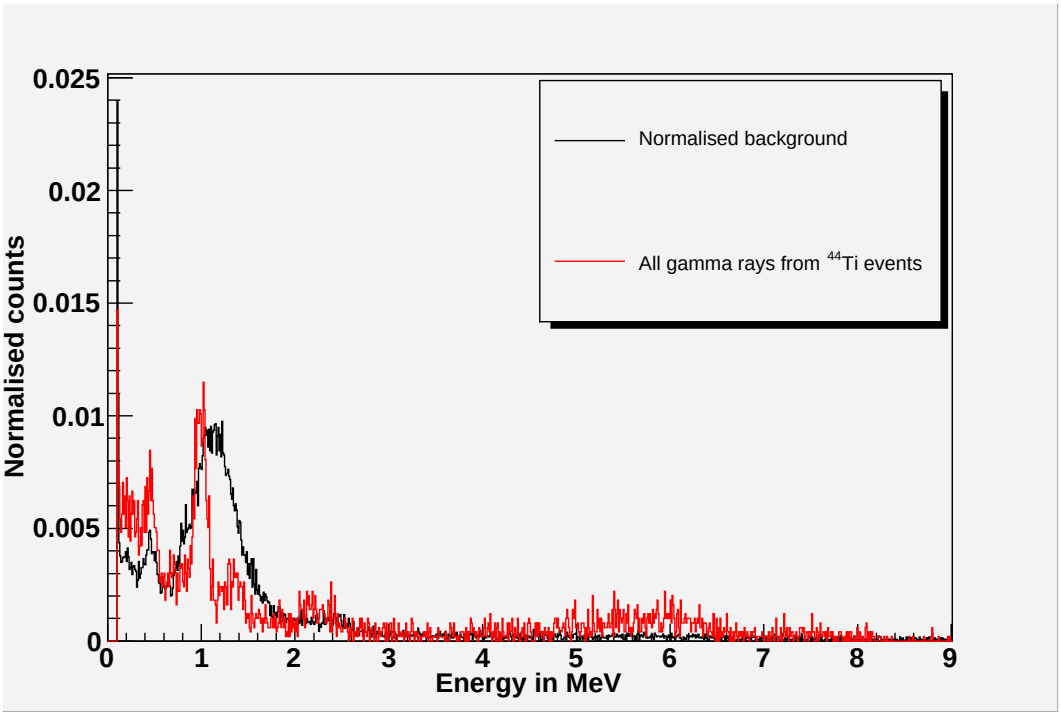

Figure 4.7. All γ-rays in coincidence with ^{44}Ti that survived the other cuts. The background spectrum is composed of all remaining BGO events. The 1.1 MeV transition from the 1st excited state to the ground state is the only clearly visible γ-ray line.

4.3.5 γ-ray Spectrum

The γ-rays detected also provide an additional cut to the data. The sum of the de-excitation gamma-ray energies should not be greater than the sum of the Q-value for the reaction plus the center of mass kinetic energy. This cut was not very stringent. Applied last, it accounted for excluding 1.3% of those events identified as recoils without the cut. Figure 4.7 displays the energy spectrum for the γ-rays that were in coincidence with all the recoils that survived all the cuts. The features of the spectrum are not sharp due to the small number of events, only 4963 events in total. The only clearly visible line is the 1.1 MeV de-excitation of the 1st excited state to the ground state of ^{44}Ti. Also plotted in Fig 4.8 are the highest and second highest energy γ-rays detected. The triangular arrangement of the data is characteristic of a decay from an excited state, where the energy of the secondary γ-ray is limited to the remaining energy of excitation.

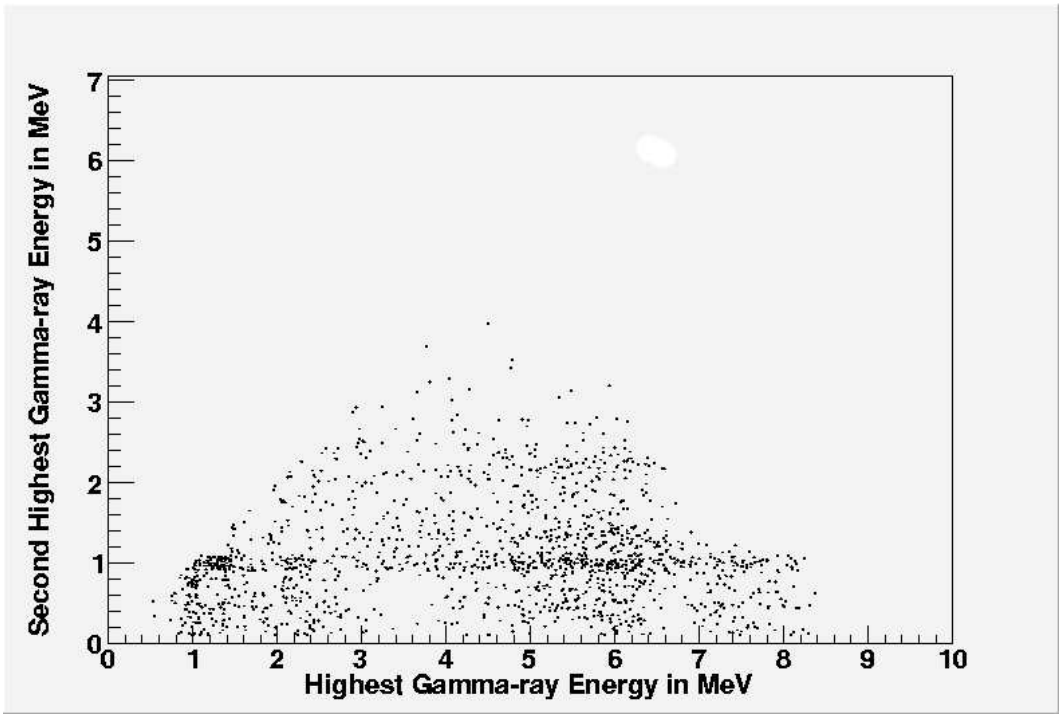

Figure 4.8. Most energetic compared to the second most energetic γ-ray in coincidence with ^{44}Ti that survived the other cuts. The sharp slope to the data on the right hand side is due to the fact that the second γ-ray can only be as energetic as the remaining excitation energy.

4.3.6 Final Tabulation of Recoils

After all cuts have been applied, the centroid of the Ti distribution in the EdE plot was tabulated for each run. This was done both with a peak finding program to find the Ti peak and with visual verification. The visual verification was facilitated by organizing the singles, coincidence and coincidence + time of flight EdE histograms on a single display window, so that there was no mistaking which peak was ^{44}Ti and which was leaky beam. The most numerous ^{44}Ti peak width was 30 channels wide. Because this experiment was to be the first measurement of this energy region for this reaction, the decision was made to try and include as many possible recoil candidates and use a very loose cut in the EdE spectrum. An x-y box 100x100 channels wide was centered on the tabulated centroid (roughly three standard deviations wide). The sum of all the events that fell within that box was the number of ^{44}Ti for that run, n_{Ti}.

4.4 Beam Normalization

Under the run conditions during data collection the number of ^{40}Ca ions being delivered by ISAC to DRAGON was for the most part very constant, and stable. A typical rate spectrum vs. time can be seen in Fig 4.9.

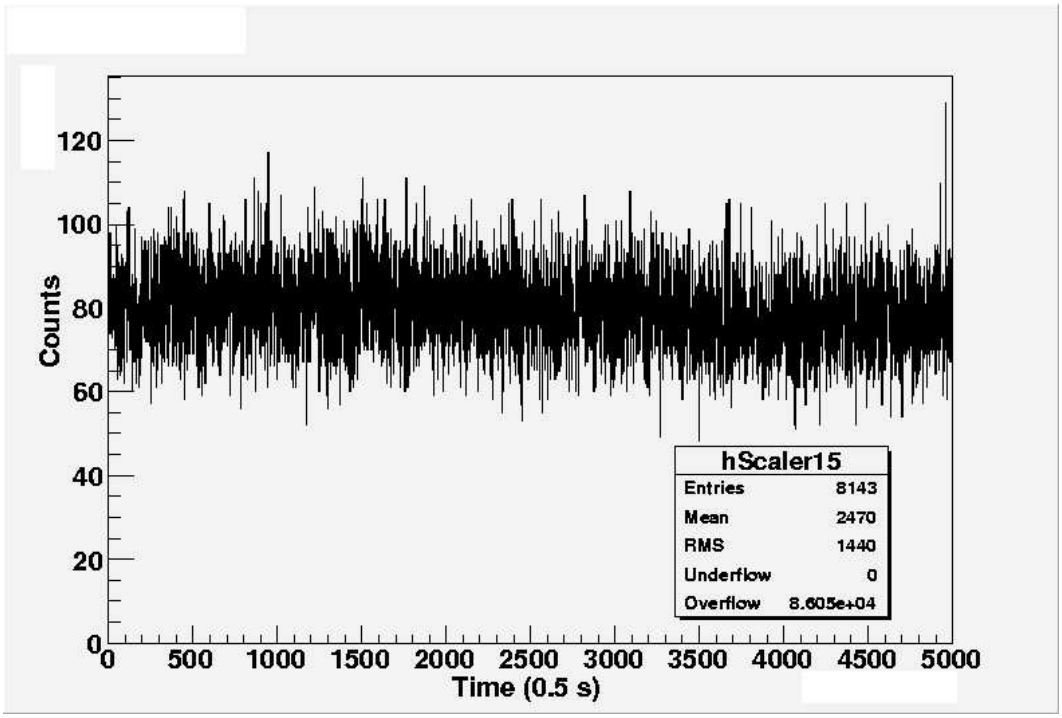

Figure 4.9. A sample spectrum of the rate of events collected by the elastic monitor, a surface barrier detector positioned at 57^0 within the gas target. This rate is not directly proportional to the beam intensity because of noise and electronic pulser signals. However the elastically scattered ^{4}He represents the largest fraction of the rate and so it was used as a diagnostic tool to monitor beam intensity.

However, vagaries in the source production, carbon stripper foils slowly being burned away and other experimental realities meant that the beam was never completely ideal. By using the realtime elastic monitor, mounted at 57 degrees to the beam axis within the gas target, all of these irregularities and different pressures from one run to the next can be accounted for and the integrated number of incident ^{40}Ca easily calculated.

Because ^{40}Ca is relatively heavy and the beam energies are moderate to high the elastically scattered Helium is well separated in energy from any background, as seen in Fig 4.10.

For many runs an electronic pulser was set up, for the purpose of verifying that the surface barrier detector was still functional, and the pulser signal

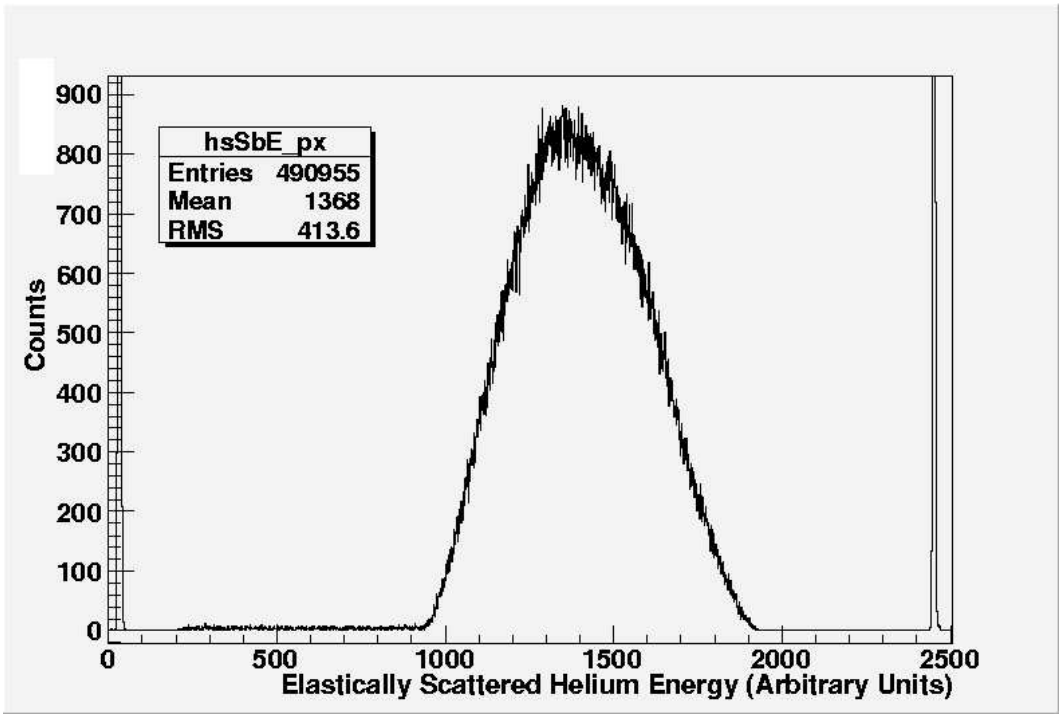

Figure 4.10. The elastically scattered ^{4}He forms the large central peak in the surface barrier detector readout. The far left peak is noise, most of which is removed by a lower level discriminator. The far right peak is an electronic pulser, used to monitor the SB detector is functioning.

was at the right edge of the spectrum. To determine the number of elastically scattered ^{4}He, n_{sb}, it sufficed to integrate the spectrum above background and below the pulser.

At the beam energies used in this experiment the scattering of the Helium nuclei into the surface barrier detector follows classical Rutherford scattering theory: it is proportional to the pressure and inversely proportional to the energy squared. The following "R-parameter" (or "R-value") was thus a constant between runs of different pressure and energy,

$$R = \frac{I/q}{e}\frac{\Delta tP}{n_{sb}E'^2_{lab}} \tag{4.4}$$

where I is the beam intensity as measured with Faraday cup FC4, q is the charge state of the beam (7^+), Δt is the time interval over which the beam is constant, P is the pressure, E'_{lab} is as before the beam energy in the lab frame, and $e = 1.6\times10^{-19}$ C. Clearly from previous discussion the Faraday cup FC4 cannot be in the beam line when making these measurements. However, before each data run, FC4 measurements were made. If the beam was constant

as measured on the Faraday cup, the number of elastically scattered particles n_{sb} was counted over a 2 minute time interval Δt in the ensuing data run and compared to the Faraday cup reading, because the Faraday cup provided a direct measure of beam intensity. The resulting R-values were plotted and a fit performed to determine the constant, Fig . The final R-value used in this analysis was R = 1743 ± 179. Small correction factors for dead-time, and

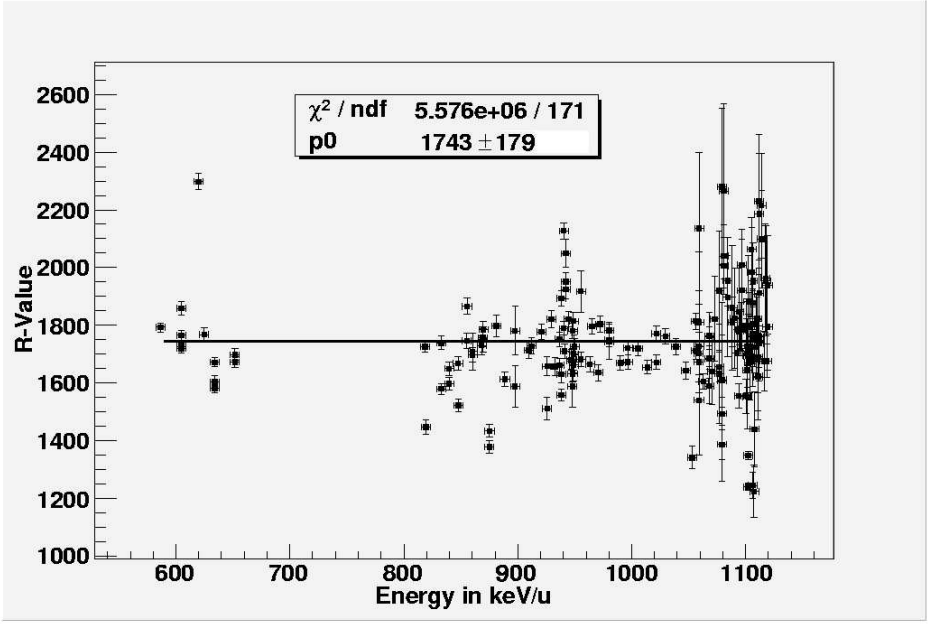

Figure 4.11. The R-value fit for beam normalization. The data points correspond to different runs. Error bars are statistical. The gap in energies correspond to runs where the R-value was discrepant as a result of a malfunctioning SB detector (see section 4.4.1).

argon contamination and transmission efficiency were included in this value as well. Dead time arises essentially from the data rate being quite high. A scaler monitors the amount of triggers presented to the DAQ versus the number actually acquired and stored, the ratio of which is the dead-time. Many runs were used in the calculation of the R-value, and not simply good recoil data runs, because all that is important in the R-value calculation is the SB detector functioning correctly. The error bars are root mean square (RMS) errors applicable to a counting experiment.
As part of the run procedure, individual runs were terminated when $\sim 2\times10^5$ elastic ^{4}He counts were recorded or more than 200 recoils in the coincidence spectrum.

4.4.1 Normalization With Damaged SB Detector

The method for determining the R-value described in the preceding section was applicable to 89% of the recoil data. For 20 recoil runs however, a damaged surface barrier detector was unintentionally used. What damaged the detector remains unclear, but it exhibited a double-peaked spectrum in energy, Fig 4.12, and calculation of the R-value indicated the counts were no longer proportional to the intensity of the beam, which was only discovered after the runs were completed. These runs stretched from 830 keV/u to 648 keV/u.

Fortunately part of the run-plan procedure was to record the value of FC4

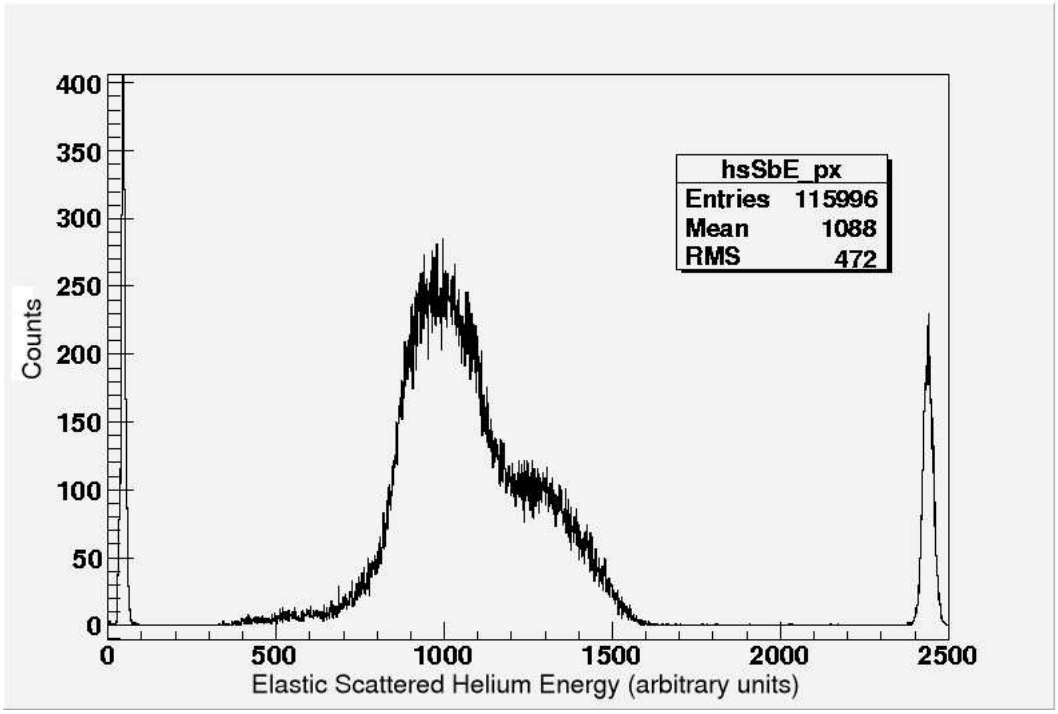

Figure 4.12. Same plot as Fig 4.10. The damaged surface barrier detector exhibited odd double peaking and tails.

before each and every run. Instead of using the SB detector to monitor the beam intensity the leaky beam was used. The total beam delivered to the target was then related in direct proportion to the FC4/(initial leaky beam) ratio and the total leaky beam,

$$\mathrm{n}_{40Ca} = \frac{\mathrm{I/q}}{\mathrm{e}} \frac{\mathrm{n'}_{leaky}}{\Delta \mathrm{t}} \mathrm{n}_{leaky} \tag{4.5}$$

where I, q and e are defined as before, $\mathrm{n'}_{leaky}$ is the number of leaky beam

events within Δt=120s and n_{leaky} is the total number of leaky beam events over the course of the run. An IC deadtime correction was also included.
To verify that this method worked, it was compared to runs that had the good SB detector, and a direct correlation between the two methods was found, see Fig 4.13.

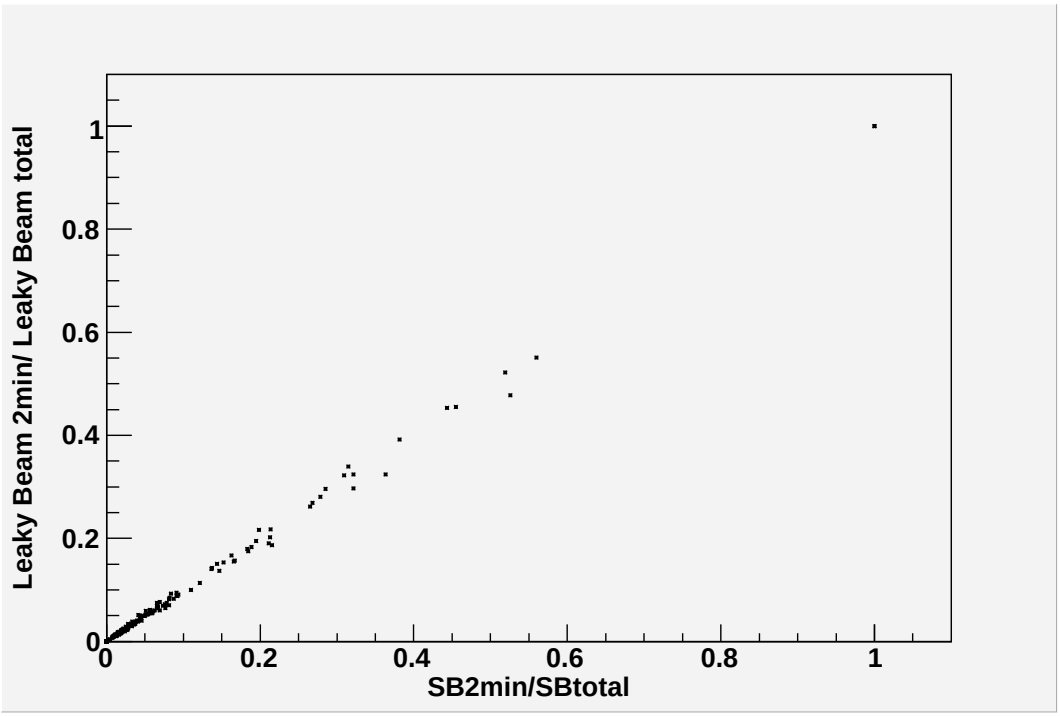

Figure 4.13. The correlation plot between the leaky beam method of measuring the total beam delivered and the method based upon elastically scattered particles using the properly functioning SB detector. The leaky beam intensity is essentially random from one run to the next but its intensity is clearly proportional to the primary beam intensity.

4.5 BGO Array Efficiency

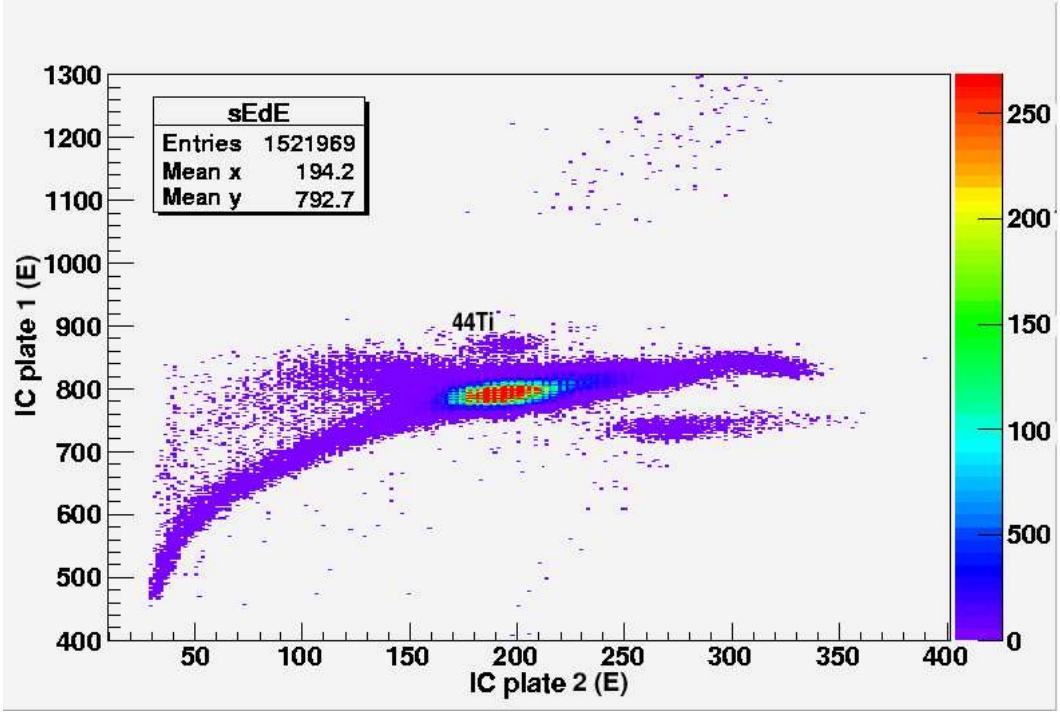

Figure 4.14. The EdE plot for a run where the ^{44}Ti was occasionally visible in the singles spectra. This occured only when the leaky beam was particularly low. These runs allowed for an absolute determination of the γ-array efficiency. The energy units are arbitrary.

In a small number of runs, the suppression of leaky beam by the electromagnetic separator was sufficient to discriminate the ^{44}Ti recoils in the singles spectra, without the need for any cuts as seen in Fig 4.14. Because the ion chamber is very nearly 100% efficient and ion transmission to the end detector is very nearly 100%, these runs offer the opportunity to directly measure the total γ-array efficiency by comparing the singles to coincidence ratio,

$$\zeta_{BGO} = \frac{\text{number of } ^{44}\text{Ti in coincidence}}{\text{number of } ^{44}\text{Ti in singles}} \tag{4.6}$$

This number of Ti was calculated with the same method as before, summing all counts that fell within a box centered at the Ti peak position (as seen with all the other cuts applied). Ideally, if this comparison is to be a proper measure of efficiency, then the ratio of various portions of the ^{44}Ti peak in the EdE plot should be the same. To gauge this, the window (box) size centered on the

recoil peak was increased and decreased. The ratios were found to be largely independent of window size, and lends great confidence to this measurement, see Fig 4.15. A fit to a constant was performed over the first 18 runs which represent beam times in August 2005 and September 2005 and as well a fit to a constant was performed for the last 18 runs which represented the November 05 and March 2006 beam time. The values of ζ_{BGO} were found to be 0.5 $\pm$ 0.1 and 0.8 $\pm$ 0.1, respectively. It can be seen that during the last series of

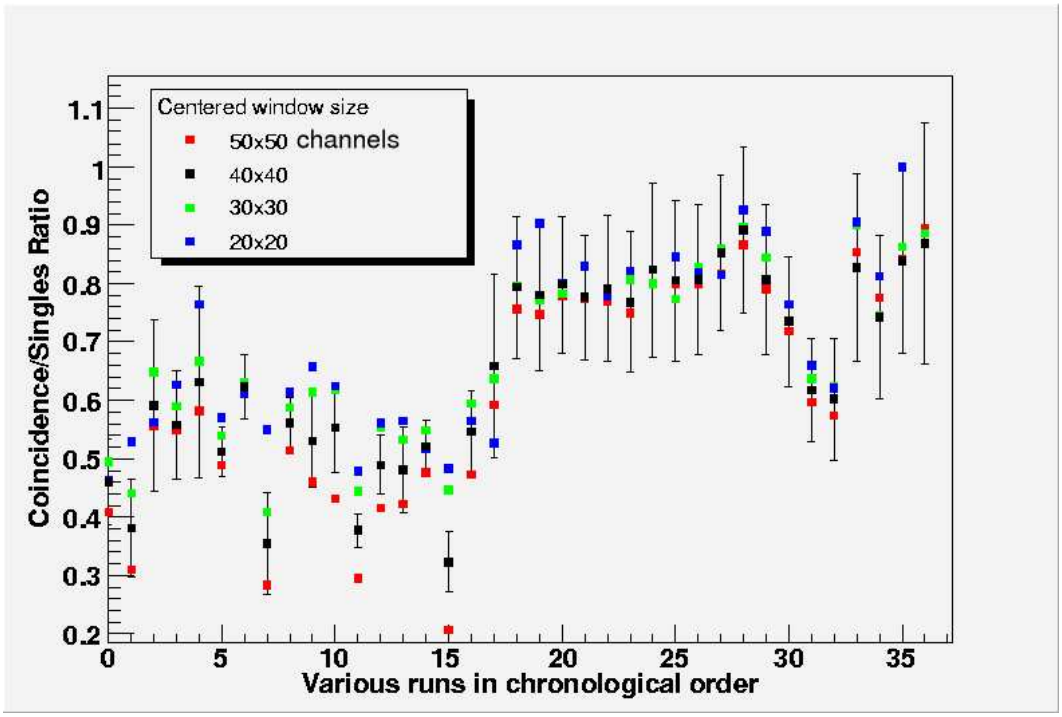

Figure 4.15. The ^{44}Ti coincidence/singles ratio for various EdE window sizes. The error bars ploted are the RMS of the counting statistics for the 40x40 channels window. The larger window sizes naturally include more leaky beam in the singles and the ratio is in general correspondingly lower.

recoil data runs the efficiency of the γ-array was considerably higher. This was due to the hardware threshold for triggering a coincidence event having being decreased. Initially one might expect a lower threshold to reduce the efficiency, allowing for more random coincidences with room background. However, there is also a trade-off with identifying lower energy γ-rays from the decay of the excited recoil ^{44}Ti*.

4.6 Recoil Charge State Distributions

A significant amount of empirical theory exists describing charge state distributions of beams of particles traversing matter. However, all describe uniquely the passage of beams through gas or solid targets, and to the knowledge of this author none adequately describes the effects of beams passing through both a gas and a solid, as is the case with the DRAGON gas target with the charge state booster (CSB) in the beam line. The situation was further complicated by the fact that a small quantity of the gas managed to leak behind the CSB. It was therefore deemed necessary to measure as best as possible the charge state distributions (CSD).

4.6.1 Interpolation Between Measurements

The charge state distribution of a beam of charged particles passing through matter naturally depends upon the electronic structure of the beam particles rather than the nuclear structure. In that sense the nucleus' only role in the CSD is to define that electronic structure. This means that even though in this experiment the interest is in knowing the CSD of radioactive ^{44}Ti we can use a stable beam of ^{48}Ti because ^{48}Ti has all the same electron orbitals as ^{44}Ti.
In May 2006 the charge state distributions for a $^{44}Ti^{9+}$ beam were measured using a very nearly pure ^{48}Ti beam.
The CSD was measured at a variety of target gas pressures and at 4 different beam energies (537, 706, 826 and 934 keV/u), both with and without the CSB. A sample of the charge state distributions can be seen in Fig 4.16, and the remaining data may be found in the Appendices. The measurements were accomplished by measuring the beam intensity at Faraday cup FC4 (right before the gas target), then measuring the intensity at FC1 (right after the gas target), and finally measuring the intensity at FCCH (right after MD1) which was scaled for the appropriate energy and selected charge state. The charge slits were kept open wide to $\pm$ 45 mm for all these measurements, since there was a significant difference in magnetic rigidity between the various charge states. The ratio of FCCH/FC4 gave the charge state fraction of the selected charge state, which was then corrected by the transmission ratio of FC1/FC4. The charge state fraction did not need to be adjusted for contamination, as there were no contaminants detected in the beam. Linear interpolation was then used to determine the recoil charge state fraction, C, of equation 4.1 at the energy and charge of interest, and an example can be seen in Fig 4.17. Uncertainties were taken from the fit values and were roughly 5%.

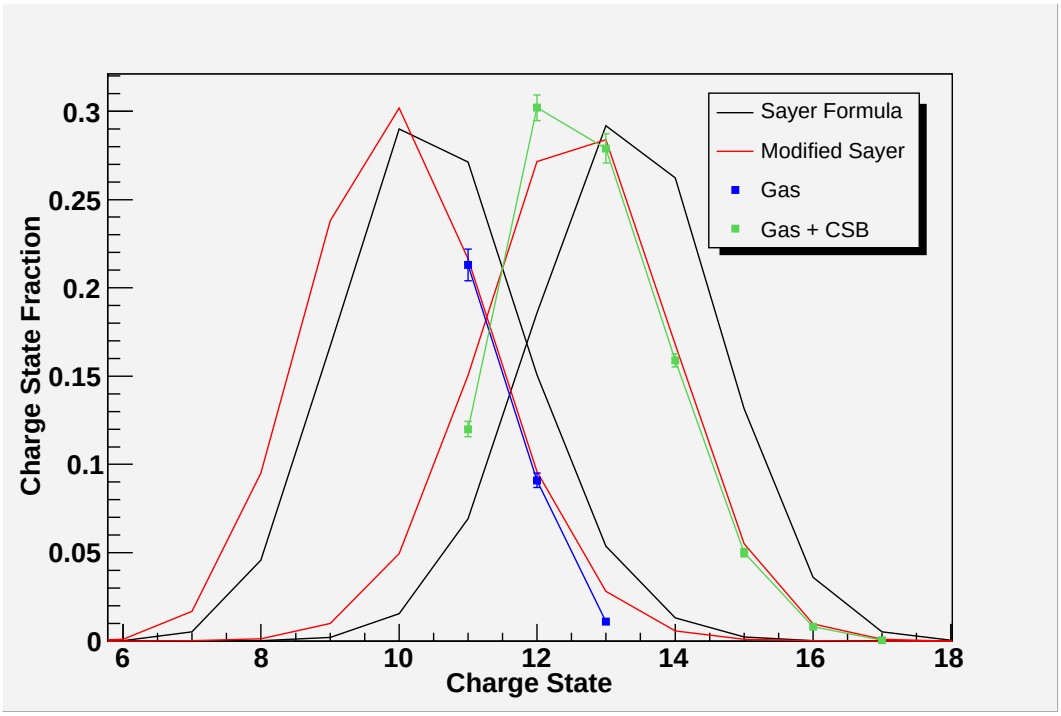

Figure 4.16. Charge state distributions for ^{48}Ti beam at 826 keV/u. The blue data were taken with 2 torr of gas in the target and the green data with 4 torr. The Sayer model charge state distributions failed to accurately represent the data. Once the mean charge state was scaled in Sayer's formulas, reasonable agreement between the data and models was found. The model distributions to the left are for a purely gas target whereas the model distribution to the right are for a purely solid target. Note the effect of the charge state booster in increasing the mean charge state compared to purely gas.

Measurements without the CSB were taken at various pressures to determine the equilibrium charge state distribution. Essentially beyond a certain thickness of gas in the target the charge state fractions no longer vary, and reach equilibrium. Equilibrium was experimentally found to occur within 1-2 torr, as can be seen in Fig 4.18. All ^{44}Ti recoil data described in this thesis were taken at pressures well in excess of equilibrium conditions (4-8+ torr).

The beam was in the 9^+ charge state to mimic the incident ^{40}Ca in the 7^+ charge state. Furthermore a kinematic factor must be included to relate the energies at which the charge state distributions were measured to the energies at which the ^{44}Ti recoil data were taken. The Newtonian formula for kinetic energy is $E = \frac{1}{2}mv^2$. Because of the unit conventionally used, keV/u, the energy is thus equal to half the square of the velocity, $E\ (keV/u) = \frac{1}{2}v^2$. Therefore the physics of a ^{48}Ti beam passing through a target with 537 keV/u of energy is equivalent to that of a beam of ^{44}Ti passing through a target with

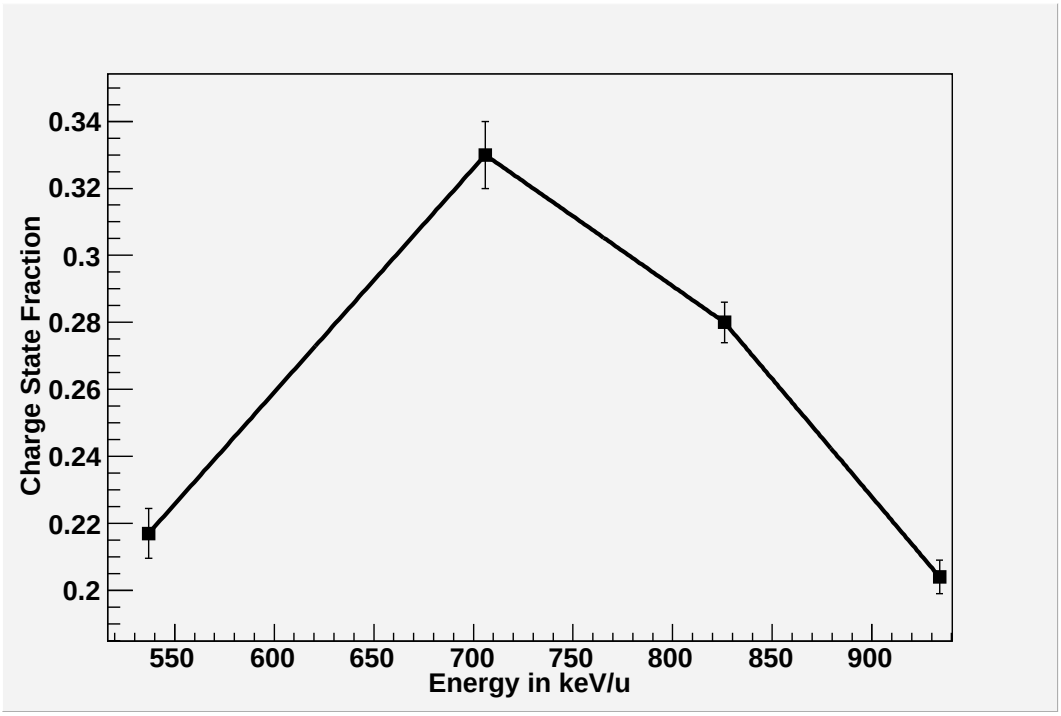

Figure 4.17. Energy interpolations done for $^{48}Ti^{12+}$ beam charge state fractions. The charge state fractions are the average over all equilibrium measurements at that energy with the charge state booster.

537 keV/u, since they have the same velocity and electronic structure. However, equation 3.6 must be used to compare the recoil energy to the incident ^{40}Ca beam energy. Because of the keV/u convention this works out to being a factor of $\sim 44^2/40^2$. Thus a charge state fraction measurement made at 530 keV/u with ^{48}Ti corresponds to an incident ^{40}Ca beam energy of ∼641 keV/u. Because of time constraints, some 10% of the recoil data taken fell outside of the energy interpolated regions. It was thus necessary to extrapolate the charge state fractions for those data using empirical theory.

4.6.2 Extrapolation With Theory

The Sayer model is an empirical model which essentially describes the charge state distribution for a monoenergetic beam of particles passing through either a solid or a diffuse gas target by an asymetric Gaussian function [65]. It uses 3 parameters: q_0 the mean charge state, essentially the Gaussian width ρ, and a term that introduces the asymetry of the Gaussian, ϵ. If F_q is the charge state fraction of charge q and F_m is the maximum charge state fraction

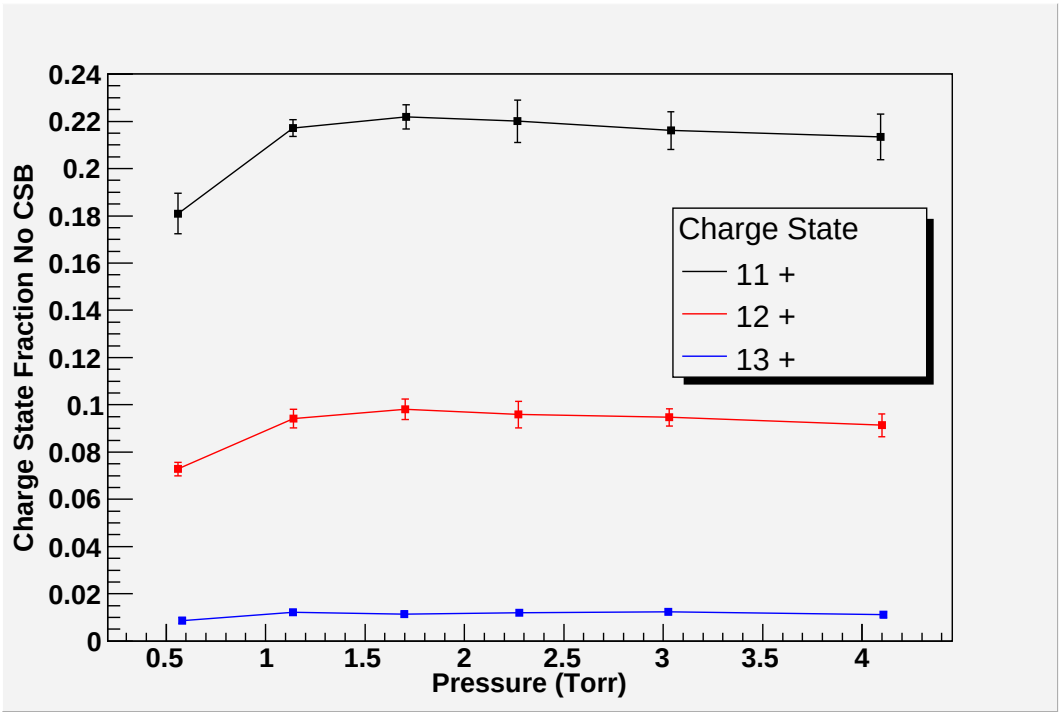

Figure 4.18. The charge state distributions rapidly reach equilibrium, within 1-2 torr of gas pressure within the gas target. The data shown is for ^{48}Ti beam at 826 keV/u without charge state booster.

(m close to q_0) then Sayer predicts that,

$$F_q = F_m \exp\left(-0.5\frac{((q-q_0)/\rho)^2}{1+\epsilon(q-q_0)/\rho}\right) \tag{4.7}$$

The empirical formulae Sayer arrived at for the parameters are as follows:

$$q_0 = Z(1-1.08\exp(-80.1Z^{-0.506}(vc)^{0.996})) \tag{4.8}$$

$$\rho = 0.35Z^{0.55}\left((q_0/Z)(1-q_0/Z)\right)^{0.27} \tag{4.9}$$

$$\epsilon = \rho(0.17+0.0012Z-3.3(vc)) \tag{4.10}$$

The above is for diffuse gas, and the following is for solid targets:

$$q_0 = Z(1-1.03\exp(-47.3Z^{-0.380}(vc)^{0.860})) \tag{4.11}$$

$$\rho = 0.48Z^{0.45}\left((q_0/Z)(1-q_0/Z)\right)^{0.26} \tag{4.12}$$

$$\epsilon = \rho(0.0007Z-0.7(vc)) \tag{4.13}$$

Table 4.1. Average systematic uncertainties.

Source of the uncertainty	Uncertainty
Beam normalisation	10%
γ-array efficiency	16%
Charge state fraction	5%
Stopping power	1.5%
Beam energy uncertainty	5%
Effective target length	4%

where Z is the atomic number of the beam particles, v is their velocity and c is the speed of light in vacuum.
Applying these formulae directly did not give satisfactory results, even with a purely gas target, see Fig 4.16. To get satisfactory results, the mean charge state was empirically scaled by a linear factor $q_0 = (a + bE)q_0^{Sayer}$ where a and b were obtained from a fit to the data. A good fit was then achieved. The charge state fractions which could not be found through linear interpolation between known charge state fractions were then found using equation 4.7. Uncertainties using this formula were estimated to be $\sim$5%.

4.7 Reaction Rate Determination

With all the pieces of equation 4.1, the excitation function for the ^{40}Ca(α,γ)^{44}Ti reaction was constructed. The reaction rate is then calculated from resonance strengths and energies using the formalism discussed in Chapter 2.

4.7.1 Excitation Function

The data from all 184 recoil data runs can be seen in Fig 4.19. Those runs which were taken at the same energy and pressure were averaged. Uncertainties were added in quadrature. The average uncertainties are summarized in Table 4.1. Yields are tabulated in Appendix A.

4.7.2 Stopping Cross Section

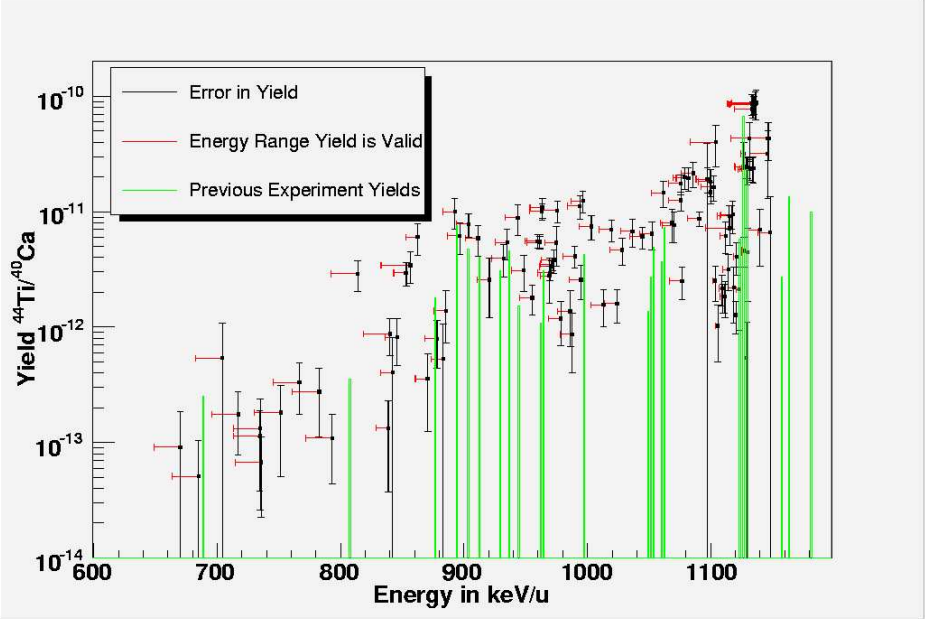

Figure 4.19. The yields for the ^{40}Ca(α,γ)^{44}Ti reaction. The height of the green bars are predicted contributions to the yield from resonances detected through previous γ-ray experiments [2, 3, 4, 5, 6]. See chapter 5 for further discussion.

To relate the yields of the excitation function to the resonance strengths necessary for the thermonuclear reaction rate, the stopping cross section ϵ_{lab} was required. As discussed in section 4.1, this quantity was found by measuring the energy loss of the beam at different gas target pressures. The stopping cross section is related to the energy loss per unit thickness, also called stopping power $\frac{dE}{dx}$, by the inverse of the number density n of the gas (atoms per unit volume),

$$\epsilon = \frac{1}{n}\frac{dE}{dx} \tag{4.14}$$

The number density of the gas is determined from the ideal gas law and is given by,

$$n = 9.66 \times 10^{18}\frac{\mathrm{P}}{\mathrm{T}} \tag{4.15}$$

where P is the pressure in torr and T is the temperature of the gas in Kelvin (300 K in the DRAGON gas cell). Because the DRAGON gas target is not very long and the gas pressures are small, the energy loss per unit thickness varies slowly with energy, and is essentially a constant. The energy loss per unit thickness can thus be well approximated by the total energy loss ΔE

divided by the effective target length, $\Delta x_{target} = 12.3 \pm 0.5$, such that $\frac{dE}{dx} \sim \Delta E / \Delta x_{target}$ and

$$\epsilon = \frac{T}{9.66 \times 10^{18} P} \frac{\Delta E}{\Delta x_{target}} \tag{4.16}$$

By measuring the beam energy at many different pressures using MD1, the stopping power can be easily found. The results of those measurements can be seen in Fig 4.20.

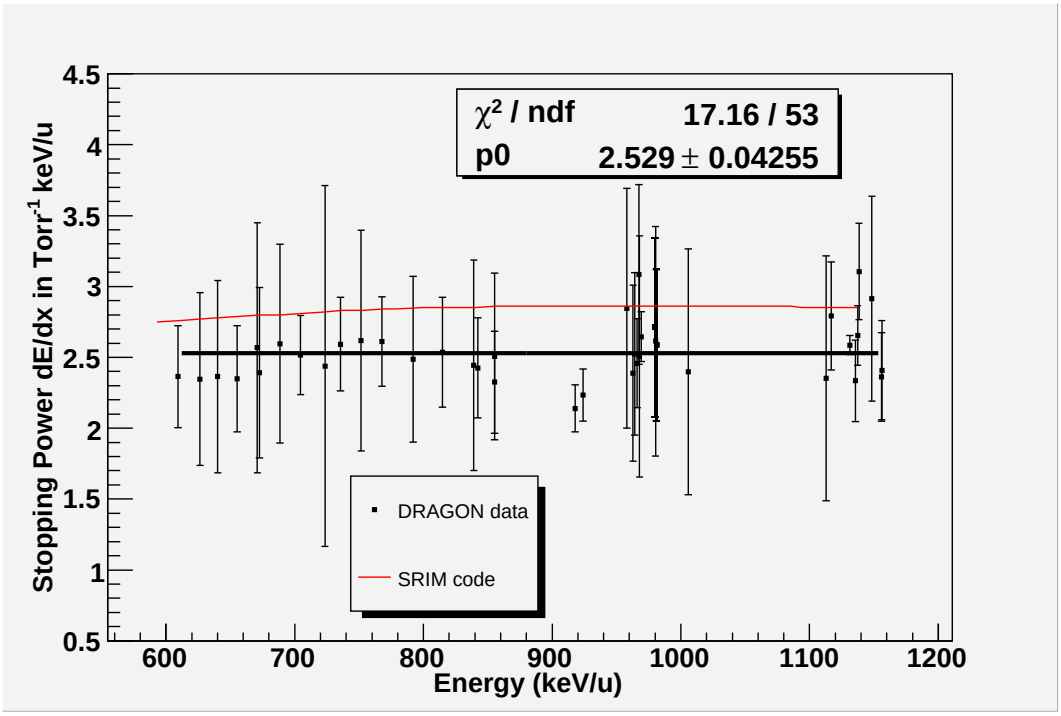

Figure 4.20. Stopping power measurements made with DRAGON and comparison to SRIM Monte Carlo (2003 version). While much of the data falls within error bars of the model, there remains a 11% discrepancy between average values.

A computer program called SRIM is able to model energy loss of He and H in matter using a Monte Carlo technique. The program then scales the data by the effective charge of the beam and produces a stopping cross section. The values returned by SRIM were some 11% higher than the measured values using DRAGON [66, 67]. On average, DRAGON measures $dE/dx = 2.52 \pm 0.04$ cm^{-1}keV/u and SRIM returns 2.84 cm^{-1}keV/u. SRIM also relies on fitting to available data. No other experimental stopping cross sections for a ^{40}Ca beam through ^{4}He exist to the knowledge of this author, so no further comparison was possible and the SRIM results did not reference any available data.

4.7.3 Thermonuclear Reaction Rate

The procedure used to relate the yield measurements that form the excitation function to a reaction rate is here detailed.
Each yield measurement covers a range of energy determined by the pressure in the gas target. Over that energy range multiple resonances could hypothetically contribute to the observed yield. However, the measurements made do not provide sufficient resolution to find those individual resonances. The yield was then approximated as being the result of a single resonance at the center of the energy region scanned for a given measurement. For each yield, a resonance strength, $\omega\gamma$, was then calculated using equation 2.40, and they are tabulated in Appendix A. A selection was then made of resonance strengths that covered the entire astrophysical region of interest with minimal overlap. The reaction rate was then calculated using the formalism of equation 2.32 and can be seen in Fig 4.21. It is conventional (practical) to present the reaction rate in terms of the units of $\mathrm{cm^{-1}mol^{-1}s^{-1}}$, where the rate $<\sigma v>$ has been multiplied by Avogadro's constant N_A. The uncertainty or error range was calculated with the formalism developed in the paper by Thompson and Iliadis [68]. In concise form the error range was developed as follows:
The reaction rate can be viewed in simplified algebra as,

$$\mathrm{N}_A < \sigma v >= f \sum_{i=1}^{N} (\sigma v)_i \tag{4.17}$$

where $f = 1.540 \times 10^5/(\mu T_9)^{3/2}$ is a purely temperature dependent piece and

$$(\sigma v)_i = (\omega\gamma)_i B_i \tag{4.18}$$

where $B_i = \exp(-\mathrm{E}_i/\mathrm{kT})$ is the Boltzmann term of the reaction rate. The Boltzmann term has an uncertainty σ_B associated with it because the resonance energy is uncertain, and in the case of this experiment that is 5% of the energy. The other uncertainty is that of the calculated resonance strength $\sigma_{\omega\gamma}$. The uncertainty in the Boltzmann contribution is calculated by convolution of the Boltzmann term with a Gaussian and it ends up in the form,

$$\sigma_B = e^{E/kT} e^{(\sigma_E/4kT)^2} \sqrt{e^{(\sigma_E/kT)^2} - 1} \tag{4.19}$$

where σ_E is the uncertainty in the energy. Combined, the overall uncertainty to the reaction rate from a single measured resonance is:

$$\sigma_{r,i}^2 = (f\sigma_{\omega\gamma_i} B_i)^2 + (f(\omega\gamma)_i \sigma_{B_i})^2 \tag{4.20}$$

And the total uncertainty in the reaction rate is the sum of all the uncertainties in the individual resonance rates.

$$\sigma_r = \sum_{i=1}^{N} \sigma_{r,i} \tag{4.21}$$

However, difficulties typically arise at low energies when the lower limit of the reaction rate that would be calculated with the above uncertainty becomes negative. Essentially the standard deviation in the rate becomes larger than the rate itself leading to unphysical negative reaction rates. To remedy this situation asymmetric uncertainties $\sigma_{\pm}^{(a)}$ are used,

$$\sigma_{\pm}^{(a)} = \pm \mathrm{N}_A < \sigma v > [\exp(\pm \sigma_r / \mathrm{N}_A < \sigma v >) - 1] \tag{4.22}$$

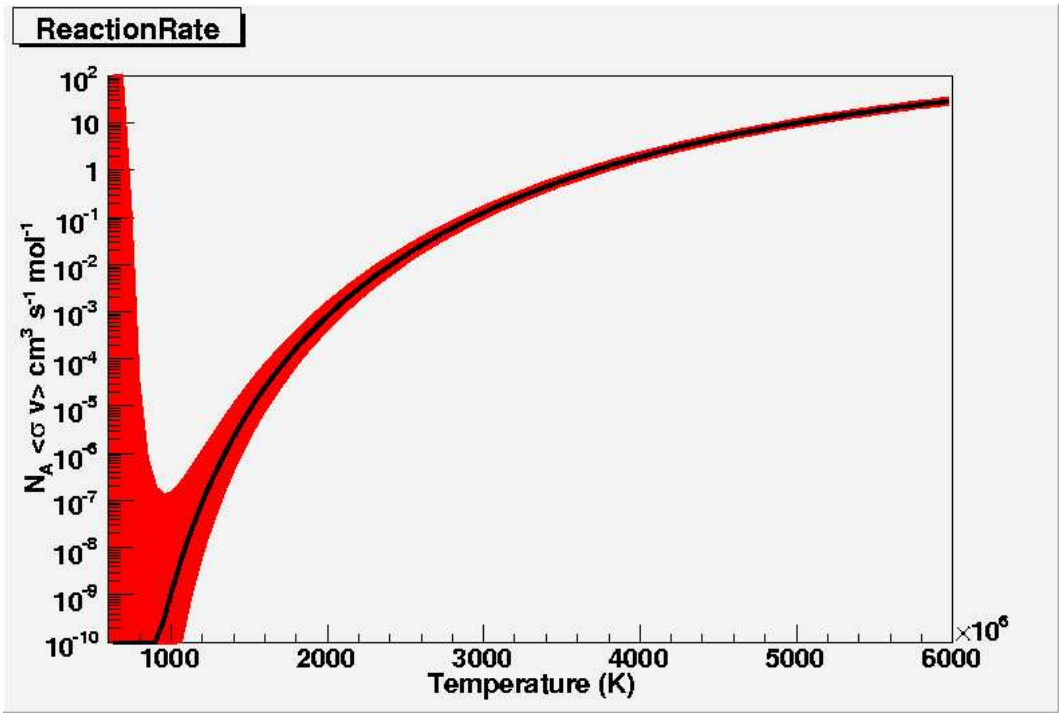

Figure 4.21. The thermonuclear reaction rate for the ^{40}Ca(α,γ)^{44}Ti reaction. The asymmetric uncertainty range, one standard deviation, is shaded in red. The range of temperatures shown goes to lower temperatures where there was no data, and the uncertainty consequently becomes pronounced.

Chapter 5

Discussion and Conclusion

In this section the reaction rate measured in this experiment is compared to other existing reaction rates and the astrophysical implications are detailed.

5.1 Comparison With Other Reaction Rates

As discussed in the introduction, the ^{40}Ca(α,γ)^{44}Ti reaction has been studied before in both experiment and theory. Currently many supernova models rely upon the REACLIB rate libraries [50]. The REACLIB libraries are built out of a combination of statistical theory from a Hausher-Feshbach code called NON-SMOKER and experimental rates. The current REACLIB library rate for ^{40}Ca(α,γ)^{44}Ti uses the γ-ray resonances from the 1970's and 1980's to calculate the reaction rate [2, 3, 4, 5, 6]. These experiments bombarded a ^{40}Ca target with ^{4}He and measured the resulting γ-rays using Germanium-Lithium detectors. In particular the resonance strengths of twelve isolated narrow resonances were measured in the energy range of E_{cm}= 2.5 - 3.6 MeV and then further experiments gave 8 more resonance strengths for resonances from E_{cm}= 3.8 - 4.5 MeV. In total, these cover a corresponding temperature range of 1.2 - 2.9 T_9 ($T_9 = 10^9$ K). A recent experiment using AMS calculated an integrated yield over the region of E_{cm} = 2.1 - 4.2 MeV or correspondingly a range of 0.93 - 2.6 T_9 as well as a smaller window about 4.1 MeV [48]. For comparison the DRAGON data in this work spans E_{cm} = 2.3 - 4.2 MeV or 1.1 - 2.6 T_9.

At present all these measurements agree very well with the region around the triplet of strongly resolved states at E_{cm} = 4.112, 4.100, 4.088 MeV. The γ-ray experiments report resonance strengths of 2$\pm$0.4, 5.8$\pm$0.12

and 0.5±0.1 eV, respectively. The AMS measurement reports an integrated resonance strength of 8.8±3.0 eV for this region. Using DRAGON over the E_{cm} = 4.12 - 4.05 MeV (1135 - 1115 keV/u) region the measured resonance strength is 7.0±1.2 eV, also very much in agreement with the γ-ray experiments. A second series of DRAGON measurements over a slightly lower energy range 1133-1113 keV/u produced a similar result, $\omega\gamma$= 7.2 ±1.5 eV. These numbers are the accumulation of many runs at different beam times and give great confidence to the consistency of the results.

In the analysis section, the resonance strengths measured in the γ-ray experiments were converted into a yield and compared directly to the excitation function developed, Fig 4.19. There is broad agreement between the two data sets: for a given previously known resonance strength, a similar yield was measured with DRAGON. However the data measured with DRAGON clearly show additional yield coming from regions between the published data.

To derive a reaction rate from the AMS measurements, the experimenters first derived an average cross section and then compared that to integrated cross sections from various models. They found that their data agreed best with a scaled BRUSLIB model [48], a model based on a statistical Hartree-Fock approach which incorporates a microscopic model of nuclear level densities. They then integrated the cross section as a function of energy given from the scaled model to produce a rate. The AMS (Nassar) rate can be seen in comparison to the rates from the DRAGON data, the γ-ray experiments in Fig 5.1. Also in Fig 5.1 the BRUSLIB model and the NON-SMOKER model rate can be seen. The Rauscher empirical model is the rate found in reference [69] that is to say it is the NON-SMOKER rate with the γ-ray experimental data folded into it. The closest match to the DRAGON rate is interestingly enough the NON-SMOKER rate. It was argued by the creator of the NON-SMOKER code that the level density in ^{44}Ti was likely not sufficiently high for a reliable prediction from the statistical model [69]. A low level density is also inferred from α-transfer reactions [70]. However, the DRAGON excitation function is conclusive proof of a higher level density than previously known at the time the REACLIB libraries were generated.

5.2 Astrophysical Implications of This Work

The impact of this new reaction rate for the ^{40}Ca(α,γ)^{44}Ti reaction in the production of ^{44}Ti during alpha-rich freezeout has been investigated with the model described in reference [47]. The calculations and results of this section were graciously performed by Lih Sin The from Clemson University. In the supernova model, the adiabatic expansion of pure ^{28}Si is simulated with an initial temperature of T = 5.5 T_9 and peak density of $\rho = 10^7$ g cm^{-3}. The

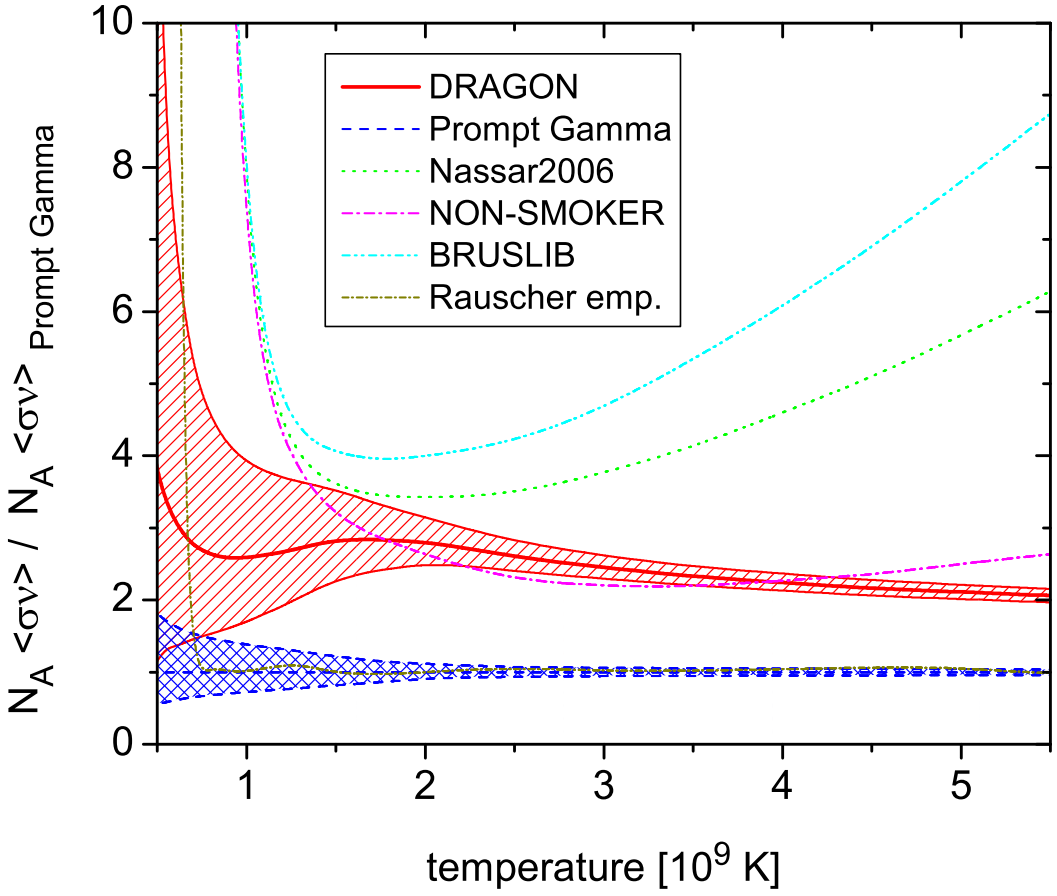

Figure 5.1. A comparative plot of the reaction rate for the ^{40}Ca(α,γ)^{44}Ti reaction from various models and experimental data. The y-axis is normalized to the rate infered from the prompt γ-ray experiments. Both the DRAGON and the AMS measurements point to a higher rate than the previous estimate from γ-ray spectroscopy alone. The hatched areas are the uncertainty range for the appropriate rate. Rauscher emp is the empirical rate found in REACLIB, it follows essentially the prompt γ rate down to the temperature range to where there is no longer γ-ray experiment data. Figure from C. Vockenhuber, verified by C. Ouellet.

resulting ^{44}Ti mass fraction as the gas cools can be seen in Fig 5.2. The general features of Fig 5.2 are here explained. At the high initial temperatures (left hand side of the graph) a large quasi nuclear statistical equilibrium (QSE) cluster is formed from the photodisintegration of ^{28}Si. As discussed in the introduction, this state of QSE is characterized by an imperfect balance of production and destruction of the various nuclei. As the gas cools, the QSE shifts towards production of nuclei of higher mass than ^{44}Ti and the mass fraction correspondingly drops. At $\sim$ 4 T_9 the ^{44}Ti nuclei break out of the QSE, and their numbers increase as they are formed by successive α-capture

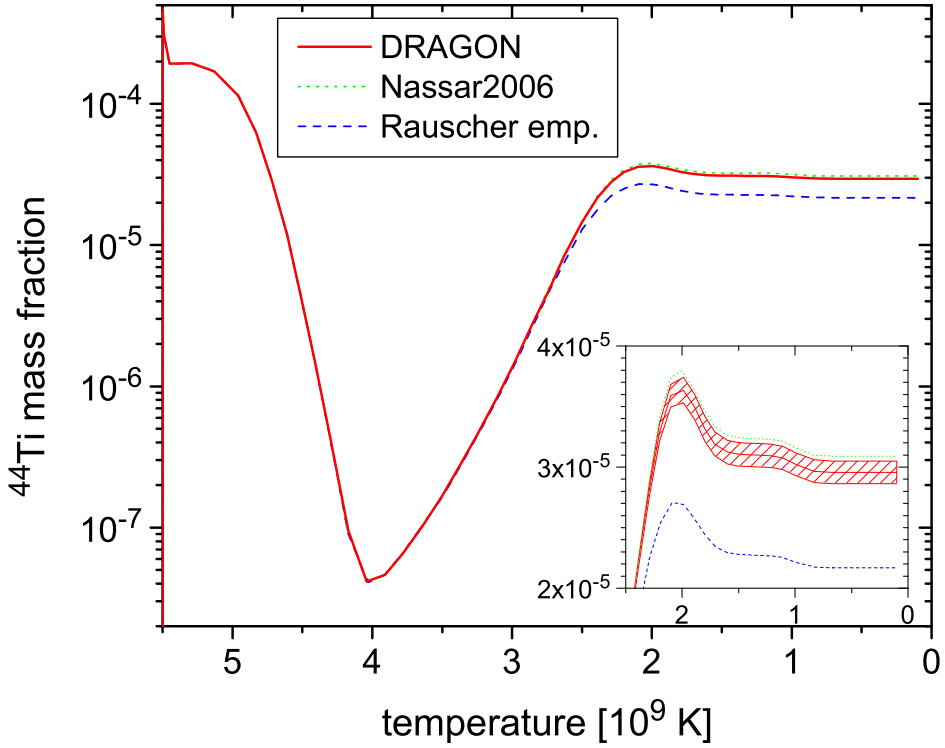

Figure 5.2. The impact of various thermonuclear reaction rates for the ^{40}Ca(α, γ)^{44}Ti reaction on the mass fraction of ^{44}Ti produced by alpha-rich freezeout after a supernova. Both the DRAGON and the Nassar rates point towards higher production than the empirical rates found in REACLIB (labeled Rauscher emp.) below T $\sim$ 2.5 GK. The DRAGON rate shows increased production of ^{44}Ti by about 36% relative to the REACLIB rate. The area of interest is shown in greater detail in the smaller window graph.

reactions with the triple-α reaction as a seed. The final portion of the graph is where the effect of the ^{40}Ca(α,γ)^{44}Ti reaction is most prominent and the differences in the various reaction rates have the largest impact upon the final mass fraction of ^{44}Ti. The final mass fractions of ^{44}Ti, labeled $X(^{44}Ti)$, are summarized in Table 5.1 (Table data courtesy of L.S. The). The ^{44}Ti mass fraction calculated using the DRAGON rate shows an increase of roughly 36% relative to the REACLIB rate. The DRAGON upper limit on the ^{44}Ti mass fraction lies just below the mass fraction derived using the rate by Nassar. However, the Nassar rate specifically used the SRIM stopping power. There is reason to be confident that using the newly acquired DRAGON measurement of the stopping power, the Nasser ^{44}Ti mass fraction will fall within error

Table 5.1. The ^{44}Ti mass fraction resulting from alpha-rich freezeout from a variety of different rates.

rate	$X(^{44}\mathrm{Ti})\times10^{-5}$	$X(^{44}\mathrm{Ti})\times10^{-5}$ Lower limit	$X(^{44}\mathrm{Ti})\times10^{-5}$ Upper limit
DRAGON	2.957	2.864	3.049
γ-ray	2.160	2.094	2.240
Nasser 2006	3.089		
REACLIB	2.169		
NON-SMOKER	2.749		
BRUSLIB	3.216		

Table 5.2. Sensitivity of the ^{44}Ti mass fraction as a function of direct scaling of the ^{40}Ca(α,γ)^{44}Ti reaction rate at different temperatures

Temperature (T_9)	$X(^{44}\mathrm{Ti})\times10^{-5}$ rate$\times$10	$X(^{44}\mathrm{Ti})\times10^{-5}$ rate$\times$0.01
Standard	2.0685	2.0685
$T > 4.3$	2.0685	2.0681
$4.3 > T > 2.8$	2.0683	2.0726
$T < 5.5$	3.7921	0.2819
$T < 2.8$	3.7922	0.1626
$T < 1.0$	2.0685	2.0685

bounds of the DRAGON mass fraction.

The sensitivity to variations in the reaction rate of the ^{44}Ti mass fraction at various temperatures can be seen tabulated in Table 5.2, and were performed prior to the DRAGON experiment to confirm the role of the ^{40}Ca(α,γ)^{44}Ti reaction. To determine the sensitivity, the rate is multiplied by a factor of 10 and in another instance divided by a factor of 100. What remains clear is that the ^{44}Ti mass fraction is unaffected at the high temperatures by the reaction rate as a result of the condition of QSE. The standard rate is from reference [50].

Finally, in a work of this complexity it is very important that more than one person verify the results of the analysis. A postdoc at DRAGON, Christof Vockenhuber, produced an independent analysis of the data, using slightly different cuts and with a different analysis approach. In the final comparison,

our reaction rates agree to within 0.3%.

5.3 Broader Perspective

Modeling supernova explosions is a difficult task, complicated primarily by the uncertain nature of the explosion mechanism. The gas about the Cassiopeia A (Cas A) supernova remnant is emitting thermal X-rays that are consistent with the ejecta of a core collapse supernova. The observed amount of ^{44}Ti produced by the supernova at the origin of Cas A is larger by a factor of 2-10 than predicted by current 1D supernova models (observed $1.6^{+0.6}_{-0.3}\times10^{-4}$ solar mass [42]) [71]. A recent model by Limongi and Chieffi using REACLIB rates gives a wide range of ^{44}Ti production (from 8.44×10^{-10} to 1.3×10^{-4} solar mass) based upon the initial kinetic energy given to the ejecta [72]. This model however fails to reproduce the observed ^{44}Ti/^{56}Ni ratio that has been deduced from the light curves of SN1987a, and it also fails to explain the solar system abundance of ^{44}Ca. The problem may lie in the determination of the mass cut, that is, the fraction of matter that falls back onto the proto neutron star or black hole. It is also possible that asymmetric supernova explosions, thus requiring a 2D or 3D model, could lead to material being ejected from deep layers without subsequently undergoing alpha-rich freezeout and thereby altering the ^{44}Ti/^{56}Ni ratio [73].

Another potential solution to the observed discrepancy could come from the half-life of ^{44}Ti. The laboratory value is now very well established following a 14 year long study and many other measurements [41]. What remains unclear is the ionization level of the ^{44}Ti atom in the ejecta of supernovae. Because ^{44}Ti decays by capturing one of its shell electrons the ionization level of the atom plays a key role in determining its half-life, and fully ionized it is essentially a stable nucleus. Studies by Motizuki and Kumagai indicate that ^{44}Ti^{20+} decays slower by a factor of 0.889 and ^{44}Ti^{21+} by a factor of 0.444 [74]. This would decrease the calculated mass of ^{44}Ti observed in Cas A because of the decay correction, by a factor of 2.4 for dominant ^{44}Ti^{20+}, and increase the amount produced by SN1987A due to the lower activity powering the light curve.

Still another possible avenue of thought is that Cas A is simply an oddity of nature, a particularly strong source of ^{44}Ti. Recent indications of a newly discovered source of ^{44}Ti in the VELA region were not confirmed by COMPTEL or INTEGRAL. It would appear that the only unambiguous source of ^{44}Ti in the sky at present is Cas A. The galactic supernova rate has been estimated at $\sim$3/100 yr. The conclusion that is being drawn is that "either core-collapse supernova have been improbably rare for the past few centuries or ^{44}Ti-producing supernovae are atypical supernovae" [1].

5.4 Conclusion

In conclusion, while this work does not entirely resolve the astrophysical puzzle as to why supernovae appear to be producing the large quantities of ^{44}Ti that are being detecting it does provide a very firm nuclear physics standing for increased production of this radioactive nuclide as a result of previously unresolved resonances. It makes one step towards a greater understanding of one of the many mysteries of the origin of the elements and our own origin.

Appendix A

Table A.1. Tabulated yields and resonance strengths. ΔE is the energy scanned within the gas target.

Energy	ΔE	Yield ($\times 10^{-11}$)	Yield Error	$\omega\gamma$ (eV)	$\omega\gamma$ error
1148.05	9.79484	0.663064	0.690309	0.560906	0.584403
1146.18	14.7435	3.18	1.8716	2.67983	1.58103
1135.21	19.9653	8.42866	1.48235	7.01826	1.26723
1133.57	20.0699	8.62359	1.76173	7.16979	1.49379
1115.34	19.8842	0.719905	0.207913	0.588876	0.171768
1115.05	9.76026	0.915462	0.211373	0.752078	0.176352
1099.65	9.79834	1.82709	0.480155	1.48015	0.393665
1097.23	8.95923	1.91241	0.477152	1.54644	0.390993
1090.86	9.76868	0.870398	0.124986	0.699472	0.104438
1085.81	9.92333	2.15252	0.538228	1.72165	0.436216
1081.77	9.70376	1.95614	0.450611	1.55888	0.36472
1079.18	9.88838	1.97523	0.406455	1.57018	0.32943
1076.78	9.97945	0.250463	0.0782026	0.198648	0.0625548
1075.68	9.67156	1.75123	0.344605	1.38772	0.278916
1070.38	9.97058	0.762585	0.224919	0.601217	0.179023
1068.63	9.61267	0.796205	0.257388	0.626794	0.20424
1061.72	10.0673	1.45515	0.367787	1.13785	0.291335
1052.43	9.8717	0.643632	0.174874	0.49891	0.137083
1044.42	9.86787	0.608295	0.129801	0.467912	0.101666
1036.57	9.96909	0.678092	0.188821	0.517637	0.14569
1028.26	9.87691	0.464883	0.123141	0.352036	0.0943566
1024.07	9.95851	0.159997	0.0517538	0.120658	0.0393404
1019.58	9.83954	0.698635	0.145276	0.524569	0.111175
1013.13	9.99276	0.156235	0.0548657	0.116554	0.0412084

Table A.2. Tabulated yields and resonance strengths. ΔE is the energy scanned within the gas target (cont'd).

Energy	ΔE	Yield ($\times 10^{-11}$)	Yield Error	$\omega\gamma$ (eV)	$\omega\gamma$ error
1003.27	10.0804	0.746912	0.177523	0.551735	0.133067
1002.96	9.80398	0.746912	0.177523	0.551641	0.133044
996.555	10.0933	1.23808	0.257114	0.908396	0.192284
994.936	9.77203	0.257458	0.0830192	0.188623	0.0613118
989.93	10.0601	0.411262	0.0895099	0.299738	0.0663827
986.186	9.99865	0.136985	0.0696809	0.0994618	0.0507576
978.461	9.9912	0.118139	0.0487198	0.0851028	0.0352688
975.556	12.105	1.02222	0.216542	0.733373	0.158234
974.962	9.81152	0.538964	0.205119	0.38689	0.148094
972.934	10.0079	0.3812	0.087363	0.273042	0.0635678
969.681	9.7646	0.295523	0.04102	0.210989	0.0305359
963.785	9.72518	1.08584	0.207125	0.770513	0.150331
959.571	9.89697	0.556555	0.0710336	0.393162	0.0527036
955.28	9.74799	0.179499	0.0529467	0.126242	0.0375952
948.551	9.88883	0.31106	0.107313	0.217203	0.0754608
943.688	10.0357	0.886259	0.266656	0.61561	0.186935
932.181	9.88147	0.393662	0.120995	0.270115	0.083757
920.662	9.99117	0.257711	0.138125	0.174623	0.0938661
911.457	9.96877	0.587077	0.174546	0.393805	0.118193
903.873	9.91577	0.781765	0.183559	0.520028	0.123953
892.674	10.0778	0.997642	0.299309	0.655301	0.198432
885.517	10.1308	0.138745	0.066703	0.0903972	0.0436174
883.17	9.98313	0.0528059	0.0544885	0.034316	0.0354375
878.326	9.89276	0.0794379	0.0350084	0.0513408	0.0227239
870.378	9.86462	0.0356659	0.0231807	0.0228415	0.0148752
862.441	9.8218	0.602007	0.186134	0.382017	0.119153
856.616	23.8047	0.34275	0.102745	0.214249	0.0648248
856.531	23.8116	0.34275	0.102745	0.214227	0.064818
853.42	9.84408	0.294337	0.0691629	0.184811	0.0440851
852.875	9.77357	0.294337	0.0691629	0.1847	0.0440586
845.898	9.73574	0.0819033	0.0355809	0.0509736	0.022243
842.19	10.0105	0.0403325	0.0415114	0.0249866	0.0257375
840.095	21.4776	0.0872007	0.0304015	0.0535172	0.0187873
838.533	9.71175	0.013325	0.00960256	0.00822049	0.00593364

Table A.3. Tabulated yields and resonance strengths. ΔE is the energy scanned within the gas target (cont'd).

Energy	ΔE	Yield ($\times 10^{-11}$)	Yield Error	$\omega\gamma$ (eV)	$\omega\gamma$ error
813.801	21.7053	0.290295	0.0855878	0.172488	0.0513471
793.305	21.4316	0.0109353	0.00653637	0.00633283	0.00379428
782.481	21.3648	0.0275643	0.0163973	0.0157429	0.00938742
766.664	21.4058	0.0333048	0.0156476	0.018631	0.00878703
751.505	21.7731	0.0182056	0.0131407	0.00997772	0.00721358
735.481	21.0113	0.00672512	0.00447541	0.0036079	0.00240558
716.97	21.2117	0.017594	0.00981496	0.00919657	0.00514439
704.15	21.8747	0.0536916	0.0556829	0.0275426	0.0285867
684.852	21.236	0.00509882	0.00527954	0.00254397	0.00263624
670.044	21.2235	0.00910001	0.00945309	0.00444062	0.00461657

Appendix B

‘

Table B.1. Tabulated equilibrium charge state fractions with charge state booster and gas in the target using ^{48}Ti beam.

Charge State	537 keV/u	706 keV/u	826 keV/u	934 keV/u
9+	0.128±0.006			
10+	0.25±0.01	0.085 ±0.002		
11+	0.27±0.01	0.157 ±0.004	0.103 ± 0.002	±
12+	0.21±0.01	0.33 ± 0.01	0.280 ± 0.006	0.204±0.005
13+	0.052 ±0.002	0.212 ± 0.008	0.287 ±0.008	0.309±0.007
14+	0.00010 ±0.00001	0.084 ± 0.005	0.179 ± 0.005	0.268±0.009
15+		0.018 ± 0.005	0.062 ± 0.001	0.134±0.005
16+			0.0112 ±0.0006	0.037±0.001

Table B.2. Tabulated equilibrium charge state fractions with only gas in the target using ^{48}Ti beam.

Charge State	537 keV/u	706 keV/u	826 keV/u	934 keV/u
9+	0.183 ±0.004			
10+	0.063± 0.002	0.238 ±0.004		
11+	0.0152± 0.0008	0.100 ±0.002	0.216 ± 0.005	
12+	0.00010±0.00001	0.024 ± 0.001	0.093 ± 0.003	0.197±0.006
13+		5.3e-4 ± 3e-5	0.0120 ±0.0006	0.036±0.002
14+				5.5e-4±2e-5

Bibliography

[1] L. The, D. Clayton, R. Diehl, D. Hartmann, A. Iyudin, M. Leising, B. Meyer, Y. Motizuki, and V. Shonfelder, "Are Ti44-Producing Supernovae Exceptional?," *Astronomy and Astrophysics*, vol. 450, pp. 1037–1050, 2006.

[2] W. Dixon and R. Storey, "Levels of ^{44}Ti from the ^{40}Ca(α,γ)^{44}Ti reaction ," *Physical Review C*, vol. 15, pp. 1896–1910, 1977.

[3] E. Cooperman, M. Shapiro, and H. Winkler, "Helium Burning of ^{40}Ca," *Nuclear Physics*, vol. A 284, pp. 163–176, 1977.

[4] W. Dixon and R. Storey, "An Isospin Mixed Triplet in ^{44}Ti," *Canadian Journal of Physics*, vol. 58, pp. 1360–1366, 1980.

[5] R. Peshel, H. S. J. Long, and D. Bromley, "The Radiative Capture Reactions ^{40}Ca(α,γ)^{44}Ti and ^{48}Ca(α,γ)^{52}Ti in the Region of the Giant Dipole Resonance," *Nuclear Physics*, vol. A232, pp. 236–286, 1974.

[6] W. Dixon, R. Storey, and A. Bielajew, "Q-Value of the ^{40}Ca(α,γ)^{44}Ti Reaction," *Nuclear Physics*, vol. A378, pp. 273–279, 1982.

[7] Lucretius, *On the Nature of Things: De Rerum Natura*. Baltimore: The John Hopkins Univ. Pr, 1995, 1995.

[8] M. Wright, *Empedocles: The Extant Fragments (classic latin and greek texts)*. London: Bristol Classic Press, 2001.

[9] J. Dalton, "On the Absorption of Gases by Water and Other Liquids ," *Memoirs of the Literary and Philisophical Society of Manchester*, vol. 1, pp. 271–87, 1805.

[10] P. Dahl, *Flash of the Cathode Rays: A History of J.J.Thompson's Electron*. London: Institue of Physics Publishing, 1997.

[11] E. Rutherford, "The Scattering of Alpha and Beta Particles by Matter and The Structure of the Atom ," *Philosophical Magazine*, vol. 21, pp. 669–688, 1911.

[12] H. Moseley, "The High Frequencey Spectra of the Elements ," *Philosophical Magazine*, vol. 26, pp. 1024–1034, 1913.

[13] R. Boyle, *The Sceptical Chymist*. London: J.Cadwell, 1661.

[14] A. Lavoisier, *Traite Elementaire de Chimie*. Bruxelles: Culture et Civilisation, 1965.

[15] D. Mendeleeff, *The Principles of Chemistry*. London: Longmans, Green, and Co., 1891.

[16] R. Dragoset, "Atomic Properties of the Elements," *NIST handout*, vol. SP 966, p. 1, 2001.

[17] Aristotle, *On the Heavens I and II*. Warminster: Aris and Philips, 1995.

[18] C. Rolfs and W. Rodney, *Cauldrons in the Cosmos*. The University of Chicago Press, 1988.

[19] F. Lucchhin and P. Coles, *Cosmology, the Origin and Evolution of Cosmic Structure* . West Sussex: John Wiley and Sons ltd., 2002.

[20] A. Friedman, "On the Curvature of Space," *Z.Phys.*, vol. 10, p. 377, 1922.

[21] G. Lemaître, "A homogeneous Universe of constant mass and growing radius accounting for the radial velocity of extragalactic nebulae," *Annals of the Scientific Society of Brussels*, vol. A47, p. 49, 1927.

[22] G. Gamow, "Evolution of the Universe," *Nature*, vol. 162, p. 680, 1948.

[23] M. Terasawa, *Origin of Matter and Evolution of Galaxies* . Singapore: World Scientific Publishing Company, 2003.

[24] R. Alpher, H. Bethe, and G. Gamow, "The Origin of Chemical Elements," *Physical Review*, vol. 73, p. 803, 1948.

[25] G. Gamow, "The Origin of Elements and the Separation of Galaxies," *Physical Review*, vol. 74, p. 505, 1948.

[26] B. Carroll and D. Ostlie, *An Introduction to Modern Astrophysics*. New York: W.W.Norton and Company, 1994.

[27] A. Einstein, "Does the Inertia of a Body Depend Upon Its Energy Content," *Annalen der Physik*, vol. 18, pp. 639–641, 1905.

[28] H. Bethe and C. Critchfield, "On the Formation of Deuterons by Proton Combination," *Phys. Rev.*, vol. 54, p. 248, 1938.

[29] E. Salpeter, "Nuclear Reactions in Stars. Buildup from Helium," *Physical Review*, vol. 107, pp. 516–525, July 1957.

[30] T. Weaver and S. Woosley, "Evolution and Explosion of Massive Stars ," *Annals of the New York Academy of Sciences*, vol. 336, pp. 335–57, 1980.

[31] W. Arnett and J. Truran, "Carbon-Burning Nucleosynthesis at Constant Temperature," *Astrophysical Journal*, vol. 157, pp. 339–+, July 1969.

[32] W. Arnett, "Advanced evolution of massive stars. V - Neon burning," *Astrophysical Journal*, vol. 193, pp. 169–176, Oct. 1974.

[33] W. Arnett, "Advanced evolution of massive stars. VII - Silicon burning," *Astrophysical Journal*, vol. 35, pp. 145–159, Oct. 1977.

[34] W. Arnett, "Hydrostatic Oxygen Burning in Stars. I. Oxygen Stars," *Astrophysical Journal*, vol. 173, pp. 393–+, Apr. 1972.

[35] S. Woosley, W. Arnett, and D. Clayton, "Hydrostatic Oxygen Burning in Stars. II. Oxygen Burning at Balanced Power," *Astrophysical Journal*, vol. 175, pp. 731–+, Aug. 1972.

[36] T. Weaver and S. Woosley, "Supernova Models," *Annals of the New York Academy of Sciences*, vol. 375, pp. 357–80, 1981.

[37] E. Burbidge, G. Burbidge, W. Fowler, and F. Hoyle, "Synthesis of the Elements in Stars," *Reviews of Modern Physics*, vol. 29, pp. 547–650, 1957.

[38] C. Iliadis, *Nuclear Physics of Stars*. Darmstadt: Wiley-VCH, 2007.

[39] D. Clayton, *Handbook of Isotopes in the Cosmos*. Cambridge: Cambridge University Press, 2003.

[40] D. Osterbrock, "The Astrophysical Journal Centennial," *The Astrophysical Journal*, vol. 438, p. 1, 1995.

[41] I. Ahmad, J. Greene, E. Moore, S. Ghelberg, M. Paul, and W. Kutschera, "Improved measurement of the ^{44}Ti half-life from a 14-year long study ," *Physial Review C*, vol. 74, p. 803, 2006.

[42] A. Iyudin, V. Shonfelder, H. Bloemen, R. Diehl, W. Hermsen, G. Lichti, J. Ryan, C. Winkler, H. Steinle, M. Varendorff, C. de Vries, and D. Morris, "Comptel Observations of ^{44}Ti Gamma-ray Line Emission from CasA," *Astronomy and Astrophysics*, vol. 284, pp. L1–4, 1994.

[43] J. Vink, J. Laming, J. Kaastra, J. Bleeker, H. Bloemen, and U. Oberlack, "Detection of the 67.9 and 78.4 keV Lines Associated with the Radioactive Decay of ^{44}Ti in Cassiopeia A," *The Astrophysical Journal*, vol. 560, pp. L79–82, 2001.

[44] M. Renaud, J. Vink, A. Decourchelle, F. Lebrun, P. Hartog, R. Terrier, C. Couvreur, J. Knodlseder, P. Martin, N. Prantzos, A. Bykow, and H. Bloemen, "The Signature of the ^{44}Ti in Cassiopeia A Revealed by IBIS/ISGRI on INTEGRAL ," *The Astrophysical Journal*, vol. 647, pp. L41–L44, 2006.

[45] P. Lundqvist, C. Kozma, K. Sollerman, and C. Fransson, "IS0/SWS observations of SN 1987A II," *Astronomy and Astrophysics*, vol. 374, pp. 629–637, 2001.

[46] L. Nittler, S. Amari, E. Sinner, S. Woosley, and R. Lewis, "Extinct ^{44}Ti in Presolar Graphite and SiC: Proof of a Supernova Origin," *The Astrophysical Journal*, vol. 462, pp. L31–34, 1996.

[47] L. The, D. Clayton, L. Jin, and B. Meyer, "Nuclear Reactions Governing the Nucleosynthesis of ^{44}Ti ," *Astrophysical Journal*, vol. 504, pp. 500–515, 1998.

[48] H. Nassar, M. Paul, I. Ahmed, Y. Ben-Dov, J. Caggiano, S. Ghelberg, S. Goriely, J. Greene, M. Hass, A. Heger, H. Heinz, D. Henderson, R. Janssens, C. Jiang, Y. Kashiv, B. NaraSingh, A. Ofan, R. Pardo, T. Pennington, K. Rehm, G. Savard, R. Scott, and R. Vonrasek, "^{40}Ca(α,γ)^{44}Ti Reaction in the Energy Regime of Supernova Nucleosynthesis," *Physical Review Letters*, vol. 96, p. 041102, 2006.

[49] Y. Motizuki, "Key Isotope 44Ti and its Production in Supernovae," *American Institute of Physics Conference Series*, vol. 704, pp. 369–374, 2004.

[50] T. Rauscher and F. Thielemann, "Atomic and Nuclear Data Tables," *Atomic and Nuclear Data Tables*, vol. 79, p. 41, 2001.

[51] A. Iyudin, V. Shonfelder, K. Bennett, H. Bloemen, R. Diehl, W. Hermsen, G. Lichti, R. van der Meulen, J. Ryan, and C. Winkler, "Emission from ^{44}Ti Associated With a Previously Unknown Galactic Supernova," *Nature*, vol. 396, pp. 142–144, 1998.

[52] D. Clayton, *Principles of Stellar Evolution and Nucleosynthesis*. Chicago: University of Chicago Press, 1983.

[53] S. Engel, *PhD thesis: Awakening of the DRAGON: Commisioning of the DRAGON Recoil Seperator Facility.* Bochum: Ruhr Universitat, 2003.

[54] H. Gove, *Nuclear Reactions. Chapter VI.* Amsterdam: North Holland Publishing, 1959.

[55] J. D'Auria, L. Buchmann, D. Hutcheon, P. Lipnik, D. Hunter, J. Rogers, R. Helmer, U. Giessen, A. Olin, and P. Bricault, "A Facility for Studying Radiative Capture Reactions Induced with Radioactive Beams at ISAC ," *Nuclear Physics A*, vol. 621, p. 599c, 1997.

[56] R. Laxdal, "International Workshop on the Production of Radioactive Ion Beams," *PRORIB, Pui India*, vol. 200, p. 1, 2001.

[57] J. Staples, "The Physics of Particle Accelerators," *AIP conference proceedings*, vol. 249, p. 1485, 1992.

[58] D. A. Hutcheon, S. Bishop, *et al.*, "The DRAGON facility for nuclear astrophysics at TRIUMF-ISAC: design, construction and operation," *Nuclear Instruments and Methods in Physics Research A*, vol. 498, pp. 190–210, Feb. 2003.

[59] S. Bishop, *PhD thesis: Direct Measurement of the $^{21}Na(p,\gamma)^{22}Mg$ Resonant Reaction Rate in Nova Nucleosynthesis.* SFU: Simon Fraser University, 2003.

[60] D. Gigliotti, *MSc Thesis: Calibration and Simulaton of a Gamma Array for DRAGON at ISAC.* UNBC: University of Northern British Columbia, 2003.

[61] A. Chen, "Results from the Development of Ionization Detection Systems for the DRAGON Facility," *Nuclear Instruments and Methods in Physics Research B*, vol. 204, pp. 614–618, 2003.

[62] G. Knoll, *Radiation Detection and Measurement.* John Wiley & Sons, 1979.

[63] D. Hutcheon, "The DRAGON Facility for Nuclear Astrophysics at TRIUMF-ISAC: Design, Construction and Operation," *Nuclear Instruments and Methods in Physics Research A*, vol. 498, pp. 190–210, 2003.

[64] R. Keitel, D. Bishop, D. Dale, H. Hui, S. Kadantsev, M. Leross, R. Nussbaumer, J. Richards, E. Stuber, and G. Waters, "Design and Commissioning of the ISAC Control Systems at TRIUMF," *International Conference on Accelerator and Large Experimental Physics Controls Systems*, 1999.

[65] R. Sayer, "Semi-Empirical Formulas for Heavy-Ion Stripping Data," *Revue de Physique Appliquee*, vol. 12, pp. 1543–1545, 1977.

[66] SRIM–The Stopping and Range of Ions in Matter– is a collection of software packages which calculate many features of the transport of ions in matter,http://www.srim.org/.

[67] http://www.srim.org/SRIM/SRIM2003.htm/.

[68] W. Thompson and C. Iliadis, "Error Analysis for Resonant Thermonuclear Reaction Rates," *Nuclear Physics A*, vol. 647, p. 459, 1999.

[69] T. Rauscher, F. Thielemann, J. Gorres, and M. Wiescher, "Capture of α particles by isospin symmetric nuclei," *Nuclear Physics A*, vol. 675, pp. 695–721, 2000.

[70] H. Fullbright, C. Bennett, A. Lindgren, R. Markham, S. McGuire, G. Morrison, U. Strohbusch, and J. Toke, "Four-nucleon Transfer via the (^{6}Li,d) reaction," *Nuclear Physics A*, vol. 284, pp. 329–364, 1977.

[71] T. Rauscher, A. Heger, R. Hoffman, and S. Woosley, "Nucleosynthesis in Massive Stars with Improved Nuclear and Stellar Physics," *Astrophysical Journal*, vol. 576, p. 323, 2002.

[72] M. Limongi and A. Chieffi, "Evolution, Explosion and Nucleosynthesis of Core-Collapse Supernovae," *Astrophysical Journal*, vol. 592, pp. 404–433, 2003.

[73] K. Maeda and K. Nomoto, "Bipolar Supernova Explosions: Nucleosynthesis and Implications for Abundances in Extremely Metal-Poor Stars," *Astrophysical Journal*, vol. 598, pp. 1163–1200, 2002.

[74] Y. Motizuki and S. Kumagai, "44 Radioactivity in Young Supernova Remnants: Cas A and SN1987A," *New Astronomy Review*, vol. 48, pp. 69–73, 2004.